Head-Disk Interface Dynamics of Ultra-Low Flying Air Bearing Sliders for Hard-Disk Drive Applications

by

Brian Hayes Thornton

B.S. (University of California, Davis) 1998
M.S. (University of California, Berkeley) 1999

A dissertation submitted in partial satisfaction of the

requirements for the degree of

Doctor of Philosophy
in

Engineering – Mechanical Engineering

in the

GRADUATE DIVISION

of the

UNIVERSITY OF CALIFORNIA, BERKELEY

Committee in charge:

Professor David B. Bogy, Chair
Professor Kyriakos Komvopoulos
Professor Tomas Devine

Spring 2003

This dissertation of Brian Hayes Thornton is approved:

_____

Chair Date

_____

Date

_____

Date

University of California, Berkeley

Spring 2003

Head-Disk Interface Dynamics of Ultra-Low Flying Air Bearing Sliders
for Hard-Disk Drive Applications

by

Brian Hayes Thornton

Abstract

Head-Disk Interface Dynamics of Ultra-Low Flying Air Bearing Sliders

for Hard-Disk Drive Applications

by

Brian Hayes Thornton

Doctor of Philosophy in Engineering - Mechanical Engineering

University of California, Berkeley

Professor David B. Bogy, Chair

The dynamics associated with the head-disk interface (HDI) in hard-disk drives are studied for ultra-high magnetic recording areal densities. Slider dynamics and flying-height modulation (FHM) are studied both experimentally and by simulation. The experimental results are explained by modeling and simulation to understand and control FHM through design guidelines.

For a steady-proximity flying interface (occasional contacts between the slider and disk) the FHM is composed primarily of repeatable motions induced by the disk morphology. This FHM consists of three frequency regimes, which can be characterized as (1) geometric, (2) dynamic, and (3) zero response FHM. The geometric FHM is the major contributor for certain combinations of sliders and disks, and it is studied in detail in order to understand its cause and to minimize the effects of this component.

A comparative study of the dynamic performance of sliders as a function of form-factor (size) revealed counter intuitive results. It was previously believed that as the form-factor

decreased, the FHM and dynamic performance would improve. However, in this work we found that this conventional understanding is not always the case. As the form-factor decreases, the air bearing stiffness usually decreases and the geometric FHM is not necessarily minimized.

As the slider transitions from steady-proximity to unsteady-proximity, a certain nonlinear characteristic of the air bearing slider system becomes more pronounced. This nonlinearity is studied using joint-time frequency analysis in which a highly non-stationary response causes unusual complexities in understanding the system's behavior in the frequency domain. Also, the cause of an observed "snapping" effect from steady-proximity to unsteady-proximity is explained by incorporating near-contact triggered adhesion forces between the slider and disk through modeling. The experimental results showing this "snapping" effect as well as the presence of an observed flying-height hysteresis can be explained by inclusion of these adhesion forces. These results suggest that there is a lower limit of the flying-height below which a slider cannot fly stable. This lower FH limit may preclude the use of traditional air bearing sliders for areal densities greater than 1 Tbit/in^2, and it is likely to require special designs of the slider's air bearing surface to reach 1 Tbit/in^2.

_____

Professor David B. Bogy
Dissertation Chair

To my parents

TABLE OF CONTENTS

LIST OF TABLES

CHAPTER 2

CHAPTER 3

CHAPTER 4

CHAPTER 6

LIST OF FIGURES

CHAPTER 1

CHAPTER 2

CHAPTER 3

CHAPTER 4

CHAPTER 5

CHAPTER 6

ACKNOWLEDGMENTS

I would like to thank my research advisor, Professor David B. Bogy, for his support throughout my academic career at Berkeley. He has given me a wonderful balance between freedom to explore and academic guidance, which has made my research and academia experience in the Computer Mechanics Laboratory invaluable. I am fortunate to have had the honor to study under him and to know him personally.

I would also like to thank Dr C. Singh Bhatia, who has given me professional and personal advice and support throughout my tenure at Berkeley. His enthusiasm and motivation has encouraged me to continue and finish my Ph. D.

I would like to express gratitude to all the people who have influenced me while interning at IBM. I thank the entire mechanical integration and servo writer groups for giving me a wonderful learning experience. I am fortunate to have worked with Dr Richard Kroeker, who spent endless time in answering my questions while I was working with him at IBM and also during my stay at Berkeley.

I will treasure the friendships and experiences I encountered while at Berkeley. Walton Fong and Ryan Grisso, my former labmates, showed me there is more to life than the laboratory. Walton shinned light on a laboratory without windows making it a brighter and more pleasant place to conduct research. Roger Lo was and continues to be a source of entertainment with his stories. Perry Anderson, a friend since my undergraduate days,

has been a great friend. I will miss the morning trips to Royal Coffee and the morning rides up Tunnel Ave. to Grizzly Peak.

Finally, none of this would be possible without the endless support of my family. My parents have supported my decisions and given me advice, which has been an integral part in my accomplishments and has made me who I am today. They have also taught me to enjoy life to its fullest. My sisters, Shelly and Julia have been endless sources of support throughout my life. My fiancée, Colleen, who has put up with my graduate student life for years, has stood by my side in support and has been a source of motivation and inspiration in all aspects of my life. I am indebted to them for their sacrifices and unconditional love not only during my graduate career but also throughout my entire life.

The research presented in this dissertation was supported by the Computer Mechanics Laboratory at the University of California, Berkeley, and partially supported by the Industry Storage Consortium (INSIC) extremely high density recording (EHDR) program.

Berkeley, May 2003

CHAPTER 1

INTRODUCTION

1.1 Magnetic Recording Hard-Disk Drives

Magnetic recording technology has evolved to become the most common means of storing information. In this digital world, the endless appetite for storage capacity has driven magnetic recording technology over many technical hurdles. This demand for greater capacity has caused the magnetic areal recording density versus time to follow a schedule known in the integrated circuit world as Moore's Law, which states that the number of transistors (or magnetic bits for magnetic recording) per unit area will double annually. In fact, magnetic areal densities have increased at a rate of greater than 60 % annually in the late 90's, thereby exceeding Moore's Law. Along with the magnetic areal density, the data transfer rate has also increased dramatically. This rapid increase in densities and data transfer rates has been enabled by several technological advances in magnetics, mechanics, tribology, and several other areas of research.

The fundamental basis of magnetic recording hard-disk drives has changed very little since its introduction in 1957 by IBM. However, since 1957 the drives' physical size has gone from that of a room to something that is handheld, and the cost has gone from $35,000/Mbit to under $0.01/Mbit. Figure 1.1 shows a picture of a modern hard-disk drive with its cover off exposing the components. The information is written onto co-rotating disks by a read/write transducer that is located at the end of a suspension mounted on a rotary actuator. The combination of the spinning disks and the rotary voice coil motor actuator allows the read/write transducers to rapidly scan the entire surface of

the disk as seen in Fig. 1.2. In order for the magnetic areal density to increase, the area of the magnetic bit has to shrink. The areal density is a product of the track density and the linear bit density as shown in Fig. 1.3. Data is written on circular tracks at fixed disk radii in the form of small domains (bits) of like polarized magnetic grains. Increasing the magnetic areal density requires packing the bits closer together in both the circumferential and radial directions, and a fundamental "paramagnetic" limit at which the bits will demagnetized their neighbors is expected to be reached soon for conventional longitudinal recording.

A density of 100 Gbit/in^2 has already been demonstrated, and the quest for 1 Tbit/in^2 is now the goal of academic and industry researchers [4]. Organizations such as the Information Storage Industry Consortium (INSIC) conducts research in media and heads (magnetics), signal processing, servo, and tribology with all groups having a common goal of reaching 1 Tbit/in^2 [5].

1.2 Mechanics of the head-disk interface

In striving for the densities of 1 Tbit/in^2, we are expecting severe challenges in designing the interface between the read/write transducer and the magnetic media disk or the head-disk interface (HDI). According to the Wallace spacing loss equation, the magnetic signal decreases exponentially as the distance increases between the magnetic media and the transducer [6]. Thus, the lowest signal-to-noise ratio (SNR) would be obtained at a spacing of zero. However, to achieve a tribologically reliable interface, the spacing has to be greater than zero. Over the years the way to achieve a reliable interface, both

tribologically and magnetically, has been to control the transducer-disk spacing by use of an air bearing slider resulting in a “flying” transducer. For a given magnetic areal density, a corresponding spacing is found from modeling and experimentation to be a complex function of several physical parameters and as the areal densities increase, the corresponding head to media spacing must decrease [7]. For areal densities of 3, 35.3, and 130 Gbit/in^2, the corresponding physical spacing has been 38, 10, and 5 nm, respectively [8]. It is projected that in order to achieve 1 Tbit/in^2, a magnetic spacing of 6.5 nm will be required [7]. Allocated to this magnetic spacing budget are the thicknesses of the protective overcoats on the disk and transducer surfaces (1 nm each) and 1 nm of lubricant over the disk surface. The protective overcoats are necessary to provide wear resistance and more importantly corrosion protection of the magnetic media and transducer. The lubrication layer also provides wear resistance and durability. These protective overcoats and the lubricant have been crucial in the development of a reliable HDI, however, for the 1 Tbit/in^2 system this leaves only 3.5 nm of physical spacing or flying-height (FH) between the transducer and the lubricant/disk surface.

The motion of the transducer relative to the disk surface is composed of two components; in-plane and out-of-plane or off-track vibrations and flying-height modulation (FHM), respectively. For large off-track motions, the transducer can read/write the wrong data thereby creating errors. Also, for large FHM, the magnetic readback signal fluctuates and can result in a “write or read skip” due to a loss of signal also causing errors. Both of these fluctuations must been controlled: off-track to within ±12 % of the track width and FHM to within ±10%, corresponding to several nanometers and several angstroms,

respectively. Off-track motion has been controlled by single or dual stage actuator(s) while FH and FHM has been controlled passively. With these tolerances becoming tighter in both the off-track and FHM directions and with the excitation levels increasing due to the disk rotation speed increasing to 20,000 RPM, the control of the HDI fluctuations is becoming more difficult and more important.

1.3 Air-bearing sliders

The FH has been controlled passively through self-acting air bearing sliders such as the example shown in Fig. 1.4. The air bearing slider body size has changed over the years from the full size slider ($4.1 \times 3.2 \times 0.85$ mm) to the current "pico" sliders ($1.25 \times 1.00 \times 0.3$ mm) and the experimental "femto" sliders ($0.85 \times 0.70 \times 0.23$ mm). The air bearing surface (ABS) is a patterned surface that comes within proximity of the disk surface. A thin film magnetic transducer is deposited onto the trailing edge of the slider body. The relative motion between the "stationary" slider mounted on the end of the suspension and the rotating disk generates a thin air film bearing (gas lubrication). The slider body is supported by the gimbal and suspension that is swaged onto the actuator arm. The suspension acts as a flexible support in the out-of-plane direction, which allows the slider to follow the disk runout and distortions. The gimbal acts as a flexible support of the slider to the suspension and the dimple acts as a point load on the slider. The suspension supplies a load ("gram-load") through the dimple to the slider, which is counter balanced by the air bearing pressure force. Static equilibrium is obtained when the forces and moments acting on the slider from the suspension and gimbal balance those generated by the thin air film bearing. For the ABS shown in Fig. 1.4, the equilibrium pressure field

generated by the relative air flow is obtained numerically by the generalized Reynolds equation. The "flying" slider body has similar degrees-of-freedom as an airplane: vertical, pitch and roll. The flying attitude and characteristics of the slider are complex functions of many parameters including the gram-load, shape of the ABS, and relative velocity. The shape and design of the ABS has changed drastically over the years from simple mechanically machined positive pressure taper-flat designs to complicated plasma etched sub-ambient pressure designs as shown in Fig. 1.5. As seen in Fig. 1.1, the pivot point of the actuator and the spinning axis of the disks are fixed. Therefore, as the slider is actuated from the inner diameter (ID) to the outer diameter (OD) of the disk, the relative velocity and the relative air flow direction (skew angle) changes. These changes cause the slider's flying characteristics to vary as the slider seeks from ID to OD.

The most important criteria for ABS slider design is the static performance. The static performance criteria consist of constant FH at the transducer from ID to OD considering manufacturing tolerances and other factors such as altitude insensitivity. It is also desirable for the transducer FH to be coincident with the minimum FH, but unfortunately, the transducer FH is generally a couple of nanometers higher than the minimum FH due to the flying attitude of the slider and the ABS design. A static optimization of the ABS will yield near constant FH from ID to OD, but contains no information on the dynamic performance of the HDI.

In the past, a purely static design of the ABS was sufficient when flying at spacings greater than 30 nm, however, when flying in the sub- 10 nm regime, the dynamics must

be taken more into account. Even though the disk morphologies have become extremely smooth for “super-smooth” media (< 0.5 nm RMS), for low flying sliders, the morphology becomes comparable to the FH. This is analogous to an airplane flying over the desert floor at 20 ft opposed to 2 ft features that appear smooth at 20 ft will appear as large bumps and/or obstacles at 2 ft. With smaller allowable perturbations from steady-state, higher level of excitations, and additional forces that are no longer negligible subjected to the slider, the understanding of the HDI dynamics is becoming a crucial aspect in developing a reliable HDI.

1.4 Objective

The objective of this research is to investigate the out-of-plane (FHM) dynamics and the HDI stability associated with ultra-low flying air bearing sliders. Emphasis is placed on understanding and controlling HDI dynamics with design guidelines to achieve stable and reliable ultra-low FH’s. Both experimental and numerical modeling was used to study and verify the findings and results presented in this dissertation.

1.5 Dissertation outline

This dissertation is divided into seven chapters. The first chapter is an introduction to magnetic hard-disk drive technology, the HDI, and the motivation for the research presented. The technical material is categorized into two parts associated with the transition as FH is lowered to achieve higher magnetic areal densities. The first part, consisting of chapters 2 - 4, is concerned with the dynamics associated with a purely “flying” slider interface without contact. The second part, chapters 5 and 6, is concerned

with the transition between a purely “flying” interface to a “partial-contact” or a “stable” to “unstable” interface. These two categories are common of what occurs as the FH is lowered from sub- 10 nm to sub- 5 nm, or in moving from 100 Gbit/in^2 to 1 Tb/in^2 applications, respectively.

Chapter 2 presents the development of an experimental apparatus and procedure to measure sub- nm FHM and verification of the system by simulation. Also, a case study is included to show the effect of disk morphology on FHM. Chapter 3 presents an investigation of the effect of ABS design and flying attitude on the geometric FHM. Chapter 4 contains a comparative study of the dynamic performance as a function of slider form-factor. Chapter 5 is concerned with an investigation of the nonlinear effect of the HDI as the slider transitions from steady-proximity to unsteady-proximity. Chapter 6 presents an investigation of the HDI instability caused by adhesion forces between the slider and disk. Finally, chapter 7 presents the conclusions of this dissertation.

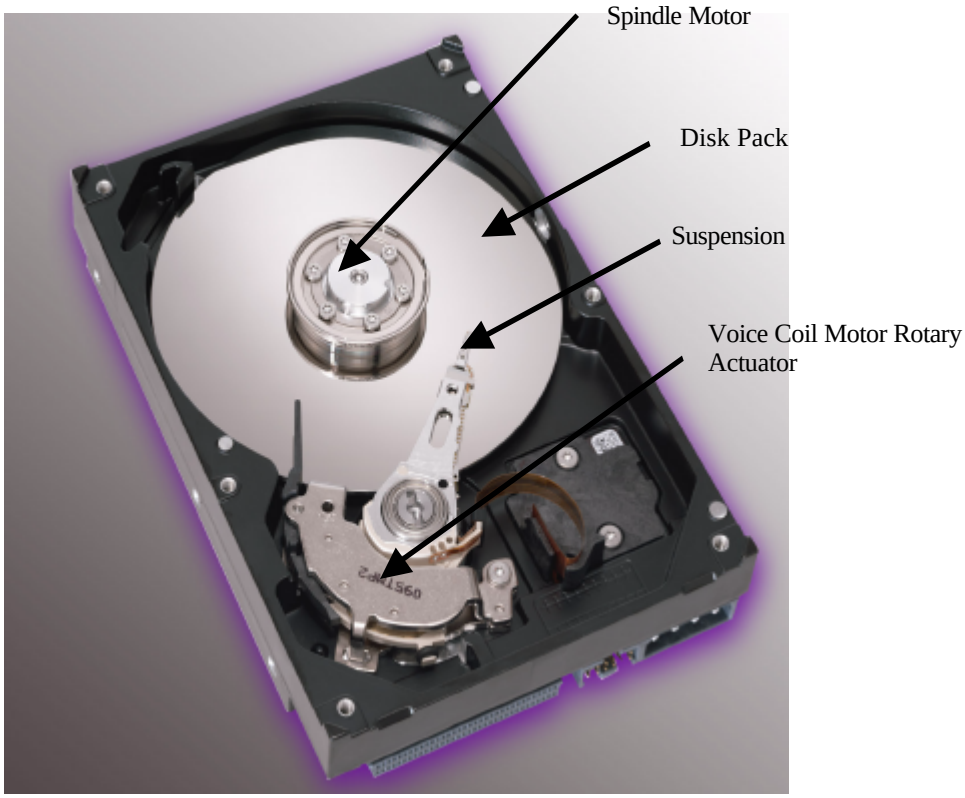

Fig. 1.1. Picture of a hard-disk drive [1].

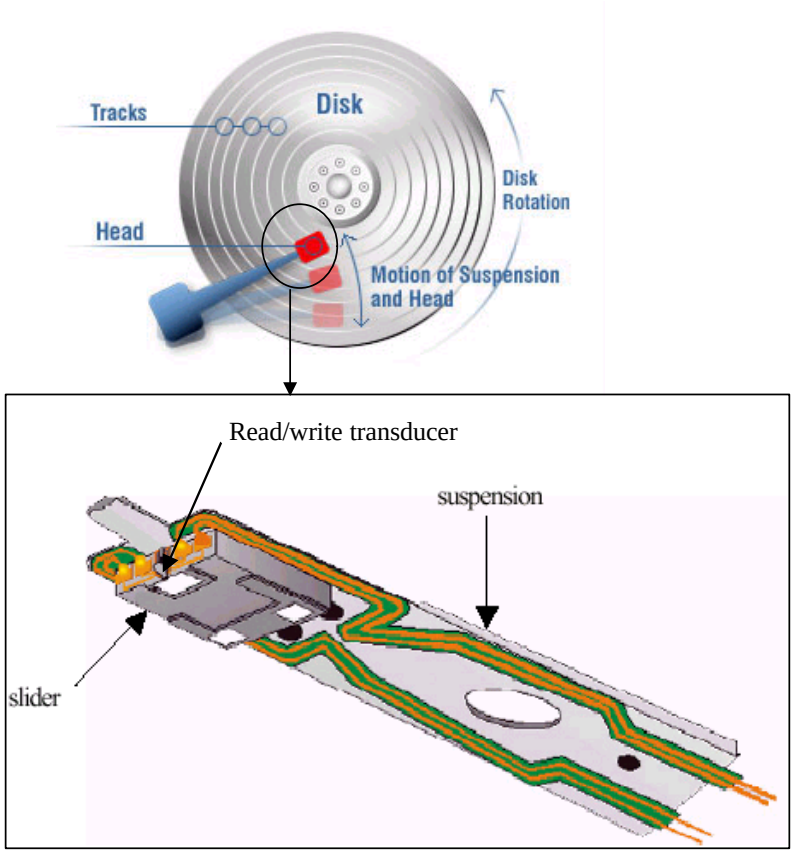

Fig. 1.2. Seeking motion of the actuator and the spinning disks allow the transducer (head) to cover the entire surface of the disks containing the magnetic bits or information [2], [3].

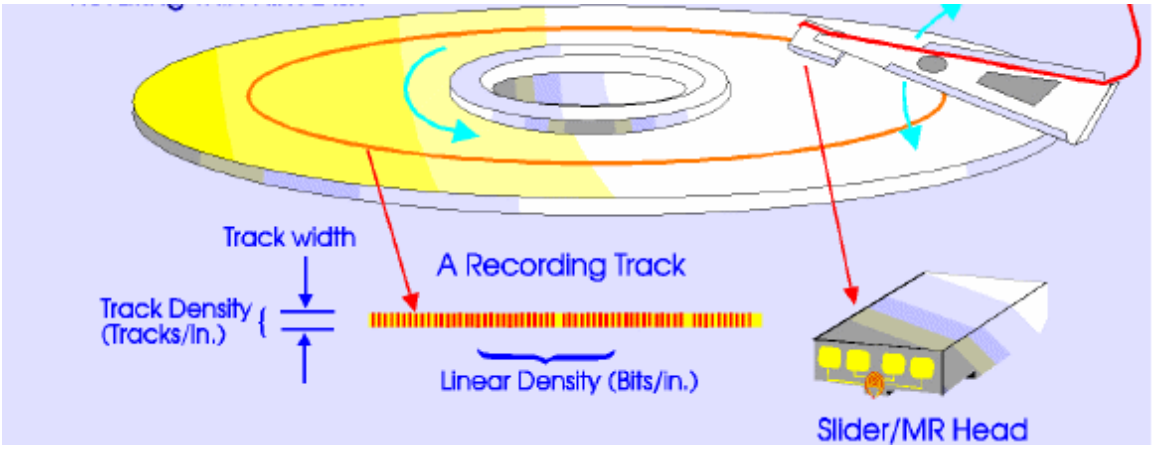

Figure 1.3. Magnetic areal recording density is the product of the linear density and the track density [3].

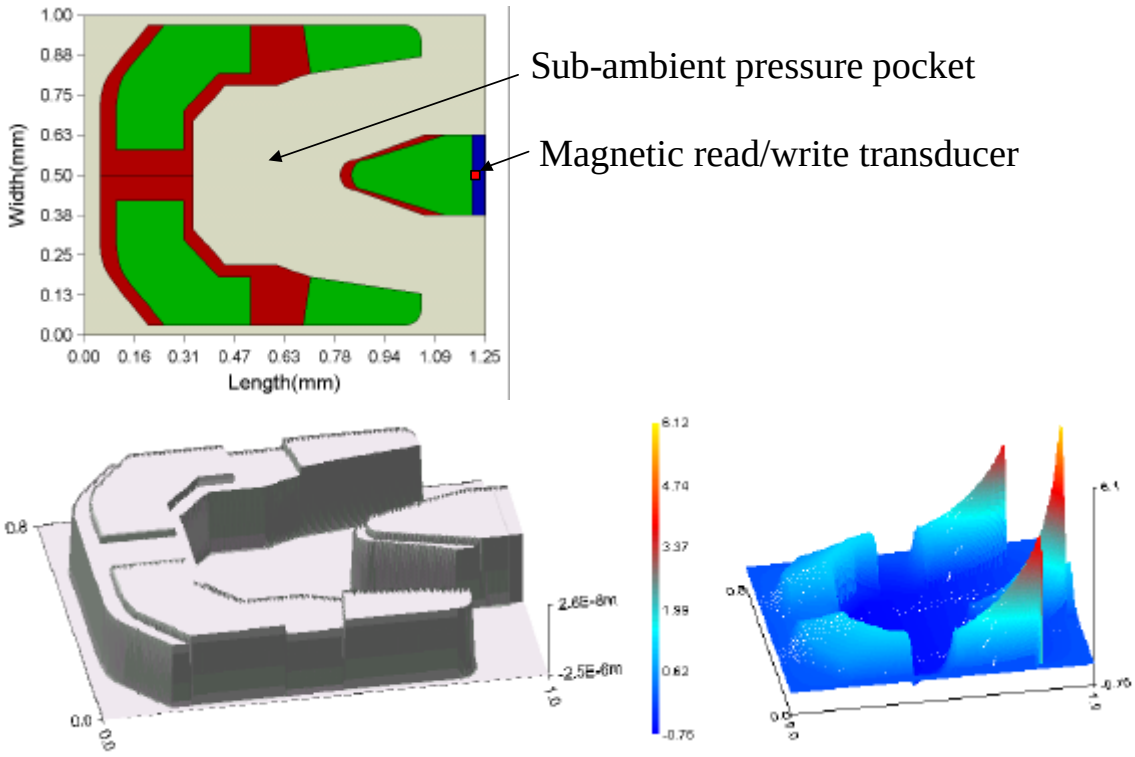

Fig. 1.4. Air bearing surface design and the pressure distribution generated over the surface by the relative motion between the spinning disk and the “stationary” slider.

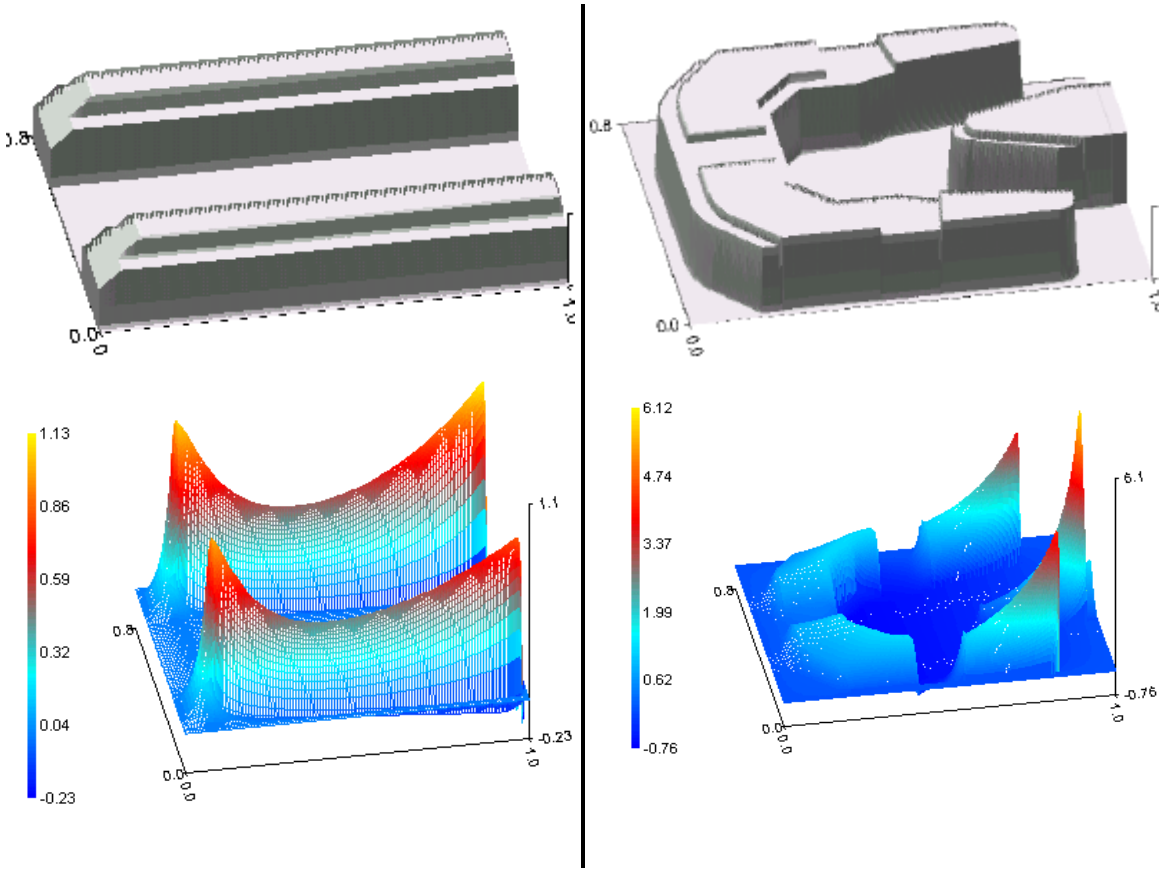

Fig. 1.5. (left) Simple taper-flat positive pressure ABS design and (right) complex sub-ambient pressure ABS design.

CHAPTER 2

THE EFFECTS OF DISK MORPHOLOGY ON FLYING-HEIGHT MODULATION: EXPERIMENT AND SIMULATION

Abstract

The effect of morphology on flying height modulation (FHM) of a sub-10 nm flying air bearing slider was studied for three different disks by experiment and simulation. The experimental measurement methods are discussed and a new single beam laser Doppler vibrometer (LDV) measurement method, which yielded the highest resolution with a 2 μm beam spot size, was introduced. Analysis was performed in three different frequency bandwidths – a geometric FHM from 10 kHz to 100 kHz, a dynamically excited FHM from 100 kHz to 500 kHz and the third band, being negligible compared to the other two bands, above 500 kHz. Transfer function analysis was carried out to investigate the FHM in the lowest frequency band. FHM in the first band was shown to be caused primarily by a phase shift between the sliders' response and the disks' morphology and secondarily by decreasing slider motion with decreasing morphology wavelength, which correlates well with the research presented in Chapter 3. For two of the disks investigated, the FHM due to the disks' morphology showed air bearing excitation that resulted in an intolerable level of FHM. However, for one of the disks studied, the FHM was as low as the disk morphology for wavelengths of 2 mm and less, which was within tolerable limits. It is concluded that when designing a disk for low FHM, it is not sufficient to characterize the quality of a disk by a single number such as roughness or waviness. Proper design and optimization of both the disk and air bearing slider results in FHM that is lower than the disks' morphology.

2.1 Introduction

With flying-heights (FH) decreasing as magnetic areal density increases a better understanding of the dynamics at the head-disk interface (HDI) is required. There are numerous parameters, the effects of some of which are still unknown, that affect the tribological and magnetic performance at the HDI. The condition of "steady-proximity" flying, or flying without contact, over an actual magnetic disk at sub-10 nm FH is not yet completely understood. But understanding the dynamics of the slider due to the disk morphology is required for the design of a stable HDI. The physical spacing requirement for 100 Gbit/in^2 data density is only 6 nm at the transducer location [11]-[12]. Also, reliable reading and writing of magnetic data requires that the transducer location on the slider fluctuate by no more than ±10 % of the nominal FH, which means ±0.6 nm [12]. An accurate method for measuring FHM due to repeatable events such as disk morphology and other motions of the disk was proposed previously by Zeng, Thornton, Bogy, and Bhatia [9].

We applied the LDV to measure FHM in a manner similar to that proposed by Zeng *et al.* with a slight modification [9]. The modification entailed a single or absolute measurement of the disk and slider with a smaller, 2 μm, beam diameter in order to improve spatial resolution. It was found that not only was a higher resolution obtained, but also we were better able to directly compare experimental and simulation results. In this way we investigated three different "super-smooth" disks with an air bearing slider that was designed for 100 Gbit/in^2 applications. By keeping the other experimental conditions constant, we compared the FHM of the three disks experimentally and by

simulation. Excellent agreement between the experimental and simulation results was found. Analysis of the data was broken into three distinct frequency bandwidths: Band I: 10 kHz to 100 kHz, Band II: 100 kHz to 500 kHz, and Band III: greater than 500 kHz. It was shown that the FHM amplitude in Band I, which was found to be the geometric FHM, was on the same order as the disk morphology. The FHM in Band II was found to be dominated by the dynamics of the air bearing slider. It was shown that for a certain level of disk morphology, the air bearing was excited to an intolerable level of FHM. In Band III, it was found that the slider had essentially zero absolute motion as the disk morphology passed underneath. However, the FHM in Band III could be neglected as compared to that in Bands I and II due to the low amplitude of the disk roughness at such high frequencies. From this study, we conclude that many factors need to be taken into consideration when designing a "steady" flying slider and a reliable HDI. With proper design of both the air bearing surface (ABS) and the disk, small fluctuations in the FH can be obtained yielding a more reliable HDI at sub-10 nm spacing, and these fluctuations can be held within ±10 %.

2.2 Experimental setup

The experimental results shown in this chapter were obtained using a modification of the experimental setup explained in detail by Zeng *et al*. [9]. A Thôt Technologies platform with the flyability option was the basic test stand. We used a Polytec LDV with a highpass filter set at 20 kHz for triggering at a small radial scratch on the outer diameter of the disk. This ensures accurate triggering for averaging the measurement. A Polytec 512 LDV with a highpass filter at 5kHz was used for the actual measurement of the disk

and slider motion. Data acquisition was accomplished using a LeCroy oscilloscope sampled at 5 MHz and averaged 500 times. All data post-processing was carried out using Matlab. This general testing platform has shown at least 95 % repeatability for measurements on the nanometer scale [9].

FHM consists of two components – the repeatable and non-repeatable fluctuations. The repeatable fluctuations can be caused by the disk morphology and other repeatable events. The non-repeatable fluctuations can be caused by aerodynamically excited disk flutter and suspension vibrations. However, if an extremely low noise LDV signal is obtained measuring the slider flying in steady-proximity (i.e., no contact), the sliders motion is repeatable as shown in Fig. 2.1 in the bandwidth of 10 kHz – 2 MHz. The high amplitude, low frequency components are almost identical after averaging 500 times with the only difference in the low amplitude, high frequency noise. Therefore, in this bandwidth, the sliders motion due to the disks morphology is almost all repeatable.

2.2.1 Single LDV beam measurement technique

Instead of using a LDV differential beam measurement as in Zeng *et al.* [9], we used a single LDV beam for absolute motion measurement with a beam spot size of approximately 2 μm. However, this can only be accomplished using the velocity output mode of the LDV. The necessary dynamic resolution would be lost if the displacement mode of the LDV were utilized.

As a disk spins, its morphology, clamping distortions, warpage, and other repeatable motions, as viewed by a stationary slider, can be decomposed into an infinite sum of sinusoids having different amplitudes, A_i, frequencies, w_i, and phases, f_i:

$$d(t) = \sum_{i=1}^{\infty} A_i \sin(w_i t + f_i) \tag{2.1}$$

The velocity, v(t) of this displacement is:

$$v(t) = \sum_{i=1}^{\infty} A_i w_i \cos(w_i t + f_i) \tag{2.2}$$

Displacement can be recovered by numerical integration of the velocity. Generally, for "super-smooth" disks, the amplitudes of the components decay exponentially as the frequency increases. If the displacement output mode were used with the LDV, the low frequency content of the disk morphology would overwhelm the higher frequency content, yielding low resolution across the bandwidth. The amplitudes of the velocity components are $A_i\omega_i$ which can be thought of as an exponentially decaying function, $A(w)$, multiplied by linear increasing ω. This helps maintain a higher resolution across the wide bandwidth of interest.

Several comparisons between differential and single beam measurements and different beam spot sizes were completed. Beam spot sizes of approximately 20 μm, 10 μm, and 2 μm were used. However, for the differential dual beam measurement, one of the beams could be no smaller than 20 μm due to the optics arrangement on the tester. For a given sampling frequency, f_s, the spatial resolution of the disk is v/f_s, where v is the relative linear velocity between the slider and the disk. For the test case presented in this chapter with f_s equal to 5 MHz, the spatial resolution was 3.7 μm/sample. If the beam spot size

were greater than the spatial resolution, the disk morphology resolution would be lost. Figure 2.2 shows time domain plots of the FHM and Table 2.1 contains peak-to-peak and 3σ values of the FHM for different measurement methods of the same HDI system. Differential or dual beam and single beam measurements of the FHM for beam sizes of 10 μm and 2 μm are shown (recall that in the dual beam measurement one beam was 20 μm). The 20 μm beam was the limiting factor of resolution for the dual beam method. It can be seen that the peak-to-peak and standard deviation values increase slightly as the beam size decreases. This is due to the ability to capture more high frequency components or very small wavelength features on the disk surface. By using the single beam or absolute measurement not only was higher resolution obtained but also a better understanding could be inferred from the results, as will be seen later in the chapter. This measurement technique provides the absolute motion of the disk surface under the slider as well as the absolute motion of the slider. By subtraction of these measurements the FHM can be obtained.

2.2.2 Effects of disk morphology on FHM

A comparison of three different "super-smooth" disks under the same experimental conditions with the same slider was conducted. Skew angle was set to zero. The linear velocity of 18.7 m/s was chosen to be 1-2 m/s faster than that associated with the first signs of contact, determined by the LDV velocity response of the slider, between the roughest disk and the slider. When the frequency content of the signal contains torsion and/or bending modes of the slider body, at 1.25 MHz and 1.65 MHz, respectively, it is assumed that contact has occurred. Even though the nominal FH of the slider was the

same for all three disks, the clearances over the high spots and asperities of the disks were different. The slider under investigation was a pico negative-pressure symmetric design with a 1.5 gm preload and with the ABS shown in Fig. 2.3.

The transducer FH at the test conditions was approximately 9 nm. The slider chosen for the experiment had good agreement in its attitude parameters (FH, pitch and roll) between measurements on a Phase Metrics Dynamic Flying-Height Tester and simulation using the Computer Mechanics Laboratory (CML) Air Bearing Design Code. The LDV beam was positioned on the slider body adjacent to the transducer to obtain the FHM at the transducer location for comparison between experiment and simulation. The band of the digital filter was 10 kHz to 2 MHz.

2.3 Experimental results

The three disks investigated, disks A, B, and C, are labeled in decreasing order of waviness and roughness. Figure 2.4 shows the frequency content of the disk morphologies from 10 kHz to 2 MHz plotted in nanometers on log-linear axes. When investigating FHM due to disk morphology, we must consider the spectral content of the entire bandwidth. Disks A and B had glass substrates and disk C had an aluminum substrate. As can be seen from Fig. 2.4, the manufacturing processes and substrates can have an effect on surface characteristics. Figure 2.5 shows the frequency content of the FHM obtained from the three different disks. By comparing Fig. 2.3 to Fig. 2.4, we observe that the FHM for disk C appears to be the same as the disk morphology. Also, comparison of the results for disks A and B shows excitations of the air bearing modes at

approximately 160 kHz and 320 kHz, which causes large fluctuations.

2.4 Comparison: experiment and simulation

Simulations were performed using the CML Dynamic Air Bearing Simulator. The measured disk morphologies were used as the input data for the disk surface topographies for the simulator. This one-dimensional measurement was extended radially across the disk surface in the simulation, as a rough approximation of the two-dimensional morphology. For this specific case where the ABS is symmetric, the transducer is at the center of the trailing edge, and the skew is zero degrees, the error from this approximation is expected to be minimized.

Figure 2.6 shows the experimentally measured disk morphology of disk C that was used in the simulation. The comparison between the FHM from experiment and simulation for disk C is shown in Fig. 2.7, where excellent agreement is seen. Similar results were obtained for the other two disks. A summary of the results for all three disks is shown in Table 2.2. The percentages shown in Table 2.2 are the peak-to-peak FHM normalized by the nominal FH, which for this case was 9 nm. Also, shown in Table 2.2 are the 3σ values of the FHM found experimentally, which were close to those values found by simulation. Excellent correlation of experiment and simulation was found in both the time and frequency domain comparisons. From Table 2.2, it can be seen that for disk C the FHM stays within the tolerable range of ±10 %, being ±5.8 % and ±7.35 % for the experiment and simulation, respectively. However, disks A and B exceed this criteria markedly being ±37 % and ±20.2 % for the experimental results, respectively.

2.5 Discussion

The three disks under investigation have very different morphologies, as seen from Fig. 2.4. The effect of the morphology on FHM can now be analyzed using both the experimental and simulation results. We analyzed the data in three distinct frequency bandwidths: Band I: 10 kHz < f < 100 kHz, Band II: 100 kHz < f < 500 kHz, and Band III: f > 500 kHz, where f is frequency. The experimentally determined standard deviations (σ) of the disk morphologies and FHM's are shown in each frequency band for all three disks in Fig. 2.8. Figure 2.9 presents the ratio of the standard deviation of the FHM to the standard deviation of the disk morphology, broken into Bands I, II, and III for disks A, B, and C. The ratios in Fig. 2.9 are outputs (FHM) divided be the inputs (disk morphology) showing the "gain" of the system in the different frequency bands for the three disks.

Band I corresponds to the geometric FHM which is studied extensively in Chapters 3 and 4. Geometric FHM occurs at frequencies below the modal frequencies of the air bearing slider that are determined by the geometry of the ABS, pressure profile underneath the ABS and the disk morphology. This is a complicated function and for this particular ABS, the geometric FHM was on the same order as the disk morphology in Band I as will be shown in Chapter 3. As seen from Figs. 2.8 and 2.9, this holds true for all three disks investigated.

Band II spans the modal frequencies of the air bearing slider. If we consider the air film and slider to be a linear system for small perturbations (which is not true for large

perturbations) under the condition of "steady" flying, the air bearing modal frequencies for the ABS under investigation fall within Band II. So in Band II, the disk morphologies excite this dynamical system and cause a resonance type FHM. Two modes are excited when the slider flies over disks A and B. The differences in the frequency peaks in Fig. 2.5 for disks A and B have to do with the differences in the clearance between the disk and the slider. For disk A the clearance was less than for disk B, causing a greater air bearing modal stiffness. These two modes are the first and second pitch modes of the air bearing. The roll mode does not contribute to FHM at the transducer due to the symmetry of the ABS and the transducer location. From Figs. 2.5, 2.8, 2.9, and Table 2.2 it is apparent that for disks A and B there was an excessive level of excitation of the air bearing, causing FHM. However, for disk C, the disk morphology is so low in amplitude that the air bearing was not excited, and it actually shows a FHM that is lower in amplitude than the disk morphology in Band II. From Fig. 2.9, the gain of the FHM to the disk displacement was more than 2 for disks A and B, but it was only approximately 1 for disk C. From Fig. 2.4, it can be seen that in Band II, the FHM amplitude for disk C decreases with frequency much faster than for the other two disks. The results show how sensitive the FHM is to air bearing excitation. Different air bearing slider designs will have different threshold values for excitation due to the disk morphology.

Band III covers the high frequency range in which the disk morphology passes underneath the slider without causing any significant absolute motion. It is also seen from Figs. 2.4 and 2.8, that the amplitudes of the disk morphologies in Band III were negligible for all three disks, compared to those in Bands I and II.

2.5.1 Explanation of band I

Even in HDI's where the air bearing dynamics are not excited (i.e. the case for disk C, see Fig. 2.8), there may still be a high level of FHM due to the geometric effect mentioned earlier. This effect will be explained in detail in the numerical simulation investigations presented in Chapter 3. As will be shown, the geometric effect is due to a phase shift between the disk surface topography and the response at the transducer location on the slider and also a decrease in the absolute motion of the slider as the wavelength on the disk decreases. This will be shown numerically using a sinusoidal waviness on the disk with various wavelengths but not for an actual disk surface that is composed of an infinite number of sinusoids over all frequencies, as seen in Eq. (2.1). If we use transfer function analysis to decompose the ratio of the output (slider motion) to the input (disk surface motion) into amplitude and phase verses frequency we can compare the experiment and simulation for the response to an actual disk. We used the Welch's averaged periodogram numerical method for estimating the transfer function between the disk and the slider motions with the aid of Matlab. Figures 2.10 and 2.11 show the estimated transfer functions for the experimental and simulation results for both amplitude and phase. Instead of plotting the transfer function verses frequency, f, it was plotted verses wavelength, λ, on the disk: $\lambda = v/f$. From Fig. 2.11, it will be seen that the phase relationship of the ratio of slider motion to that of the disk, for both the experimental and simulation, is similar to what we find in Chapter 3. Similarly, from Fig. 2.10 it can be seen that the amplitude of the absolute motion of the slider decreases as the disk waviness wavelength decreases. Both of these effects combined cause the geometric

FHM, but the phase shift is the primary cause and the decrease in the slider vibration amplitude is a secondary cause [10].

2.5.2 Case study

FHM for 10 different disks designed for sub- 20 nm FH interfaces were measured. These disks varied in manufacture, substrate, carbon overcoat, lubricant, and other variables, hence, there morphologies varied substantially. The peak-to-peak and 3σ disk topography values for the 10 disks are shown in Fig. 2.12 in the bandwidth of 10 kHz – 2 MHz, ranging from "roughest" to "smoothest". If FHM fluctuations are required to be held to within ±10 % of the FH, > ±2 nm of allowable FHM is required. Comparing this criteria to the peak-to-peak values shown in Fig. 2.12 we see that disks 1 – 6 do not meet this requirement. If the design FH were 10 nm, only disk 10 would meet the requirement of FHM less than ±10 % of the FH. Also, it is interesting to notice that the FHM is approximately in one-to-one correlation with the disk topographies; however, this may not always be the case.

2.6 Summary and conclusion

In this study, we modified an existing experimental method to measure the FHM and obtained an increase in resolution, more insight into the mechanics, and as a result we were able to make direct comparisons between experiment and simulation. Different LDV beam sizes were used and compared, showing that the highest resolution was obtained with the single beam measurement using the smallest beam size of 2 μm. Slider vibration measurements taken while flying in "steady-proximity" showed that the

fluctuations were primarily composed of repeatable motion, hence, they were caused by the disk morphology. Experiments were conducted to obtain the FHM over three different disks. Using the measured disk topographies we obtained a direct comparison between experiment and simulation that showed excellent correlation. The FHM was analyzed using the experiments and simulations in the time and frequency domains. Three distinct frequency bandwidths were used to analyze of the effect of disk morphology on FHM. Band I: 10 kHz < f < 100 kHz was the band of the geometric FHM. Additional analysis in this bandwidth using transfer function analysis correlated the results obtained here with the findings of Chapter 3. The geometric FHM amplitude for the particular system studied was on the same order as the disk morphology. However, depending on the slider ABS design and the disk morphology, this geometric FHM may be greater or less than the disk morphology [10]. The FHM in frequency Band II: 100 kHz < f < 500 kHz was influenced by the dynamics of the air bearing. If the disk morphology amplitude in Band II is low enough, excitation of the air bearing does not contribute to the FHM due to the disk morphology. The FHM in frequency Band III: 500 kHz < f < 2 MHz was so low that it could be neglected compared to that in Bands I and II. It is obvious that a single number characterization of roughness or waviness is not sufficient to determine the quality of a disk with respect to FHM. We have shown that, for the particular slider used with disk C, the FHM amplitude is on the order of the disk morphology. However, optimization can be achieved with both the ABS design and the disk morphology to obtain an even lower FHM. A case study was carried out measuring the FHM of 10 different disks manufactured for sub- 20 nm interfaces. The results showed that a majority of the disks did not meet the requirement due to the disks

morphology inducing large FHM. Also, with the correlation realized here between experiment and simulation, simulations can now be used as a design tool. New ABS designs can be modeled and simulated for FHM due to disk morphology prior to manufacturing.

	Dual Beam (10μm beam size)	Dual Beam (2μm beam size)	Single Beam (10μm beam size)	Single Beam (2μm beam size)
Peak-to-Peak FHM [nm]	1.72	1.93	1.93	2.05
3σ [nm]	0.78	0.82	0.82	0.87

Table 2.1. Peak-to-peak and 3σ values of FHM for different measurement methods.

	Disk A	Disk B	Disk C
Experimental FHMp-p/FHnom	74%	40.4%	11.6%
Simulation FHMp-p/FHnom	60%	38%	14.7%
Experimental 3σ [nm]	5.04	2.43	0.81

Table 2.2. The ratio of FHM peak-to-peak to the nominal FH for disks A, B, and C found experimentally and by simulation. Also, 3σ of FHM found experimentally.

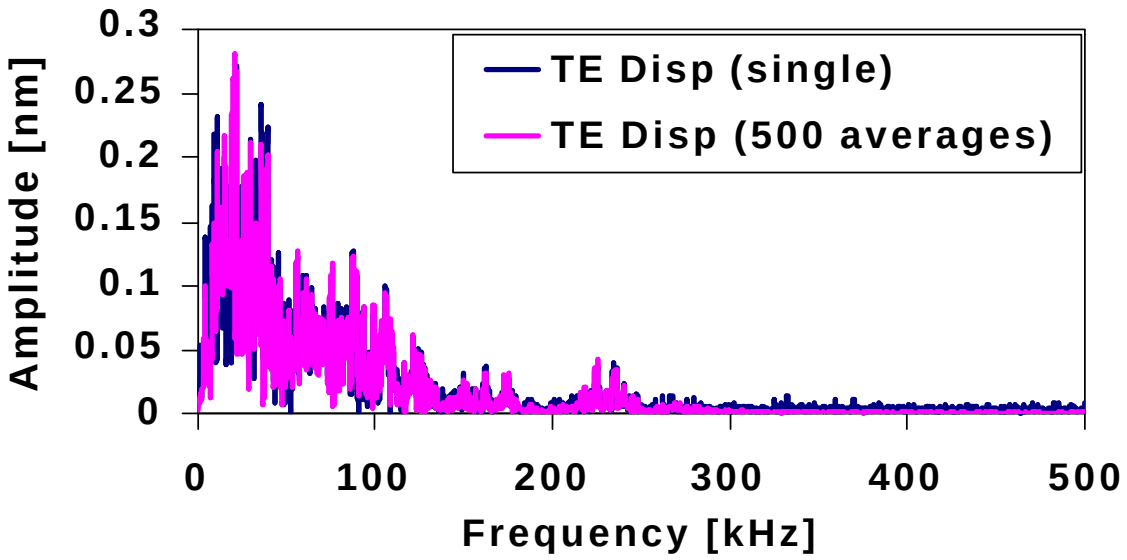

Fig. 2.1. Frequency content of the measured slider vibration in steady-proximity averaged 1 and 500 times.

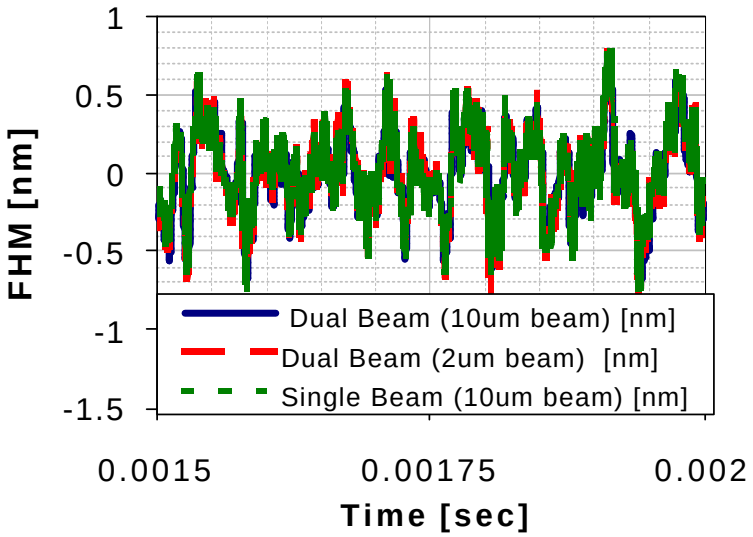

Fig. 2.2. FHM comparison between dual beam and single beam LDV measurements.

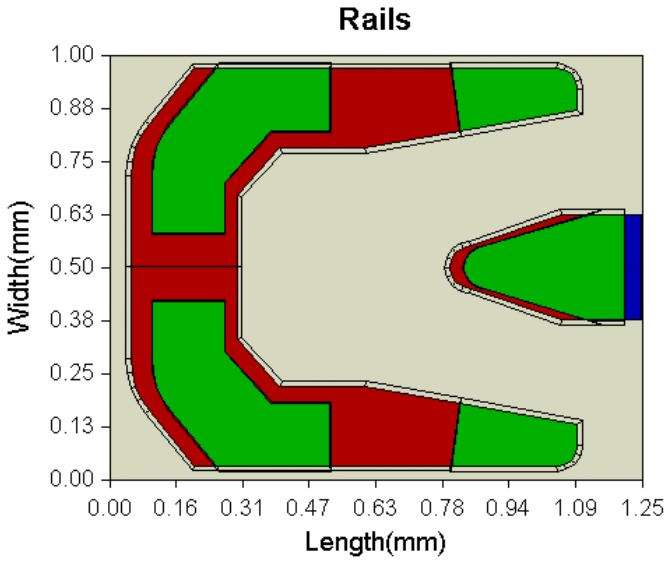

Fig. 2.3: 100 Gbit/in^2 ABS design.

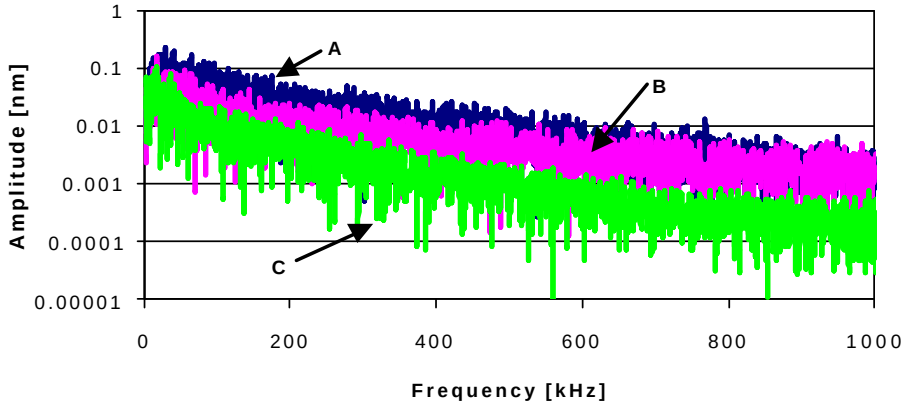

Fig. 2.4. Power spectral density of disks A, B and C morphologies as seen from a stationary point as the disk rotates.

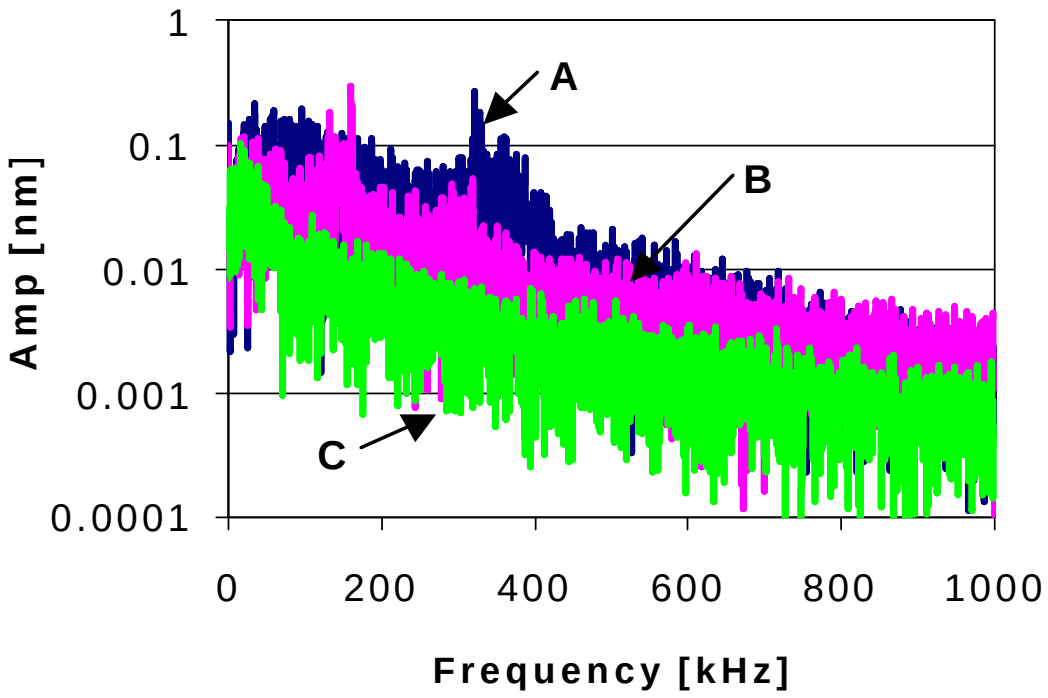

Fig. 2.5. Power spectral density of the FHM at the transducer location for disks A, B, and C.

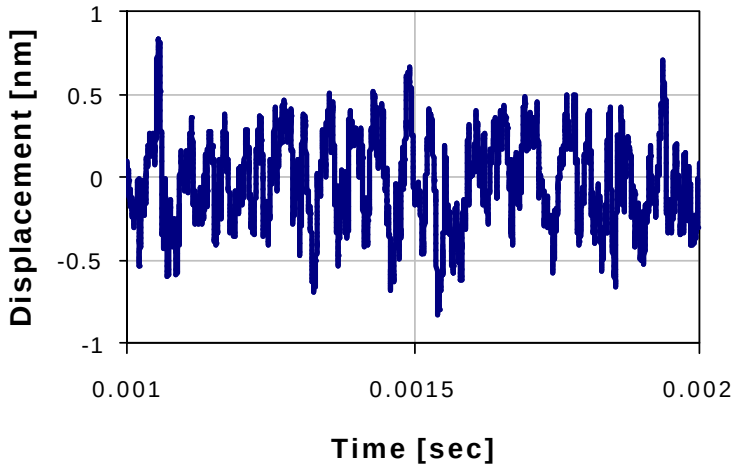

Fig. 2.6. Measured disk morphology of disk C used in the simulation.

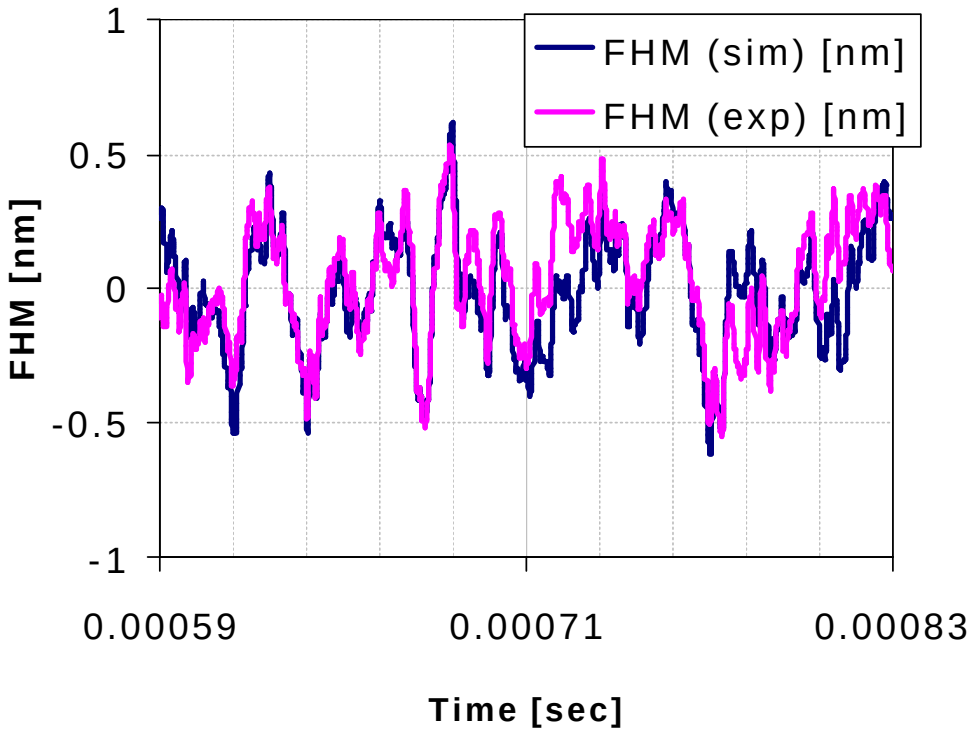

Fig. 2.7. Comparison of experiment and simulation of the FHM for disk C.

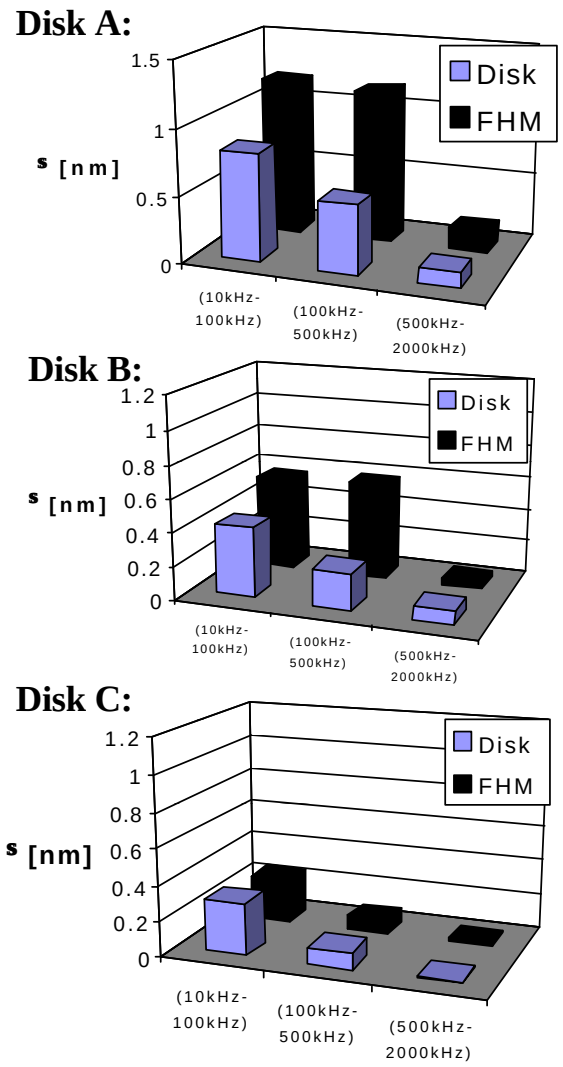

Fig. 2.8. Standard deviation of disk morphologies and FHM for disks A, B and C broken into the three Bands; Band I: 10kHz-100kHz, Band II: 100kHz-500kHz and Band III: >500kHz.

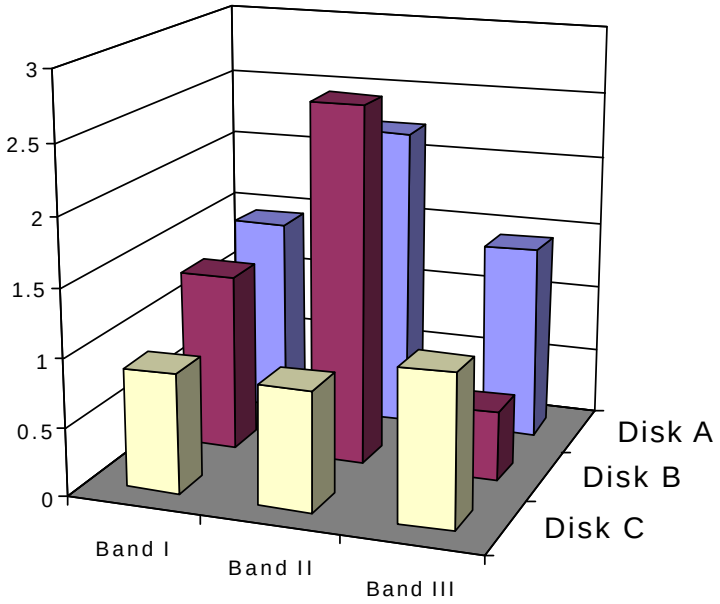

Fig. 2.9. Ratio of the standard deviation of FHM to the disk morphology broken into different Bands for disks A, B, and C.

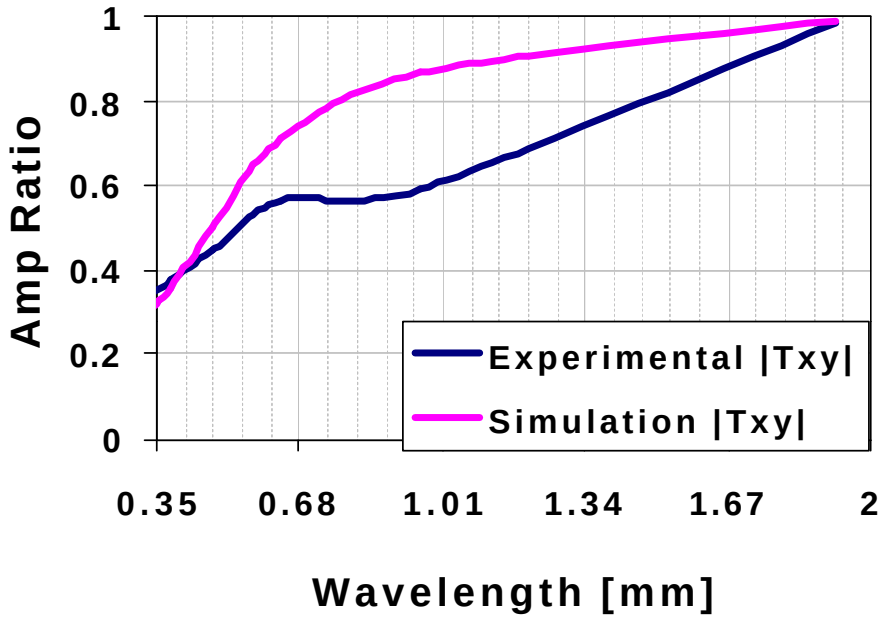

Fig. 2.10. Amplitude ratio of the slider to the disk displacement as a function of wavelength on the disk morphology.

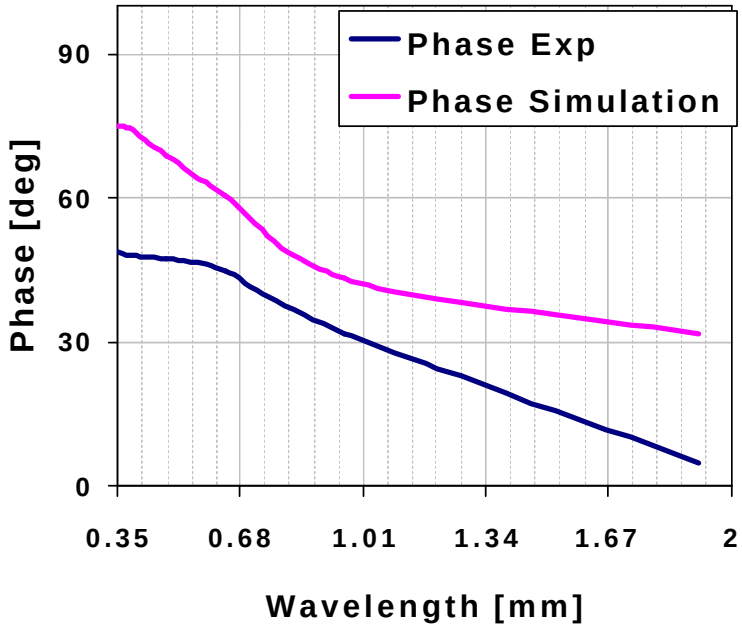

Fig. 2.11. Phase shift between the sliders displacement to that of the disk.

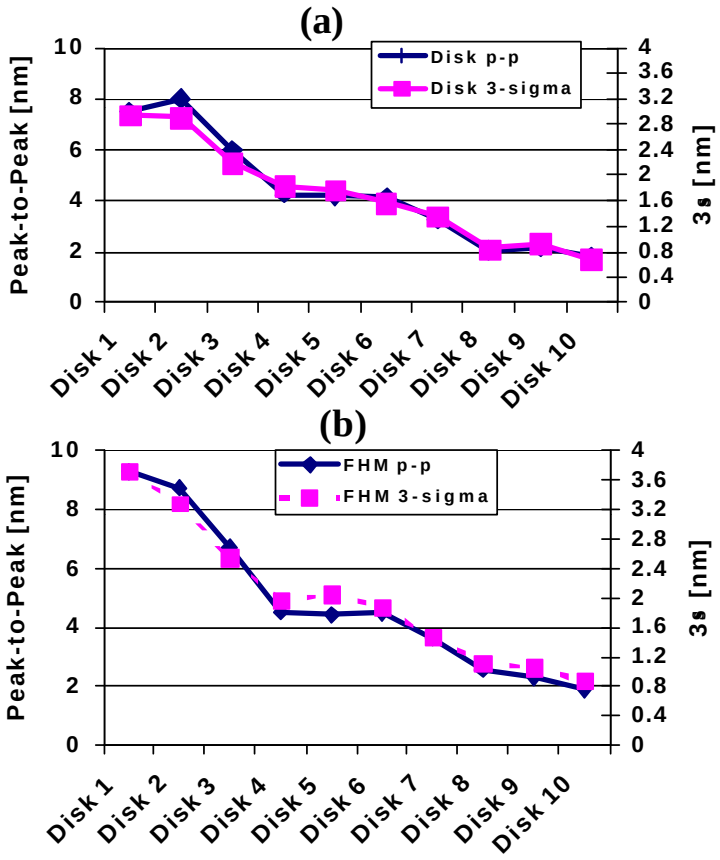

Fig. 2.12. Peak-to-Peak and 3σ measured values of the (a) disk topography and (b) the corresponding FHM for 10 different disks.

CHAPTER 3

FLYING HEIGHT MODULATION DUE TO DISK WAVINESS OF SUB- 5 NM FLYING HEIGHT AIR BEARING SLIDERS

Abstract

Two new air bearing slider designs are presented for storage densities greater than 100 Gb/in^2 in hard disk drive (HDD) applications. Their dynamic frequencies and mode shapes are characterized, and they are used to study the flying height modulation (FHM) over wavy disks due to geometric effects as opposed to dynamic effects. It is found that low pitch designs experience large FHM at wavelengths on the order of the length of the sliders to one-eighth the length of the sliders due to a complex phase shift in the sliders trailing edge response as compared to the disk waviness. FHM due to disk waviness wavelengths from 2 mm to 0.16 mm was found to be a function of the sliders' attitude (pitch angle) and the air bearing surface (ABS) geometry (pressure distribution over the ABS). The results presented suggest that the pitch should be greater than 100 μrad for the ABS designs presented and attention needs to be focused on the ABS design and disk morphology to avoid unacceptable FHM. A new ABS design was introduced to illustrate the results of the geometric FHM showing an 83% decrease in geometric FHM. The FHM due to geometric effects of the slider designs studied in this chapter could possibly be predicted by the disk morphology alone.

3.1 Introduction

As HDD storage densities approach 100 Gb/in^2 the flying height (FH) of the air bearing sliders must be reduced to 6 nm or less. Since all disks have some roughness and

waviness it is impossible to completely eliminate variations of the FH about its mean value. But it is desirable to limit this variation to no more than ±10 % of the mean FH [11]-[13].

Previous research has shown that FHM has different causes depending on the wavelength of the disk roughness relative to the length of the slider. For long wavelengths the FHM is proportional to the square of the length of the slider, a purely geometric effect. As the roughness wavelength approaches zero the slider flies about the mean surface and the FHM equals the disk waviness. For some intermediate wavelengths of waviness an air bearing resonance may be excited and the FHM depends on the dynamics of the mechanical system [14].

To minimize the long wavelength FHM a shorter slider is obviously needed. Other design features determine the air bearing modal parameters, such as FH, static attitude, and ABS design that determine air bearing stiffness and damping.

It is usually believed that femto sliders will be favored over the most commonly used pico sliders of current HDDs. This chapter investigates the relative performance of a particular pico slider designed for 5 nm FH, suitable for 100 Gb/in^2 applications, and a similar femto 3.5 nm FH slider, expected to be required for 1 Tb/in^2 densities [11]-[13]. First we present the ABS designs for the two sliders and indicate their uniformity of FH over the track range from inner diameter (ID) to outer diameter (OD) of the disk. Then we present their characterization, showing their air bearing frequencies and vibration

modes, as well as their damping characteristics. With these results as a basis we investigate the FHM for given waviness wavelengths of the disk. As expected, we find that for long wavelengths the FHM of the femto slider is about half that of the pico slider, and it is negligible for both sliders for a peak-to-peak waviness amplitude of 2 nm. As the disk wavelengths are reduced from 4 mm to 0.156 mm, it is found that the FHM of the femto slider actually exceeds that of the pico slider. This unexpected phenomenon is not associated with resonance but is found to result from the sliders' pitch and an associated phase lag between the dynamic response of the slider at the transducer point and the disk waviness. The primary finding of this work is that the FHM for some slider designs, especially certain five-pad, sub-ambient pressure designs with a center rear pad, will be unacceptably large if the pitch is too low. For low pitch the rear center pad does not generate a pressure leg, and only the aft portions of the side rails support the slider. For high pitch the rear center pad also provides comparable pressure, thereby producing the third leg of support for the slider. It was found that the FHM due to disk waviness with length on the order of the sliders' body length (1.5 mm to 0.156 mm) is a function of the sliders' attitude and the ABS design and not the length of the overall sliders' body. It is found that the geometric FHM can possibly be predicted by the disk morphology alone. To illustrate these findings, a femto ABS design is presented to minimize the FHM due to disk waviness, and it shows an 83% decrease in geometric FHM. Geometric FHM can be extremely significant, showing a maximum of 3.5 nm peak-to-peak for a disk waviness amplitude of only 2 nm peak-to-peak. Only by proper design of an ABS and disk morphology can tolerable levels of FHM be obtained.

3.2 Pico and femto designs

The pico slider was designed for 5 nm FH for use in 100 Gb/in^2 HDD while the femto slider was designed for 3.5 nm FH for use in 1 Tb/in^2 HDD. Both sliders use basically the same design, a wrap around front rail that surrounds three sides of a sub-ambient region and a trailing center pad for mounting the transducer and controlling the flying height of the transducer. Figures 3.1 and 3.2 show the designs of the two sliders. There are three step levels on both sliders, the no-etch level of the primary air bearing surfaces, the 300 nm etch regions adjacent to the rails, and the 2.5 μm base level of the sliders. Tables 3.1 and 3.2 also indicate the FH profile as a function of radial position and the associated skew. The pre-load for the pico slider is 1.5 gm, while it is 1.0 gm for the femto slider. Notice that the pitch of the pico slider is 120 μrad while it is only 55 μrad for the femto at a radius of 15 mm; the skew is zero degrees and the spindle rotational speed is 7200 RPM. These values of pitch, radius, skew and RPM are noted because those ID conditions were used in the following analysis.

These sliders were characterized by use of the CML Parameter Identification Program, and the results are shown in Figs. 3.3 and 3.4 [15]. It is seen that the three air bearing modes are quite decoupled, as indicated by the perpendicularity of the nodal lines. Also we see that the two lowest mode frequencies are similar for the two sliders, around 110 and 180 kHz, while the highest mode frequencies are different by about 100 kHz, the femto slider frequency being about 380 kHz versus 280 kHz for the pico slider.

3.3 Dynamic simulation of the FHM

The CML Dynamic Simulator Program was used to calculate the responses of the two sliders to disks of various waviness. In all cases the peak-to-peak amplitude of the waviness was 2 nm, and the wavelengths were chosen between 12 mm and 0.1 mm. Figure 3.5 shows the FHM for the two sliders for a waviness wavelength of 2.5 mm, which is obtained by subtracting the disk waviness from the sliders' displacement at the transducer. Here we see that the pico slider has a peak-to-peak FHM of about 0.4 nm, while it is about 0.27 nm for the femto slider. Similar calculations were made for several different wavelengths, and the resulting peak-to-peak FHM's are plotted for all of these wavelengths for both sliders in Fig. 3.6. As expected the FHM of the femto slider remains below that for the pico slider for wavelengths greater than about 1.5 mm. But for shorter wavelengths the modulation of the femto slider is much greater than it is for the pico slider, reaching a value of almost 3.5 nm at the wavelength of about 0.3 mm. This is an unexpected result. Notice that since the air bearing resonance frequencies are all above 100 kHz, and this value occurs for wavelengths less than 0.1 mm for 7200 RPM this strong response cannot be associated with a resonance phenomenon. Further studies are required to reveal the cause of this phenomenon.

Figure 3.7 shows the disk waviness and the pico slider's response to a 0.625 mm wavelength waviness for two different slider designs that have the same 5 nm flying height, but with different values of pitch. These slider designs are only slightly different; having the load point moved slightly aft/forward and the suspension load slightly reduced/increased for the higher/lower pitch slider. However, the ABS design was

unchanged. Two things are observed from this figure: first it is seen that the sliders' responses are phase shifted from the disk waviness; second we see that the amount of phase shift is much greater for the low pitch slider than it is for the higher pitch slider. Also it is apparent that the FHM, which is the difference between these two curves, increases with the phase shift. Just envision a case where the phase shift is 180 degrees as opposed to a case where it is 0 degrees. Figure 3.8 shows the FHM, absolute slider displacement and phase shift as a function of pitch over a disk waviness wavelength of 0.625 mm for similar 5 nm FH pico sliders. The sliders' response amplitudes are rather insensitive to the pitch, but the phase shift and hence the FHM monotonically increase as the pitch is decreased. Since the original femto slider had much lower pitch than the pico slider the large difference in the FHM for short wavelengths shown in Fig. 3.6 is evidently due to this phase-lag-pitch relation. Indeed, Fig. 3.9 shows the dependence of the FHM, absolute slider displacement and phase shift over a disk waviness wavelength of 0.625 mm for the femto sliders, and it is seen to be quite similar to that in Fig. 3.8 for the pico slider.

3.4 Explanation of the phase-lag-pitch relationship

It has been shown that the increase in FHM with decreasing waviness wavelength is related to an increase in a phase lag between the sliders' response and the disk waviness, which in turn is related to a decrease in the sliders' pitch. The original femto slider had much lower pitch than the pico slider and that accounts for the larger FHM of the femto slider in Fig. 3.6. It remains to explain why this phase difference becomes pronounced at shorter wavelengths and why this is related to pitch.

Figure 3.10 shows a sequence of pressure profiles for the original low pitch femto slider calculated at different locations of the transducer on the waviness phase. (1) is at the waviness trough, (2) is at the waviness mean height on an increasing slope, (3) is at the waviness peak, and (4) is again at the waviness mean height, but on a decreasing slope. While these profiles have some minor differences, the main observation is their similarity and the fact that the central trailing pad provides very little support to this low pitch slider. The slider is almost entirely supported by the small regions at the rear of the side pressure pads, giving it essentially a two-point support at some distance from the trailing edge where the transducer is located. When the disk rises and falls, because of its waviness, the slider responds near these two support points in phase with the disk, while the transducer is cantilevered a certain distance behind, leading to the phase shift. At some location on the slider, there exists a line which we call the “zero phase line” where forward of the line exists a phase lead and aft of this line exists a phase lag (i.e. the transducer location). For some simple slider designs, the “zero phase line” exists at the center of pressure of the ABS. Unfortunately this is not true for all slider designs including those presented in this chapter. Figure 3.11 shows the sequence of pressure profiles for the high pitch femto slider. Here we see that the center trailing edge has relatively high pressure, and therefore this slider is supported by three pressure points, one at the center trailing edge, where the transducer is located. Therefore the “zero phase line” shifts aft and causes the phase shift to be much less.

Figure 3.12 shows that the distance, *l*, between the trailing edge of the side rails and the trailing edge of the center pad (transducer location) is about 0.15 mm for both the pico and femto sliders. When the waviness wavelength is 0.625 mm, *l* is about 0.25 of the waviness wavelength, so the transducer phase lag is about 90 degrees as shown in Fig. 3.13. This also can be seen in Figs. 3.8 and 3.9 for the pico and femto sliders. As the pitch decreases, the phase angle approaches a maximum of approximately 90 degrees. When the waviness wavelength is 0.325 mm the transducer phase lag is almost 180 degrees. This can be seen for the femto slider in Fig. 3.14. Similarly, as the pitch decreases, the phase approaches 180 degrees. This case of 180 degrees phase shift is the worst-case situation with the FHM becoming maximum due solely to the subtraction of a sine and cosine wave.

Thus, the slider should have sufficient pitch to give it a three-point support rather than a two-point support. On the other hand, if the pitch is increased too much the slider will have only a one-point support at the center trailing edge. Clearly this would not be a stable design.

3.5 Comparison of pico and femto sliders with similar specification

Finally, Fig. 3.15 shows a more meaningful comparison between the pico and femto slider designs. Both sliders were slightly redesigned to have the same flying height of 4 nm and they have similar pitch angles: the pico slider has 116 μrad pitch and the femto slider has 121 μrad pitch. However, there are slight differences in these ABS designs – the femto slider is not merely a scaled down version of the pico slider. Here we see the

more expected behavior. For waviness wavelengths between 6 mm and 1 mm the FHM of the pico slider is roughly twice that for the femto slider. Between the wavelengths of 1.5 mm to 0.156 mm for both the pico and femto sliders', the geometric FHM amplitude increases to about 2 to 2.25 nm peak-to-peak for a disk waviness amplitude of 2 nm peak-to-peak. The femto slider shows slightly worse FHM performance attributed to the differences in the ABS designs and how the pressure profile is distributed. For the femto slider, the "zero phase line" is farther forward on the slider body compared to the pico slider causing worse FHM performance.

Figures 3.16 and 3.17 show FHM, absolute slider displacement, and phase lag as a function of disk waviness wavelengths for the redesigned pico and femto sliders. An important difference between these plots is that the FHM decreases and the phase angle approaches zero at a disk waviness wavelength of 0.156 mm for the femto slider. Figures 3.18 and 3.19 show the results from the CML Parameter Identification Program for the redesigned femto and pico sliders. The redesigned femto slider's air bearing mode stiffnesses are lower than those of the original design while the redesigned pico slider is stiffer than the original. We also see that the redesigned femto slider's pitch resonant mode is approximately 65 kHz. At a disk waviness wavelength of 0.156 mm, this pitch mode is excited, allowing the slider to pivot and permitting the transducer to follow the disk without a phase shift. It should be noted that the emphasis in this chapter is on geometric effects of disk waviness on FHM. This resonance phenomenon is a dynamic effect.

Another contributor to FHM due to a geometric effect is the decreasing amplitude of the absolute displacement of the slider for waviness wavelengths below 2 mm as seen in Figs. 3.16 and 3.17. This is caused by the relationship between the distance from the trailing edge of the side rails to the trailing edge of the center pad (i.e. the distance between the high pressure points, l) and the disk waviness wavelength. If we assume a simple geometric model as shown in Fig. 3.20, for small disk waviness wavelengths, the curvature is too large for the three-support points (high pressure points) of the slider to follow the disk exactly. The analytical solution for the absolute slider displacement is:

$$S_{abs}=A(1+\cos(l\pi/\lambda)) \quad \text{for } \lambda \geq l \tag{3.1}$$

Where l is the distance shown in Fig. 3.12, λ is the waviness wavelength, and A is the sinusoidal amplitude of the waviness. Figure 3.21 shows how the absolute displacement of the slider (S_{abs}) changes with A = 1 nm as wavelength is varied. This relationship follows the trend seen for both the pico and femto sliders from simulations, as seen in Figs. 3.16 and 3.17. However, this geometric effect of the sliders' displacement on the FHM is a secondary effect compared to the phase shift.

For both the pico and femto sliders the FHM for a waviness wavelength of 0.208 mm and varying amplitude from 0.2 nm to 3 nm (peak-to-peak) were simulated to find the dependence of FHM on amplitude of the disk waviness. Figure 3.22 shows how FHM changes with disk waviness amplitude. For both the pico and femto sliders, the relationship is linear with an approximate slope of one (i.e. for this particular waviness wavelength the FHM amplitude is that of the disk). Therefore, FHM due to this geometric effect is also a function of the disk morphology amplitude. For the particular ABS

designs studied in this chapter, the geometric FHM can be predicted by the disk morphology. For waviness wavelengths from 0.5 mm to 0.16 mm the FHM is approximately the disk morphology and for higher wavelengths, the FHM decreases exponentially.

3.6 ABS design for minimizing FHM due to geometric effects

From the work presented here we conclude that certain design parameters need to be taken into consideration when designing an air bearing slider for low FHM. Firstly, the "zero phase line" should be as close to the transducer as possible. Unfortunately, this is a very difficult design condition due to the transducers location and the dynamic stability of the slider. The best that can be done is to concentrate a high pressure point at the transducer location with very low pressures everywhere else on the ABS. This will move the "zero phase line" closer to the transducer thereby decreasing the parameter l. Secondly, the distance between the high pressure points, l, needs to be decreased as much as possible. This ensures the secondary cause of FHM will be minimized as seen from Eq. (3.1).

Modifications were made to the femto slider design to obtain a very high pressure point near the transducer with a pitch of 450 μrad. However, after analyzing the slider from a dynamics point of view, the air bearing resonant frequencies were found to be far to low and the stability was drastically compromised.

A new femto ABS was designed with the above parameters considered. The ABS design and pressure profile are shown in Fig. 3.23. The air bearing was not very stiff in the roll and the pitch degrees of freedom (43 kHz and 62 kHz, respectively), however it was stiff enough to show large improvements with respect to FHM. The pitch was 190 μrads with a 5 nm FH at the transducer. Figure 3.24 shows how the slider's absolute displacement, phase, and FHM change as a function of disk waviness wavelength, similar to Figs. 3.16 and 3.17. At a waviness wavelength of 0.2 mm, the pitch mode is excited; hence the geometric effect is overcome by the dynamics of the slider. As the waviness wavelength decreases from 10 mm to 0.25 mm, a slight phase shift and decrease in slider amplitude occurs because the pressure profile is not a perfect high pressure point – the pressure profile has some distribution across the entire ABS. However, the small phase shift is at most 8 degrees and with the slight decrease in slider amplitude, the phase and amplitude changes are much smaller than those of the original femto design as seen in Fig 3.6. In comparing this redesigned femto slider's FHM to that of the original femto slider shown in Fig. 3.6, we find there is an 83% decrease in FHM. The redesigned femto slider has very low pitch and roll stiffness, which could possibly compromise flyability, however this ABS design is an extreme example to show how important ABS design is for reducing the geometric FHM.

3.7 Summary and conclusions

We examined the FHM of a 5 nm pico slider design and a 3.5 nm femto slider design for disks with 2 nm peak-to-peak waviness amplitude, and as a function of waviness wavelength. The expectation was that the femto slider should have less FHM than the

pico slider, because it has long been known that for wavelengths somewhat larger than the slider length, the FHM is proportional to the square of the length of the slider. It was found that this was indeed the case for wavelengths longer than the slider, but when the wavelength was reduced to about the sliders' length the FHM of the femto slider was much greater than that of the pico slider. After examining the characteristics of the sliders it was found that the primary reason for the large FHM of the femto slider was its low pitch, which caused its pressure support points to be at the trailing edges of the side rails, about 0.15 mm forward of the transducer. It was also observed that the large FHM results from a phase shift between the sliders' response and the disk waviness, which is itself a result of the low pitch and forward pressure points. The phenomenon occurred for both the femto slider and the pico slider.

It can be concluded that, for the five-rail negative pressure sliders under consideration, the pitch should be higher than about 100 μrads to avoid large FHM. The pitch should probably be lower than about 250 μrads to avoid too much load being carried by the single trailing center pad, which would be inherently unstable.

In comparing redesigned pico and femto sliders with the same target FH and comparable pitch, we showed that the pico slider has roughly twice the FHM in the 6 mm to 1.5 mm waviness range. However, for waviness between 1.5 mm to 0.156 mm both the pico and femto sliders have similar high levels of FHM due to their similarities in ABS designs (i.e. pressure distribution). We concluded that a femto design has lower FHM due to disk waviness for wavelengths greater than 1.5 mm. However, for waviness wavelengths

below 1.5 mm and above the dynamic resonant modes of the air bearing, FHM is not primarily a function of the sliders overall length but is more a function of sliders' attitude and the ABS design. It is possible to predict FHM due to this geometric effect by considering only the disk morphology. An extreme femto slider was designed to minimizing the geometric FHM based on the findings in this chapter taken into account. Results showed an 83% decrease in FHM when compared to the original femto slider design. Therefore, these results can be used in designing better ABS's and disks for ultra-low FH sliders. In order to decrease FHM due to disk waviness for wavelengths below 1.5 mm, attention needs to be focused on slider attitude, ABS design, and disk morphology.

Radial Position (mm)	Skew (deg.)	Flying Height (nm)
31	17.39	5.05
23	9.1	4.93
15	-1.22	5.05

Table 3.1. Flying height profile of the pico slider as a function of radial position and skew.

Radial Position (mm)	Skew (deg.)	Flying Height (nm)
31	17.39	3.49
23	9.1	3.54
15	-1.22	3.51

Table 3.2. Flying height profile of the femto slider as a function of radial position and skew.

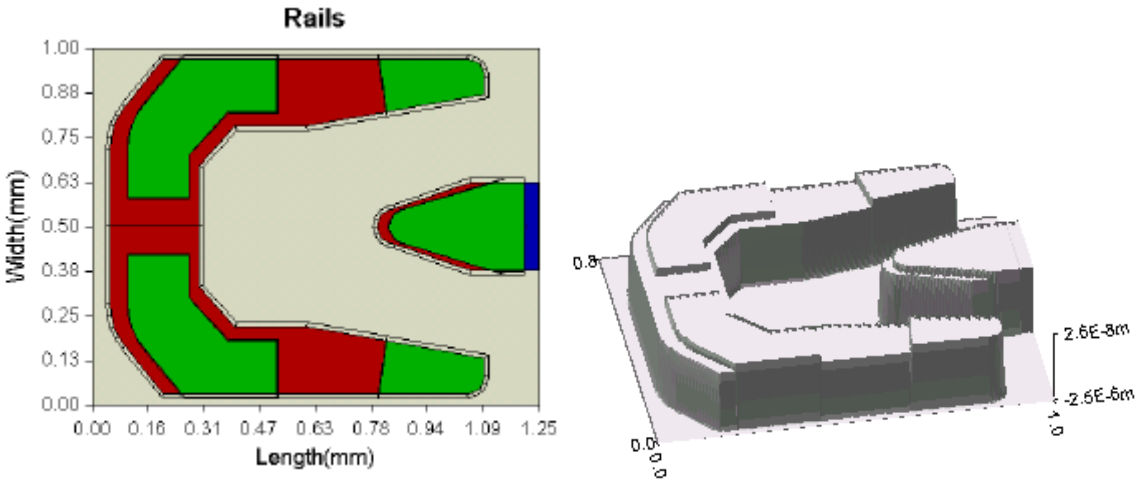

Fig. 3.1. ABS of the 5 nm pico slider.

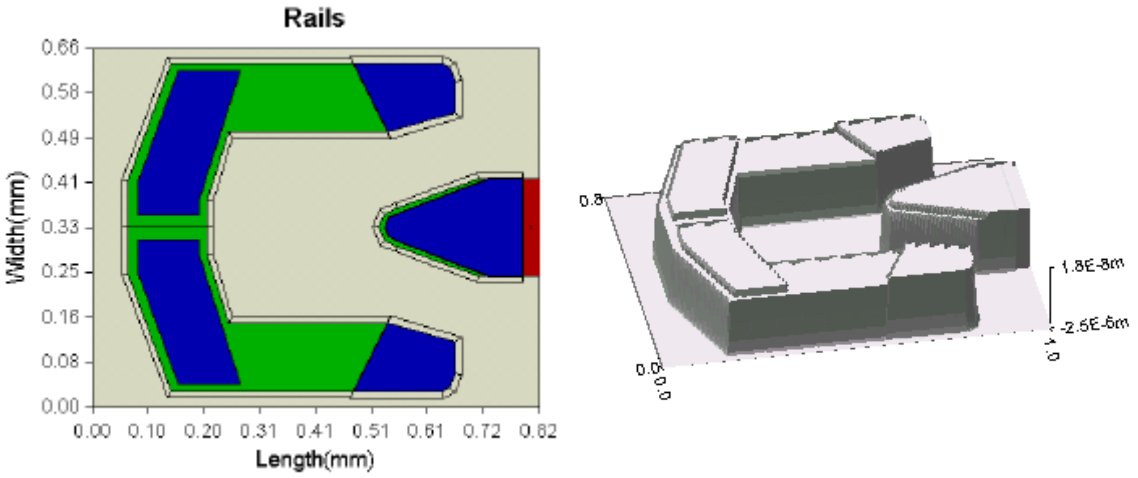

Fig. 3.2. ABS of the 3.5 nm femto slider.

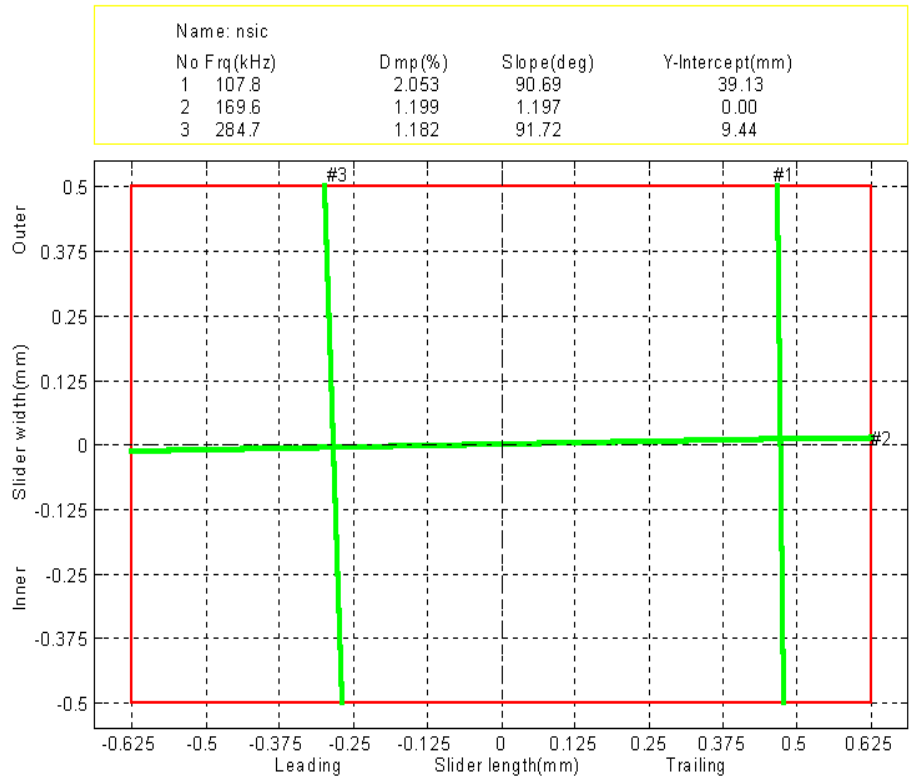

Fig. 3.3. Dynamic characteristics of the pico slider.

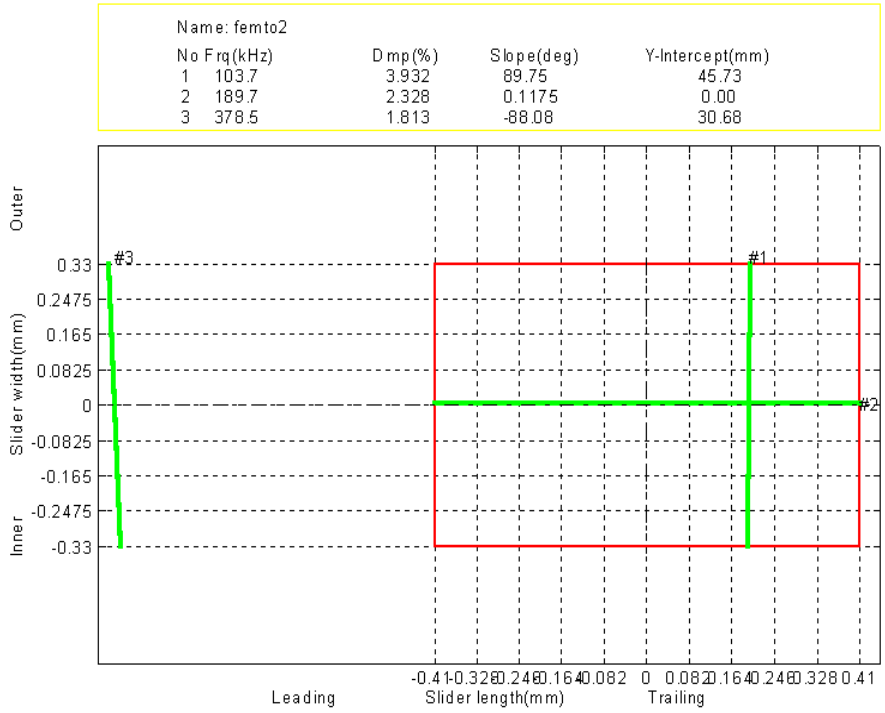

Fig. 3.4. Dynamic characteristics of the femto slider.

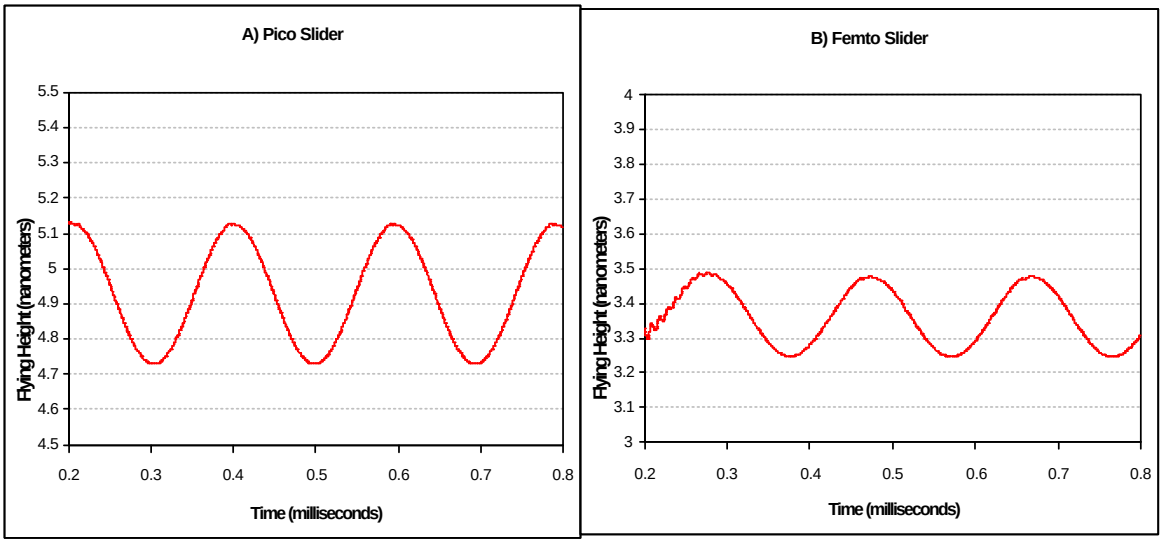

Fig. 3.5. FHM for the (A) Pico and (B) Femto sliders for the 2.5 mm disk waviness wavelength.

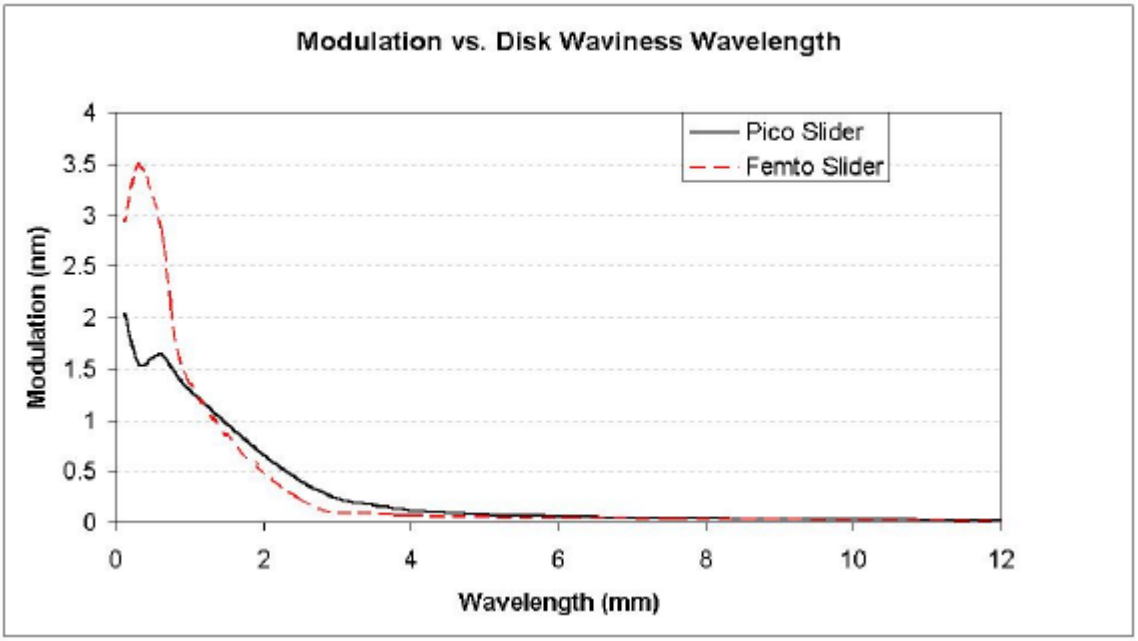

Fig. 3.6. FHM (peak-to-peak) as a function of waviness wavelength for the pico and femto sliders.

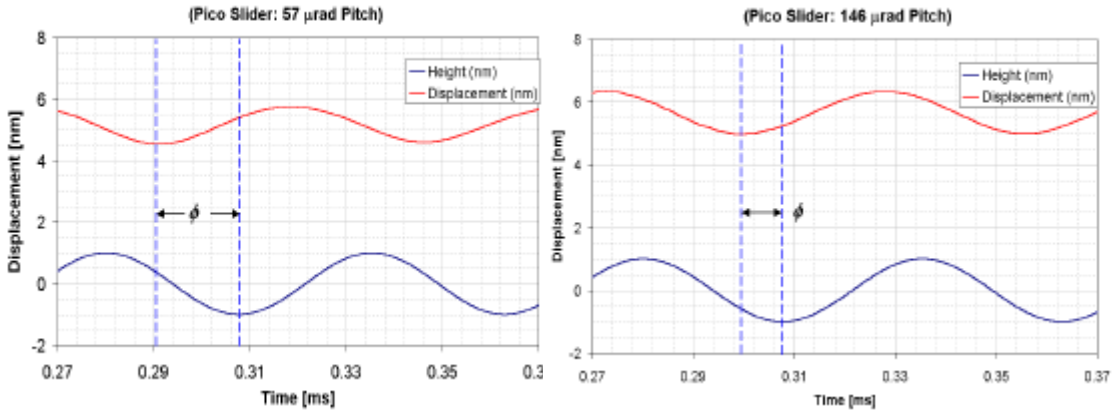

Fig. 3.7. Comparison of the slider motion and the disk waviness, showing a phase difference in the two for different values of pitch.

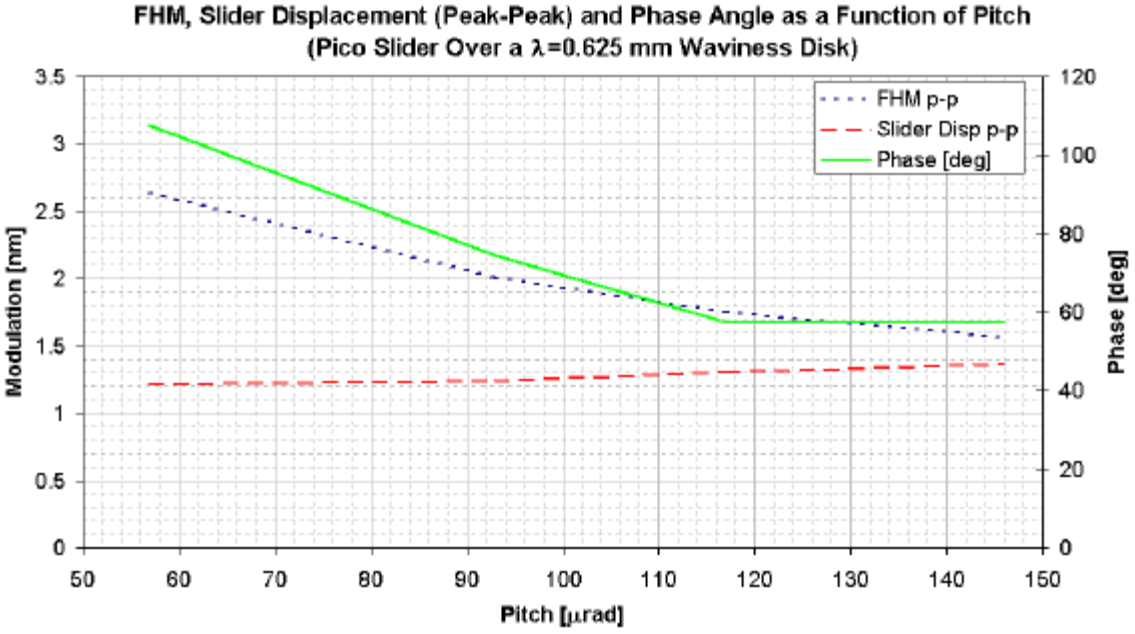

Fig. 3.8. FHM, absolute slider motion, and phase shift as a function of pitch of the 5 nm FH pico sliders for a waviness wavelength of 0.625 mm.

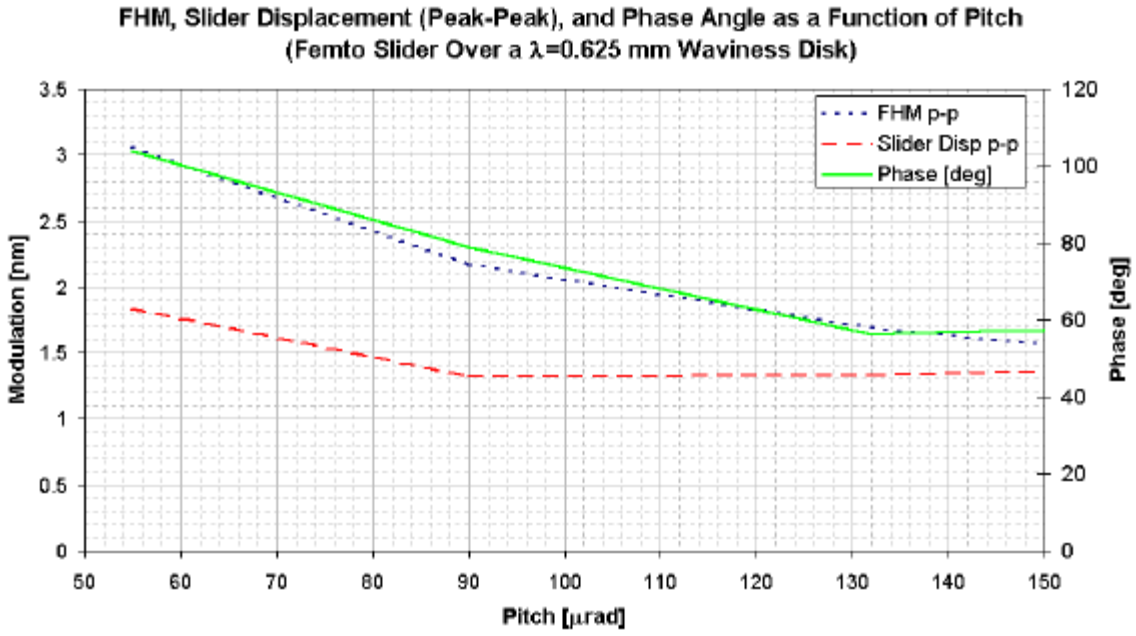

Fig. 3.9. FHM, absolute slider motion, and phase shift as a function of pitch of the 3.5 nm FH femto sliders for a waviness wavelength of 0.625 mm.

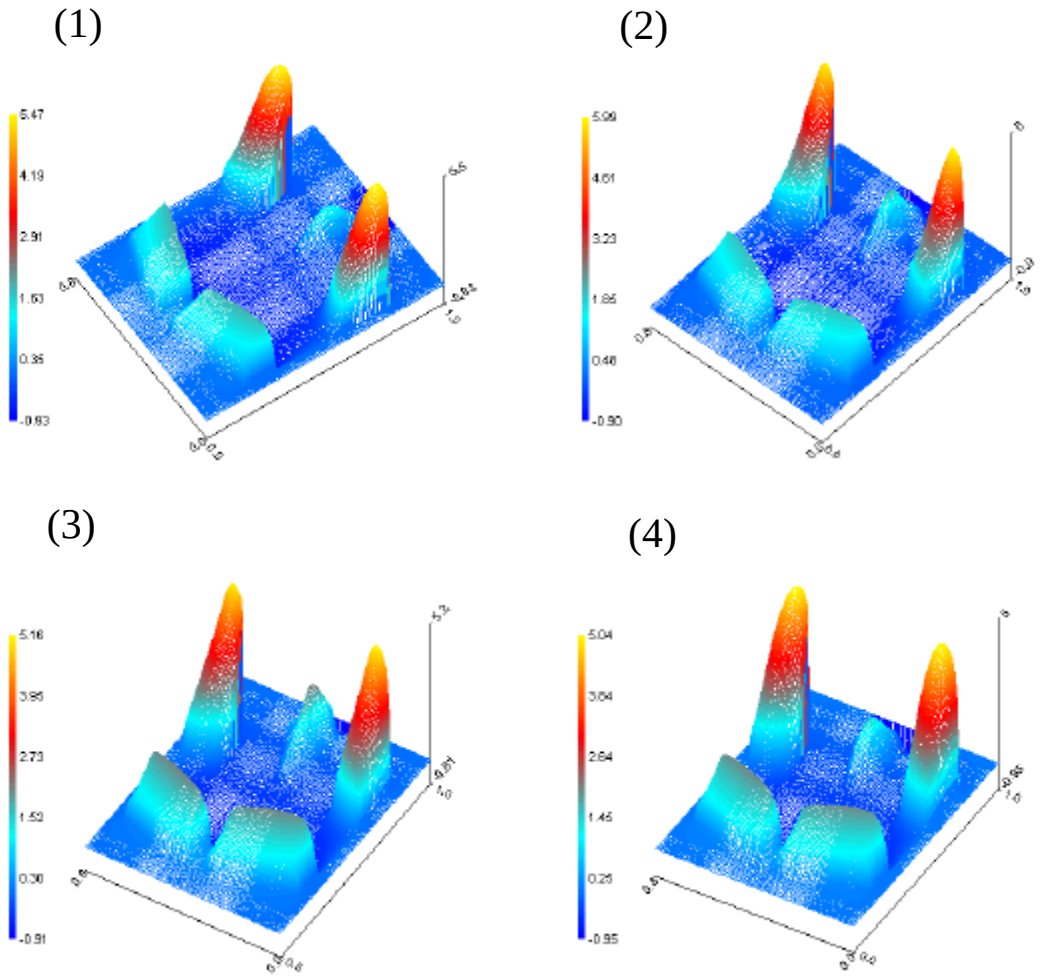

Fig. 3.10. Sequence of pressure profiles for the low pitch femto slider at different disk waviness phase locations. The trailing edge is in a waviness trough in (1), at the mean in (2), at a waviness peak in (3) and again at the mean in (4).

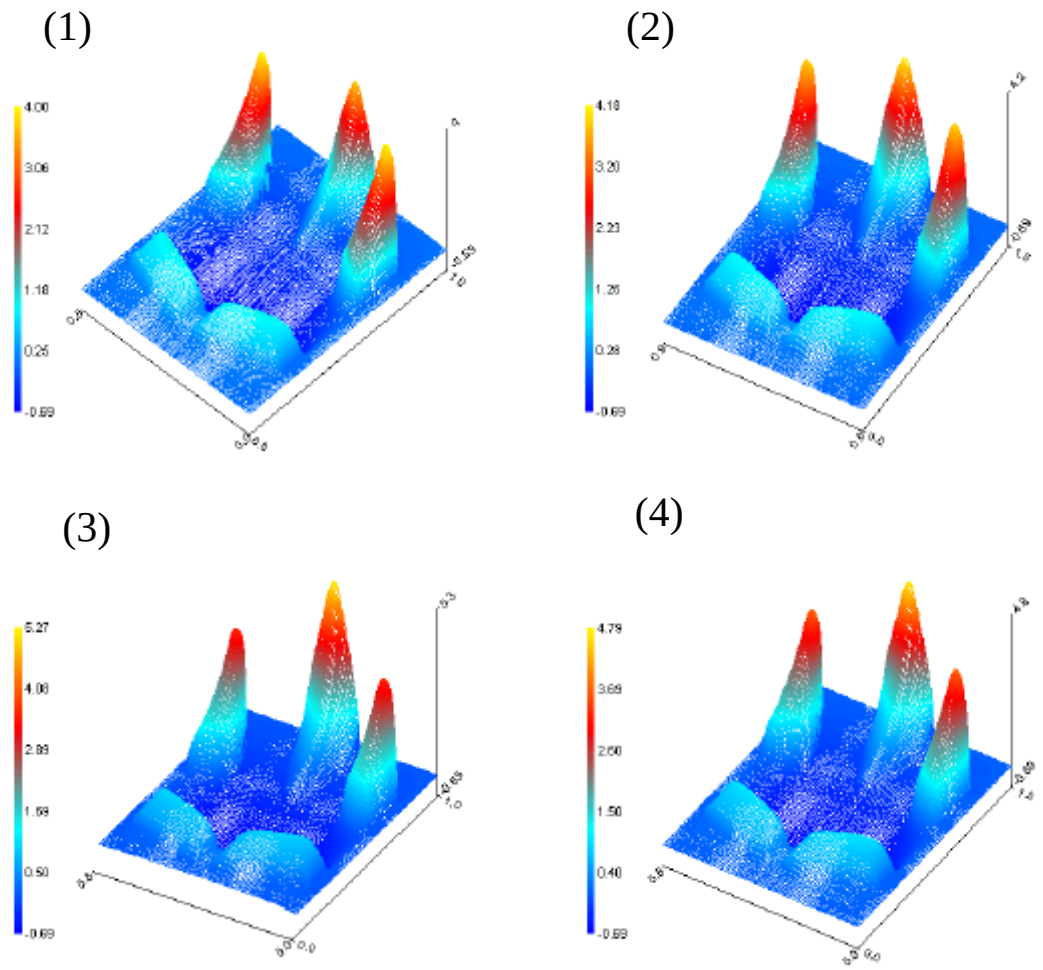

Fig. 3.11. Sequence of pressure profiles for the high pitch femto slider at different disk waviness phase locations. The trailing edge is in a waviness trough in (1), at the mean in (2), at a waviness peak in (3) and again at the mean in (4).

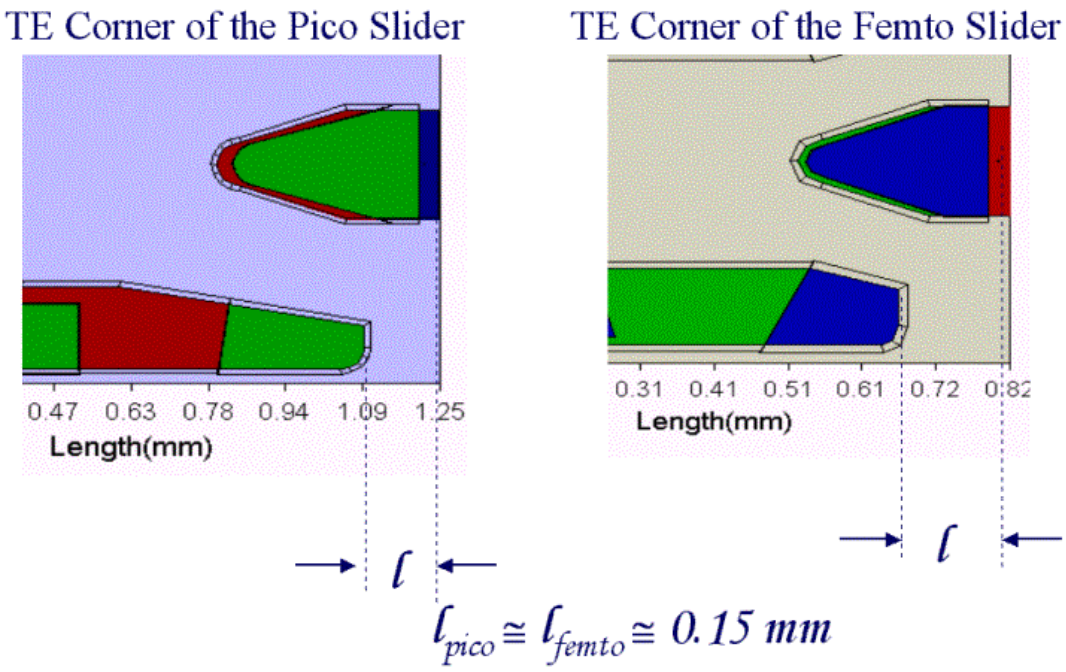

Fig. 3.12. The distance between the trailing edge of the side rails and the trailing edge of the center rail is about 0.15 mm for both the pico and femto slider designs.

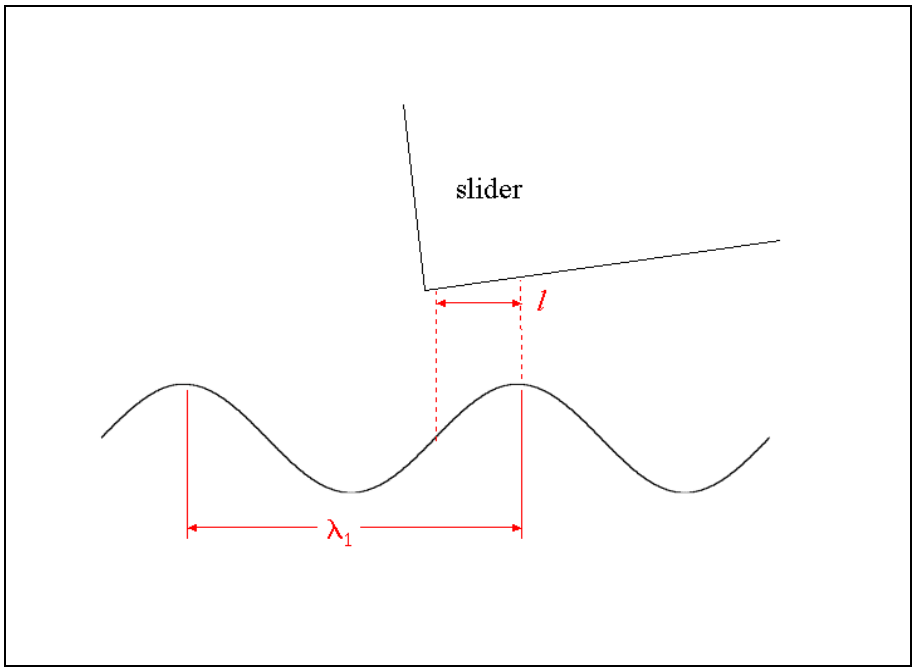

Fig. 3.13. The low pitch slider has pressure points at the trailing edge of the outer rails, which are about 0.15 mm from the transducer. When the waviness wavelength is 0.625 mm, or about ¼ wavelength, the transducer phase lag is about 90 degrees. When the waviness wavelength is 0.325 mm the transducer phase lag is almost 180 degrees.

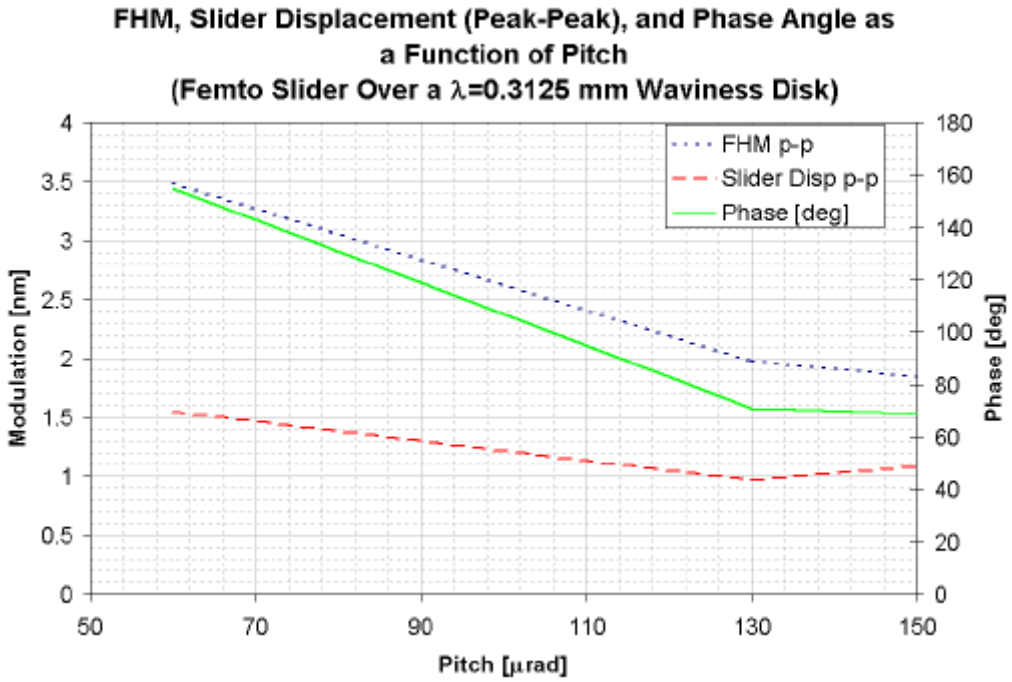

Fig. 3.14. FHM, absolute slider motion, and phase shift as a function of pitch of the 3.5 nm FH femto sliders for a waviness wavelength of 0.325 mm.

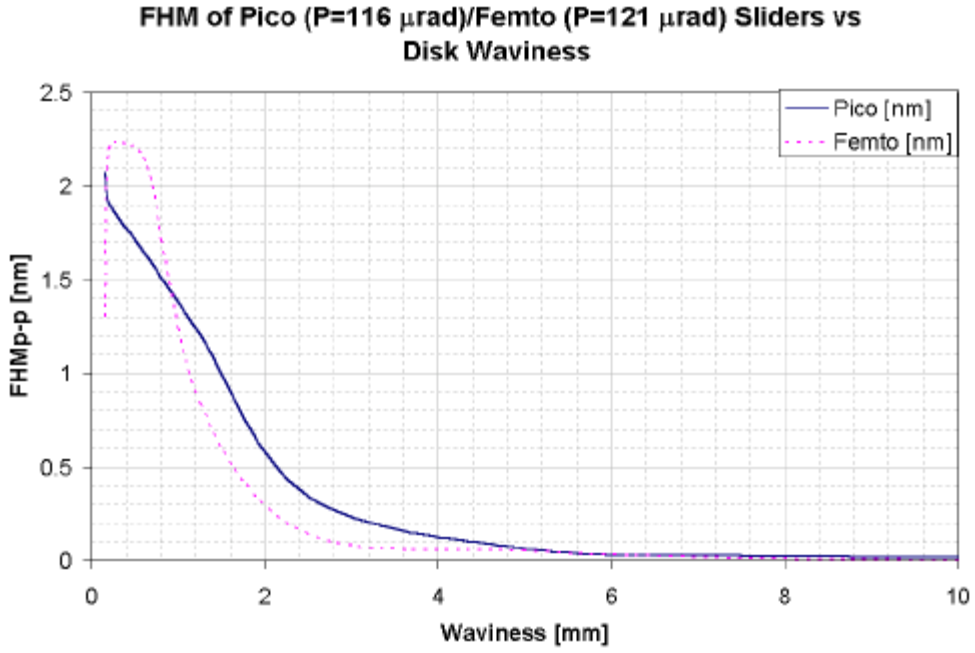

Fig. 3.15. FH modulation as a function of waviness wavelength for the redesigned pico and femto sliders.

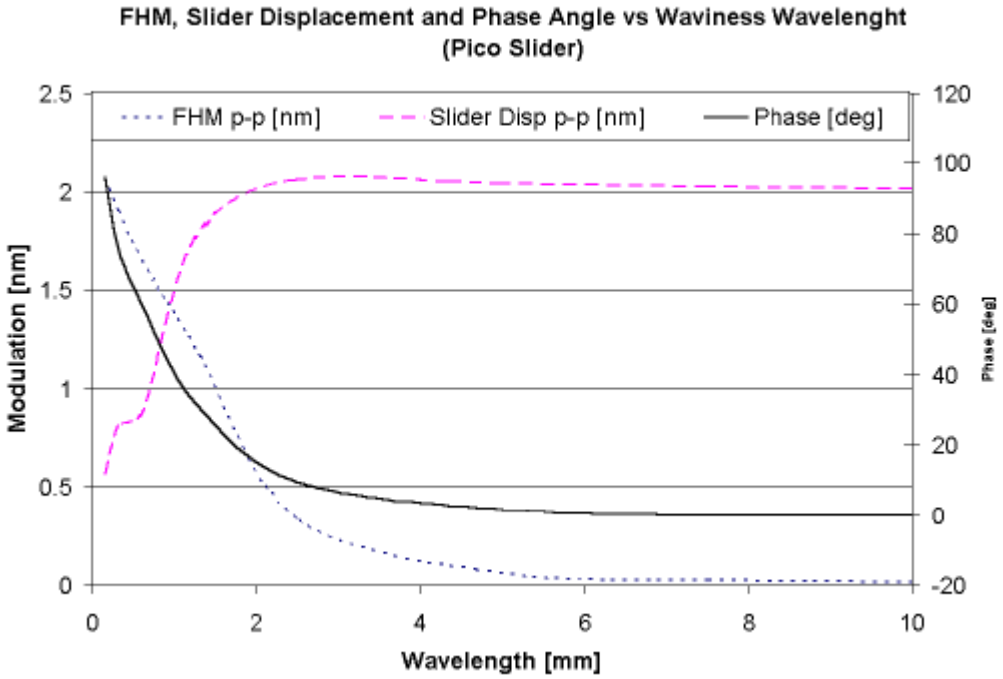

Fig. 3.16. FHM, absolute slider motion, and phase shift as a function of waviness wavelength for the 4 nm FH pico slider.

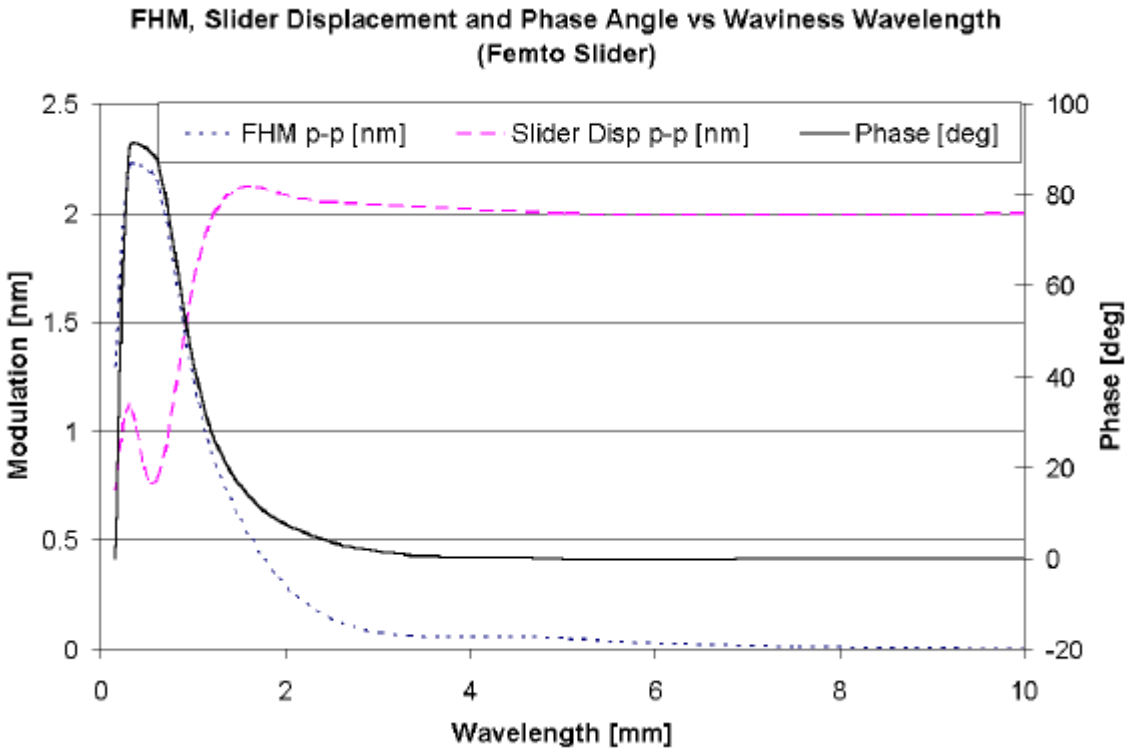

Fig. 3.17. FHM, absolute slider motion, and phase shift as a function of waviness wavelength for the 4 nm FH femto slider.

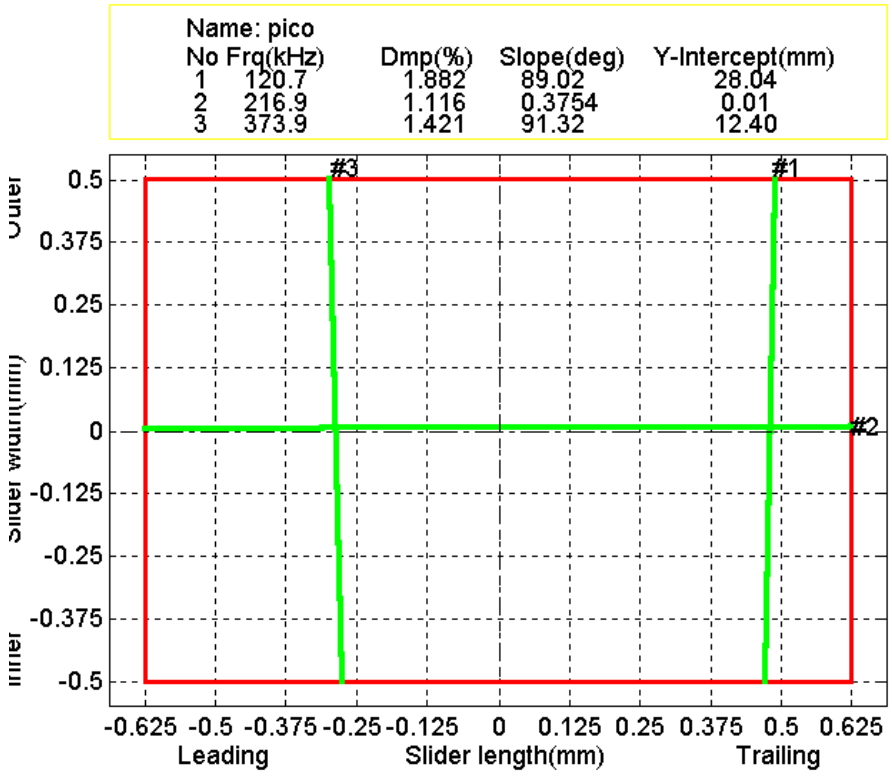

Fig. 3.18. Dynamic characteristics of the redesigned pico slider.

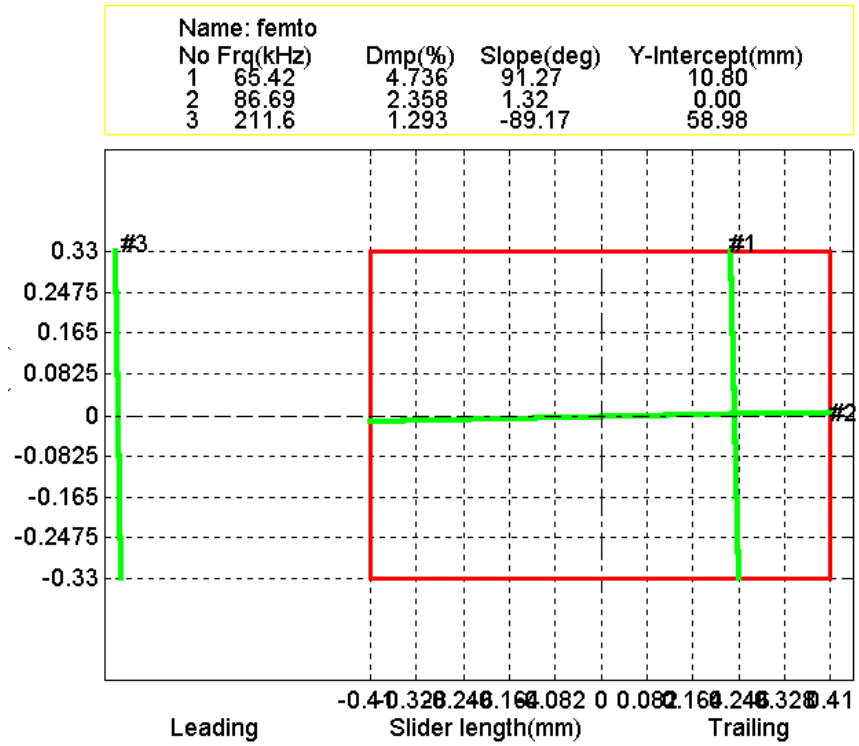

Fig. 3.19. Dynamic characteristics of the redesigned femto slider.

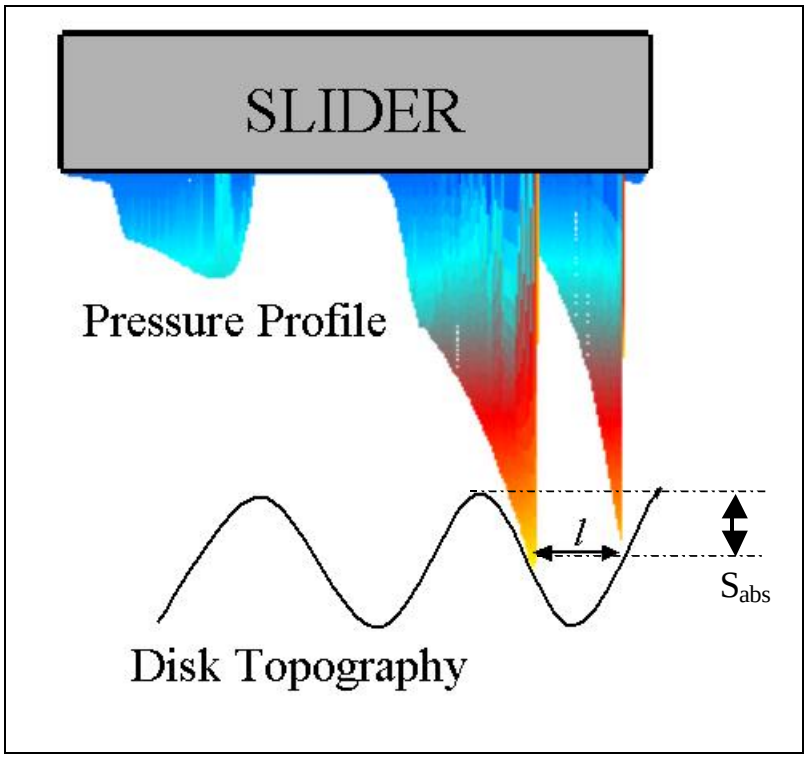

Fig. 3.20. Geometric model for showing how absolute slider motion changes with waviness wavelength.

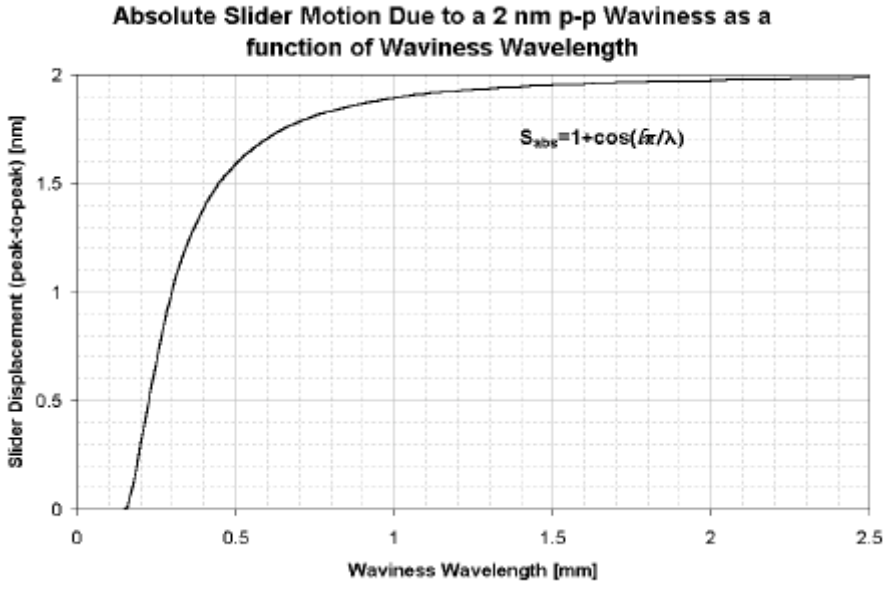

Fig. 3.21. Absolute slider motion as a function of waviness wavelength found from the geometric model.

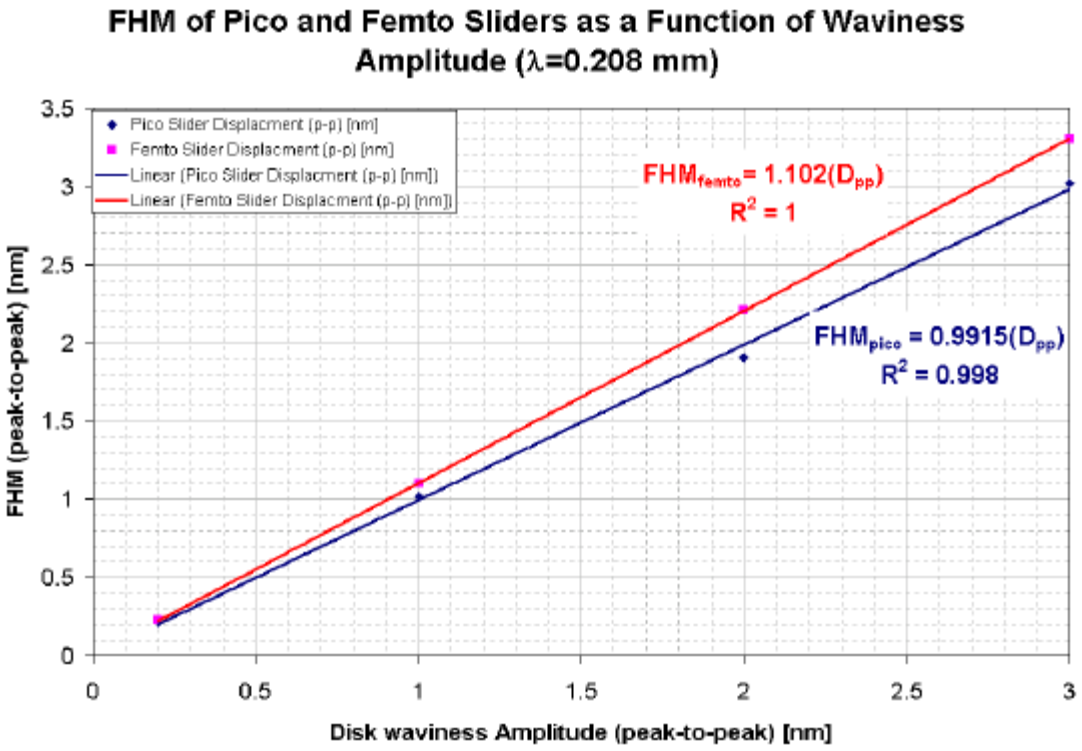

Fig. 3.22. FHM of the pico and femto sliders as a function of waviness amplitude at a waviness wavelength of 0.208 mm.

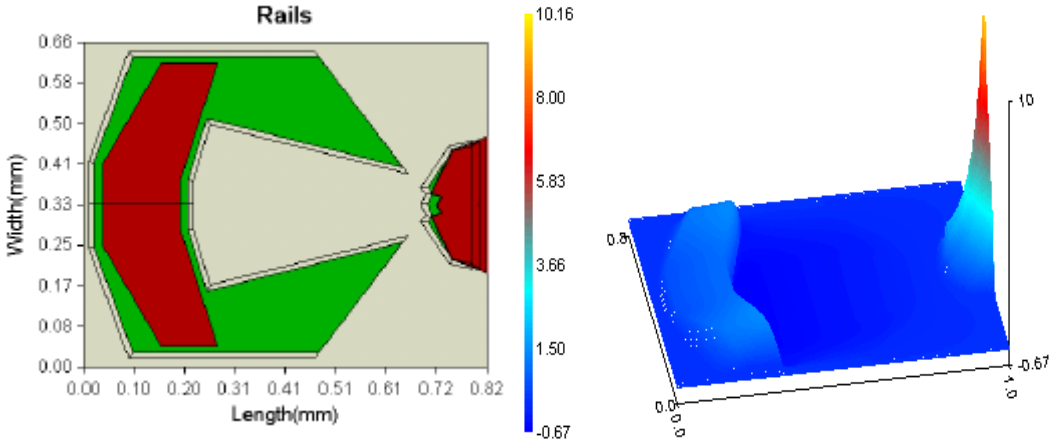

Fig. 3.23. ABS design of the redesigned femto slider and the pressure profile associated with this slider.

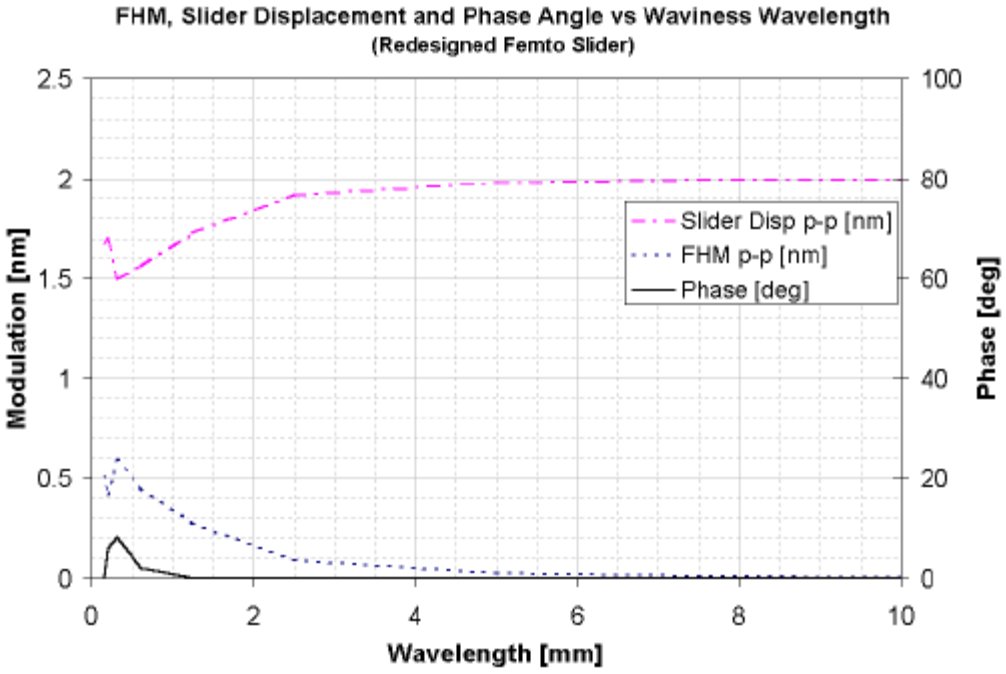

Fig. 3.24. FHM, Slider Displacement and phase angle as a function of disk waviness wavelength for the redesigned femto slider.

CHAPTER 4

A NUMERICAL STUDY OF AIR-BEARING SLIDER FORM-FACTORS

Abstract

This chapter presents a numerical study comparing the performance of air bearing slider form-factors. The air bearing slider and air bearing surface (ABS) design has gone through large changes in recent years in order to achieve the performance required by lower flying heights. In the past, improvements have been achieved by scaling down the form-factors of air bearing sliders. The pico form-factor (1.25 × 1 mm) has been successfully used for several generations of products and the question arises – should the form-factor be scaled down further? The dynamic characteristics and flying-height modulation (FHM) performance of two different ABS designs in the pico and femto (0.82 × 0.66 mm) form-factors were numerically investigated. It was found that for the smaller form-factor designs, greater damping of the air bearing film and slider body system was achieved but with an undesirable decrease in modal frequencies. However, depending on the ABS design, beneficial dynamic properties can be achieved by scaling down the form-factor from pico to femto. Maximizing the total air bearing force (the sum of negative and positive) with a design featuring a large number of transverse pressure gradients can obtain high stiffness and damping. Geometric FHM was also investigated using both sinusoidal disk waviness and an actual measured disk topography. It was found that the FHM depends not only on the form-factor, but also on the ABS design. For long disk waviness wavelengths (longer than the slider body length, L), the FHM is proportional to L^b where $\boldsymbol{b}$ was found to be between 2.6 and 4; hence FHM is dependent

on form-factor. For short disk waviness wavelengths, the FHM is a function of the ABS design and flying attitude and not the form-factor. A disk waviness wavelength of 3 mm demarks the transition above which the FHM is a function of form-factor and below which the FHM is a function of the ABS design, and the superposition of these two effects compose the geometric FHM. Simulations with an actual measured disk topography showed that the femto form-factor exhibited 22% - 32% less FHM than the pico form-factor for a similar design. However, by changing the ABS design, 35% - 40 % less FHM was achievable within the same form-factor. By scaling down a pico slider to a femto slider, we do not necessarily achieve enhanced overall performance. Significant performance improvements in the pico form-factor can be attained if the ABS is properly designed. However, in designing a dynamically stable and low FHM air bearing slider a femto slider ultimately yields better performance when care is taken in designing the ABS.

4.1 Introduction

In the evolution of hard disk drives, there has been a steady trend toward miniaturization of the drives as well as all its components. This miniaturization is motivated by several considerations such as economics, higher areal magnetic densities, access time and data rate, physical space requirements, and new applications other than computer data storage. While the general design of the mechanical components of disk drives has remained relatively fixed, the air bearing slider design has gone through substantial changes. The slider housing the read/write transducer has evolved from a large aluminum externally pressurized hydrostatic slider in 1957 with head/media spacing of 20 μm to today's

complex self-acting ceramic pico (30%: 1.25 mm × 1 mm) air bearing sliders flying at sub-20 nm over the media [6]. The need for more complex air bearing designs stems from the higher bit areal densities requiring a smaller gap, or flying-height (FH) between the transducer and magnetic media. In turn, this has increased the need for a better understanding of the head-disk interface. Shrinking the air bearing slider form-factor has produced many benefits both in cost and in performance. As the FHs approach the sub-5 nm range the question naturally arises: is it time to scale the form-factor down once again too keep up with the rapidly increasing performance criteria?

For a recording density of 1 Tbit/in^2, it is projected that the FH will be 3.5 nm [7]. In order for a reliable head-disk interface to be maintained, contacts between the slider and disk and fluctuations in FH need to be held to a minimum. Therefore, the dynamic performance of air bearing sliders is becoming of increasing importance. At such low FH's, intermittent contacts between the slider and the disk are unavoidable. The more stable the air bearing slider, the less damage will occur and the faster the slider will settle back to its steady-state flying condition once disturbed. Important characteristic parameters controlling the stability are the air bearing modal frequencies and damping ratios. The higher the frequencies and damping ratios, the more stable the interface. The spacing fluctuations between the transducer and disk, or FHM, also needs to be held to a minimum. A large fraction of the FHM is the so-called "geometric" FHM [10], [14], [16]. This FHM occurs due to disk waviness and micro-waviness with significant amplitude in the wavelength range from approximately 8 mm down to the wavelength corresponding to the first air bearing natural frequency – on the order of several hundred

microns [10]. It has been shown for disk waviness wavelengths much longer than the slider body length, L, that the geometric FHM scales proportionally to the square of the slider body length [14]. Also, from more recent studies, in the waviness wavelength regime where the wavelength is comparable to the slider body length, this geometric FHM becomes a very complex function of the ABS geometry and attitude and not the slider's length [10].

In order for manufacturers to decrease the slider form-factor, the benefits must outweigh the costs involved. A study is presented here comparing the dynamic and FHM performance as a function of form-factor and ABS design for two sizes of air bearing sliders.

4.2 Air bearing designs

In this chapter we investigated two ABS designs of different rail complexity. The first design, depicted in Fig. 4.1a, is a five-pad sub-ambient pressure design labeled ABS I. The second and more complicated design is a sub-ambient pressure design shown in Fig. 4.1b labeled ABS II. The transducer is located near the center of the trailing edge of the slider body. ABS I was designed with the following considerations: (1) high stiffness, (2) constant roll angle from inner diameter (ID) to outer diameter (OD), and (3) ease of manufacturing. ABS II was designed with the following considerations: (1) low geometric FHM, (2) high damping, and (3) relatively high stiffness. The simulations were preformed at 7200 RPM, disk radial position of 16.25 mm, and skew angle of zero degrees. Each of the two designs were scaled for pico (30%: 1.25 X 1 mm) and femto

(20%: 0.82 X 0.66 mm) form-factors. In changing the form-factor, the geometry of the rails, recess heights, crown, and camber of the ABS's were scaled proportionally as seen in Table 4.1. The additional features on the leading edge of ABS II protrude 40 nm from the ABS. These additional features serve to increase damping (as will be discussed) and could be manufactured similar to diamond-like carbon pads used on padded "stiction-free" sliders. For this study the FH at the transducer was kept approximately the same for all designs, but due to the highly non-linear nature of the generalized Reynolds equations, the gram-load could not simply be scaled down proportionally, as seen in Table 4.1. The static attitude of each ABS is also shown in Table 4.1. ABS I and ABS II were designed for transducer FHs of 7 nm and 5 nm, respectively for 100 Gbit/in^2 and greater areal recording density applications. Figures 4.2a and 4.2b show the pressure profiles with the pressure values normalized by the ambient pressure generated under the ABS I and ABS II sliders in the pico form-factor, respectively. For each slider design, the pressure profile geometry remained relatively constant, independent of form-factor with differences only in the amplitudes of pressure. The high pressure generated at the side rails of ABS I help achieve high stiffness (especially in the roll motion) and constant roll angle from ID to OD. The features on the trailing edge pad of ABS II help generate high pressure near the transducer location decreasing the geometric FHM and the large number of pressure gradients generated on the leading edge pads increase the air film damping [10], [17].

4.3 Dynamic system properties of the air bearing slider

The air bearing film and slider body form a complex coupled non-linear dynamic system. By using the CML Dynamic Air Bearing Simulator, which solves the generalized

Reynolds equations coupled with the dynamics of the slider body and a lumped parameter suspension, we are able to simulate the dynamic response of the slider for various inputs. For small perturbations about the slider's steady flying attitude the non-linearities are small and linear modal analysis can be used to obtain the modal parameters of the air bearing slider system. This system is modeled as a three degree-of-freedom (DOF) system – the vertical, pitch and roll motions. By simulating the response of the slider to initial velocities in all three DOFs, we can estimate the impulse response functions and perform modal analysis to obtain the modal masses, stiffnesses, damping ratios and nodal lines [17]. The modal frequencies and damping ratios are shown in Figs. 4.3 and 4.4 for the ABS I and ABS II designs, respectively, for the two form-factors investigated. Modes 1, 2 and 3 correspond to the three coupled modes generally called pitch, roll, and vertical or first-pitch, roll and second-pitch. For the ABS I designs, modes 1, 2 and 3 correspond to the first-pitch, roll, and second-pitch, respectively. For ABS II, modes 1, 2, and 3 correspond to roll, first-pitch and second-pitch, respectively. The modal parameters are dependent on the pressure profile generated under the ABS and the size and mass of the slider body. The nodal lines or mode shapes remain relatively fixed for each design regardless of form-factor as expected by the relatively constant pressure profiles generated by each design in the two form-factors. However, the modal stiffnesses and damping ratios changed quite significantly with form-factor, as seen in Figs. 4.3 and 4.4, due to several effects.

As the sliders decrease in size, all three modal frequencies of both slider designs decrease. This result my seem counter-intuitive initially due to the smaller mass of the

smaller form-factor (i.e. the modal frequency w_i @ $(k_i/m_i)^{0.5}$), however the stiffness decreases significantly more than the mass causing the modal frequencies to ultimately decrease with decreasing form-factor.

There are two effects that cause the stiffness to decrease as slider size decreases. As the form-factor decreases, so does the bearing load capacity – the ability of the air bearing to create positive and negative forces. For a decrease in length dimension by 33 % (pico to femto) the ABS area decreases by 56 %. The forces generated by the air film are related to the area that the air pressure acts over; hence by decreasing the area, we also decrease the bearing load capacity. ABS I decreases its load capacity by 60 % and 58 % to produce positive and negative force, respectively as seen in Table 4.1. Similarly, ABS II decreases its load capacity by 48 % and 53 % to produce positive and negative force, respectively. The ability of a slider design to retain load capacity while reducing the form-factor helps it to maintain a stiff air bearing film. Scaling the form-factor from pico to femto causes total force (positive force + | negative force |) to decrease by 59% and 51% for ABS I and ABS II, respectively. The ability of ABS II to retain a larger percentage of the total force helps it retain its stiffness as the form-factor is decreased.

Peak pressures generated by the air bearing can also have an effect on air bearing stiffness. The higher a pressure peak, the stiffer the local area will be. ABS I contains three high pressure points – one at the trailing edge pad and two on the side rails demarked in Fig. 4.2 as locations A and B. These three locations can be viewed as three stiff distributed springs over the local areas of the pads. When the form-factor decreases

from pico to femto, the overall effectiveness of these three springs decreases as the peak pressures decrease (see Table 4.2). However, ABS II has only one high pressure point located on the trailing edge pad as seen in Fig. 4.2, and as the form-factor decreases from pico to femto, the peak pressure actually increases. This increase in peak pressure helps to maintain the stiffness of ABS II in the femto form-factor. This is most effective in retaining the stiffness of the pitch modes exhibiting a decrease of only 4.6 % in stiffness for ABS II when it is scaled down from pico to femto as compared to a 30.4 % decrease in stiffness of ABS I. The three high pressure points on ABS I provide the characteristic high stiffness, especially in the roll direction, however, when it is scaled down from pico to femto, the peak pressures at all three points decrease, hence causing a decrease in all three modal frequencies.

Desirable higher damping ratios were obtained with the femto form-factor as compared to the pico form-factor for both ABS designs. It has been shown previously that the stiffer the air bearing film, the smaller the damping will be (achieved through the transverse viscous shearing [17]-[20]). This holds true for ABS I and ABS II – the femto form-factors have lower stiffnesses than the pico, and hence, higher damping ratios. ABS I had an increase in damping ratios of 1 % to 28 % while ABS II had an increase in damping ratios by at least 30% when scaling the form-factors from pico to femto. Textured ABS designs and disks have been studied and have been shown to enhance the damping characteristics of the air film [17], [18], [21]. The extra pads that are located on top of the leading edge surface of ABS II cause multiple pressure gradients designed to increase damping. From the modal analysis results, it is seen that in comparing the pico form-

factors, ABS II exhibits an increase of 21 %, 428 %, and 195 % in damping ratios over ABS I for the pitch, roll, and vertical modes, respectively. Similarly, in comparing the femto form-factors, ABS II exhibited 26 %, 480 %, and 346 % increase in damping ratios over ABS I of the pitch, roll, and vertical modes, respectively.

4.4 Air bearing flying-height modulation

It has been shown in the previous two chapters that geometric FHM due to disk waviness and micro-waviness can be comparable to the FH. It also has been known for some time that for waviness wavelengths much longer than the sliders overall body length the FHM scales proportionally to the square of the slider's length [14]. However, when the waviness wavelength approaches the sliders length, we showed in Chapter 3 that the FHM is a complex function of the ABS design, and it is independent of the overall length of the slider. In order to assess how each ABS design and form-factor is affected by disk waviness, we performed simulations using a modeled sinusoidal disk waviness, *d(x)*, for which the wavelengths, λ, ranged from 20 mm to 0.3125 mm:

$$d(x) = A\sin\left(\frac{2\pi}{\lambda}x\right) \tag{4.1}$$

In this wavelength range, the dynamic resonant modes of the air bearings are not excited and the FHM is a result of geometric effects and not dynamics. The results of the simulations are shown in Figs. 4.5 and 4.6. These figures show amplitude ratios of the FHM peak-to-peak ($FHM_{p\text{-}p}$) over the disk waviness amplitude peak-to-peak ($DISK_{p\text{-}p}$), or the "gain" as a function of disk waviness wavelength on a log-log scale. These results are similar to those presented in Chapter 3. The predicted behavior is present, with low gain for disk waviness wavelengths much longer than the slider body length, and with the

gain exponentially increasing as the wavelength approaches the slider body length. It is also seen, for long wavelengths, that the larger form-factors exhibit larger gain. However, as the wavelength decreases, the gain becomes dependent on the ABS design and independent of form-factor. This can be seen more clearly in Fig. 4.7 where the data plotted in Figs. 4.5 and 4.6 are plotted on the same plot on a linear-linear scale. There appears to be a transition waviness wavelength (depicted in Fig. 4.7) at approximately 3 mm – above which the FHM is dependent on the form-factor and below which the FHM is dependent on the ABS design. This dependence on geometry (sliders length and/or ABS design) can been seen in Figs. 4.8 and 4.9. These figures show the form-factor FHM ratios or gains $\left((FHMgain)_{femto}/(FHMgain)_{pico}\right)$ for the same design plotted as a function of waviness wavelength. It can bee seen from Figs. 4.8 and 4.9 that in the waviness wavelength range of 7.5 mm to 20 mm the curve is constant. Below 7.5 mm the curves transition and increase to 100 % and beyond as the waviness wavelengths approach 0.3125 mm.

For ABS I and ABS II the average values of the form-factor FHM ratios from waviness wavelength 7.5 mm to 20 mm are 52 % and 29 %, respectively. In this region, the FHM can be explained by Zhu's work showing that the FHM is proportional to the square of the slider length and the combined curvature of the slider and disk [14]:

$$FHM \propto L^2 Z'' \tag{4.2}$$

From this formulation, the form-factor FHM ratios should be:

$$\frac{FHM_{femto}}{FHM_{pico}} = \frac{L_f^2 \cdot Z_f''}{L_p^2 \cdot Z_p''} = \frac{\left(2/3\right)^2 \cdot L_p^2 \cdot \left(3/2\right) \cdot Z_p''}{L_p^2 \cdot Z_p''} = 66.7\% \tag{4.3}$$

where L_p and L_f are the lengths of the pico and femto sliders, respectively and Z''_p and Z''_f are the curvatures of the pico and femto sliders, respectively, calculated from the crown, *Z*, of the sliders:

$$Z(x) = 4R\left(\frac{x}{L} - \left(\frac{x}{L}\right)^2\right) \tag{4.4}$$

where *R* is the maximum value of crown shown in Table 4.1 and *x* is in the length direction of the slider. However, Zhu's formulation was for a simple taper-flat positive pressure slider and further simplified assuming a constant distributed pressure along the rails. The ABS designs evaluated in this study are much more complex, and it is found that for waviness wavelengths greater than 7.5 mm, the form-factor FHM ratios scale as $L^{2.6}$ and L^4 for ABS I and ABS II, respectively.

Below waviness wavelengths of 7.5 mm another mechanism causes geometric FHM. It was shown in Chapter 3 that this geometric FHM is dependent on the ABS design and flying attitude (specifically the pressure profile), and the waviness wavelength. This geometric FHM is primarily due to a phase shift between the slider's response at the transducer and the disk, f, and secondarily due to an amplitude change, *B*. In this waviness wavelength range, 0.3125 mm to 7.5 mm, the slider's displacement can be written as:

$$s(x) = B\sin\left(\frac{2p}{l}x + f\right) \tag{4.5}$$

In order to calculate the FHM gain, we subtract the disk's displacement in Eq. (4.1) from the slider's displacement in Eq. (4.5) and normalized by the disk's amplitude:

$$FHM_{geo} = \frac{B}{A}\sin\left(\frac{2\pi}{l}x + \phi\right) - \sin\left(\frac{2\pi}{l}x\right) \tag{4.6}$$

This geometric FHM is the difference of two sinusoids with the same frequency but with different amplitude and a phase shift. This is illustrated in Fig. 4.10 which shows the disk and slider displacements for ABS I in the pico form-factor for a disk waviness wavelength of 0.625 mm. The normalized amplitude, B/A, and the phase shift, ϕ, are known to be dependent on a characteristic length, l, which is dependent on the ABS design and pressure profile rather than the slider's body length as was shown in Chapter 3. As the waviness wavelength decreases from 7.5 mm to 0.3125 mm, the form-factor FHM ratios for both ABS I and ABS II approach 100 %, showing that both form-factors exhibit similar levels of geometric FHM.

Clearly, for long waviness wavelengths, the ABS designs in the smaller form-factors out perform the larger form-factors. However, the FHM gain for long waviness wavelengths is extremely small, so the contribution to FHM is small. As the waviness wavelengths approach the length of the sliders, the amplitude ratios in Figs. 4.8 and 4.9 reach approximately 100%, showing FHM in this waviness wavelength range is independent of form-factor. By comparing ABS I to ABS II in Fig. 4.7, we see that the ABS II design exhibits approximately 50% less maximum FHM gain than the ABS I design for wavelengths in the vicinity of the slider body length for both form-factors. This result shows that ABS II is much less susceptible to geometric FHM than ABS I. Figures 4.8 and 4.9 are informative in comparing the ratio of $FHM_{p\text{-}p}$ / $DISK_{p\text{-}p}$ between form-factors of the same ABS designs, however it is useful to understand how this translates to FHM for an actual disk topography.

When the disk rotates, the disk's out-of-plane motion is composed of clamping distortions, disk flutter, and disk morphology, including waviness, micro-waviness and roughness in order of low to high frequency or long to short wavelength. For a typical "super-smooth" disk used in sub-10 nm FH applications, the out-of-plane displacement amplitudes decrease approximately exponentially as frequency increases or as wavelength decreases. Figures 4.11 and 4.12 show the FHM ratios for the ABS designs in the pico and femto form-factors and a measured typical "super-smooth" disk topography as a function of waviness wavelength. The disk displacement amplitudes were measured with a laser Doppler vibrometer and include wavelengths from 20 mm down to 0.3125 mm. To obtain the corresponding FHM, the disk amplitude was multiplied by the FHM ratio in Figs. 4.11 and 4.12. As shown in Figs. 4.11 and 4.12 the disk amplitudes follow approximately an exponentially increasing function of waviness wavelength and the FHM ratio is approximately an exponentially decaying function of waviness wavelength. However, the FHM ratio curve decays faster than the disk function curve increases, so that when these two curves are combined to get FHM, the shorter waviness wavelengths influence the FHM more than the longer wavelengths.

In order to quantitatively compare the ABS designs and form-factors, we performed simulations using the measured disk topography. These simulation results are summarized in Table 4.3, which includes peak-to-peak and standard deviation (σ) of the FHM for ABS I and ABS II for the pico and femto form-factors. ABS I exhibited 22% less FHM for the femto than for the pico form-factor. Similarly, ABS II exhibited 32%

less FHM for the femto than for the pico form-factor. Comparing only form-factors with the same ABS design, we see a significant decrease in FHM for the smaller form-factor. However, in cross-comparing ABS designs, ABS II is found to have 35%-40% less FHM than ABS I with the same form-factor. Additionally, ABS II in the pico form-factor exhibited 22% less FHM than ABS I in the femto form-factor.

4.5 Discussion

By changing the form-factor of ABS designs and holding the design constant, we studied form-factor effects on dynamic and FHM performance. From the dynamic system properties, it is observed that, in general, the air bearing stiffnesses detrimentally decrease while the damping ratios beneficially increase as the form-factor is scaled from pico to femto. However, it is seen that these modal parameters determining the dynamic stability of the system do not scale proportionally with form-factor and are highly dependent on ABS design. The dynamic performance of ABS II is better than that of ABS I for two reasons. Firstly, it has the ability to maintain its stiffness by retaining a larger percentage of its bearing load capacity and by creating a higher peak pressure as the form-factor is scaled down from pico to femto. Secondly, the large number of transverse pressure contours on ABS II makes it highly damped compared to ABS I in both form-factors. Overall, a design's dynamic properties may not be enhanced by simply decreasing the form-factor. However with the proper design, both the modal stiffness and damping ratios can remain large leading to a dynamically more robust air bearing slider.

Another extremely important performance consideration is FHM. The largest contributor to FHM can be the geometric FHM, which is due to the disk morphology and other out-of-plane disk motions. The FHM ratios for the designs investigated were lower in amplitude for the smaller form-factor sliders for waviness wavelengths much longer than the slider body length. The femto form-factors exhibited 50% - 80% less FHM for long waviness wavelengths than the pico form-factor. However, as the disk waviness wavelength approach the slider body length, the FHM ratio becomes dependent on the ABS design and independent of form-factor. The ABS I design exhibited a gain in FHM ratio, approaching 100% and even slightly above 100%, for waviness wavelengths around the slider body length. However, for ABS II, a maximum FHM ratio of 50% was attained, half as much when compared to ABS I – regardless of form-factor.

To quantitatively compare form-factors and cross compare ABS designs, we conducted simulations using an actual measured disk topography. In comparing FHM for the same design, it was found that the smaller femto form-factor exhibited 22% - 32% less FHM than the larger pico form-factor. However, when cross comparing ABS designs, an even larger decrease in FHM was observed. The ABS II design demonstrated 35% - 40% less FHM compared to the ABS I design for both form-factors, pico and femto. Additionally, it was found that the pico form-factor of the ABS II design showed 22% less FHM compared to the femto form-factor of the ABS I design.

4.6 Conclusion

By comparing the dynamic and FHM performance of pico and femto form-factor air bearing sliders designed for 100 Gbit/in^2 applications, it was found that the smaller form-factor exhibited an overall enhancement in performance when the ABS is properly designed. A beneficial increase in damping ratios and a detrimental decrease in modal stiffnesses was observed when scaling the form-factor from pico to femto. However, it was seen that if the ABS is designed to retain a larger percentage of its bearing load capacity and can maintain high peak pressure(s), the stiffness is not compromised dramatically by scaling down the form-factor. Also, a large number of transverse pressure gradients are extremely effective in increasing damping, and they further increase damping when the form-factor is scaled from pico to femto. FHM due to geometry is composed of the superposition of two effects dependent on the overall length of the slider for long disk waviness wavelengths and dependent on the ABS design for shorter disk waviness wavelengths. For long waviness wavelengths, FHM was shown to be dependent on the sliders body length: proportional to $L^{2.6}$ and L^4 for ABS I and ABS II, respectively. For shorter waviness wavelengths, FHM was shown to be dependent on the ABS design and a phase shift between the slider's response at the transducer and the disk as well as an amplitude change in the slider's displacement. These two effects are demarked by a transition disk waviness wavelength of approximately 3 mm. By comparing femto to pico form-factors, it is seen that the femto exhibited lower FHM for waviness wavelengths greater than the sliders body length, however, it demonstrated similar levels of FHM for waviness wavelengths less than the sliders body length. By cross comparing ABS designs, it was found that significant improvements in FHM performance can also be

attained by changing the ABS design and not decreasing the form factor. Simulations were performed using an actual measured disk topography which showed a decrease of 22 % to 32 % in FHM by scaling down the form-factor from pico to femto. However, by cross-comparing ABS designs, ABS II exhibited much less FHM even in comparing ABS II in the pico form-factor to ABS I in the femto form-factor. It is concluded that by simply scaling down the form-factor, enhanced performance is not always attained. However if special care is taken in the design of the ABS in order to maintain stiffness, increase damping and decrease geometric FHM, major improvements can be attained. Ultimately, to achieve the greatest performance, a smaller form-factor should be used with special care taken in the ABS design.

	Air Bearing Design			
	ABS I		ABS II	
Form-Factor	Pico	Femto	Pico	Femto
Gram-Load [gm]	1.50	0.70	1.90	0.75
Positive Force [gm]	4.76	2.00	4.83	2.28
Negative Force [gm]	-3.26	-1.30	-2.93	-1.53
Pitch [μrad]	123.50	142.70	95.60	101.50
Roll [μrad]	-1.58	-1.43	-5.08	-2.97
Transducer FH [nm]	7.0	7.3	4.8	4.9
Crown [nm]	25.4	16.9	25.4	16.9
Camber [nm]	2.5	1.7	2.5	1.7
Base Recess [um]	2.5	1.7	2.5	1.7
Step Recess [um]	0.3	0.2	0.3	0.2

Table 4.1. Air bearing specifications and static flying attitude solution.

	Air Bearing Design			
	ABS I		ABS II	
Form-Factor	Pico	Femto	Pico	Femto
Normalized Peak Pressure (location A)	3.70	3.15	10.75	12.62
Normalized Peak Pressure (location B)	5.84	5.04	N/A	N/A

Table 4.2. Normalized peak pressures at locations A and B demarked in Fig 2 for ABS I and ABS II in the pico and femto form-factors.

	Air Bearing Design		
	ABS I	ABS II	ABS II / ABS I [%]
Femto Peak-to-Peak [nm]	1.52	0.90	**59%**
Femto σ [nm]	0.23	0.15	**63%**
Pico Peak-to-Peak [nm]	2.04	1.33	**65%**
Pico σ [nm]	0.30	0.18	**61%**
Femto/Pico (Peak-to Peak)	**74%**	**81%**	
Femto/Pico (σ)	**78%**	**68%**	

Table 4.3. FHM results from simulations with actual measured disk topography for ABS I and II in pico and femto form-factors.

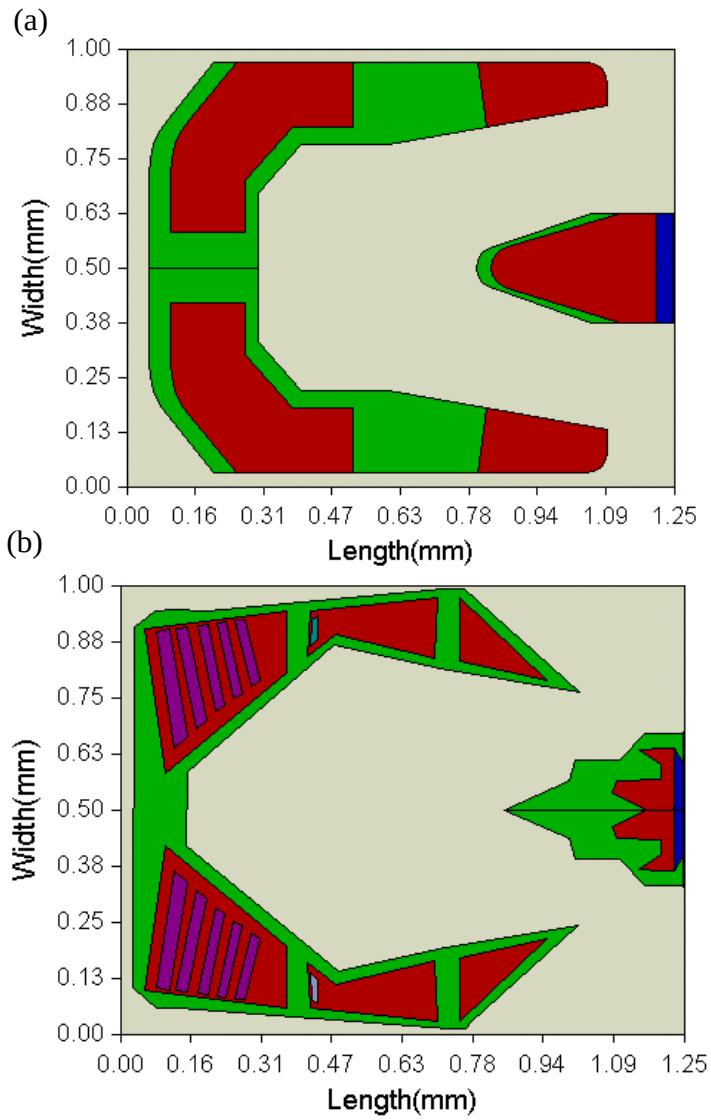

Fig. 4.1. Air bearing surface designs: (a) ABS I and (b) ABS II.

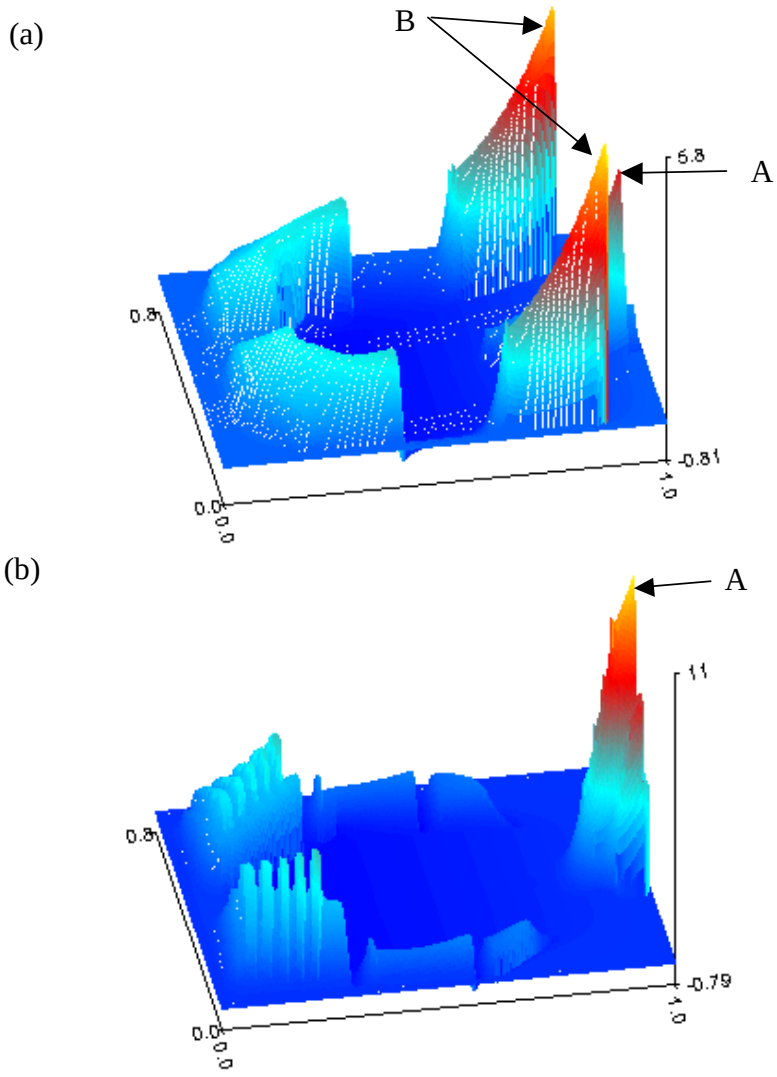

Fig. 4.2. Pressure profile generated by (a) ABS I, and (b) ABS II.

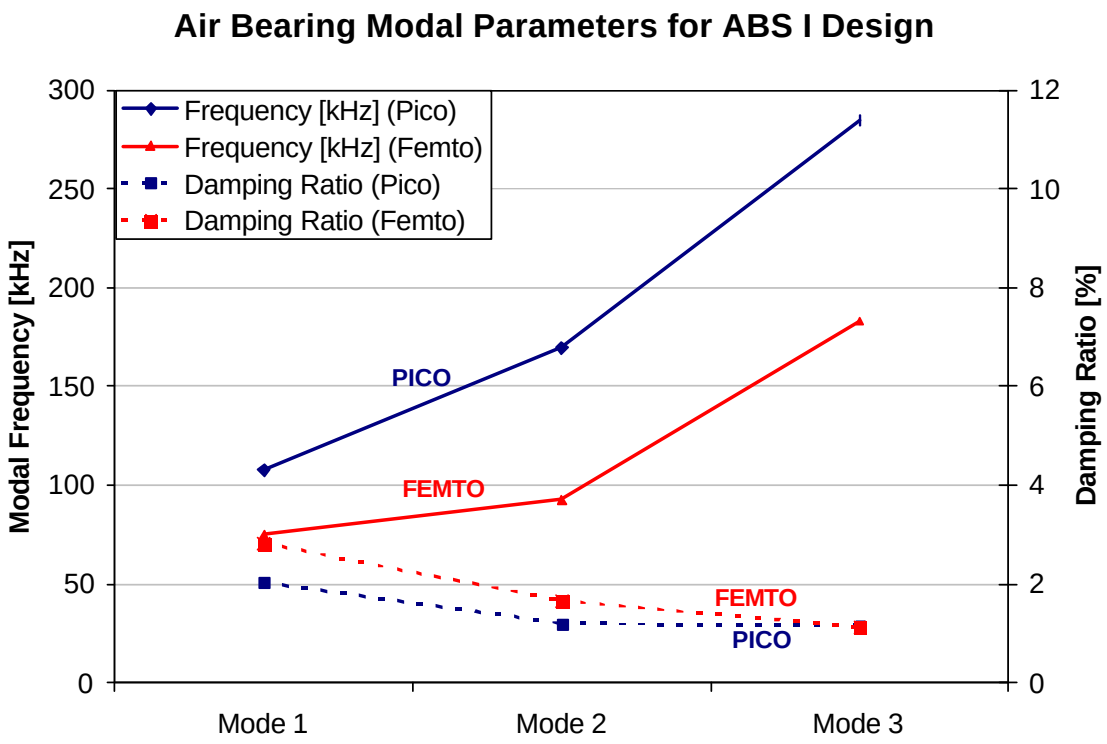

Fig. 4.3. Modal frequencies and damping ratios of the ABS I designs for the pico and femto form-factors.

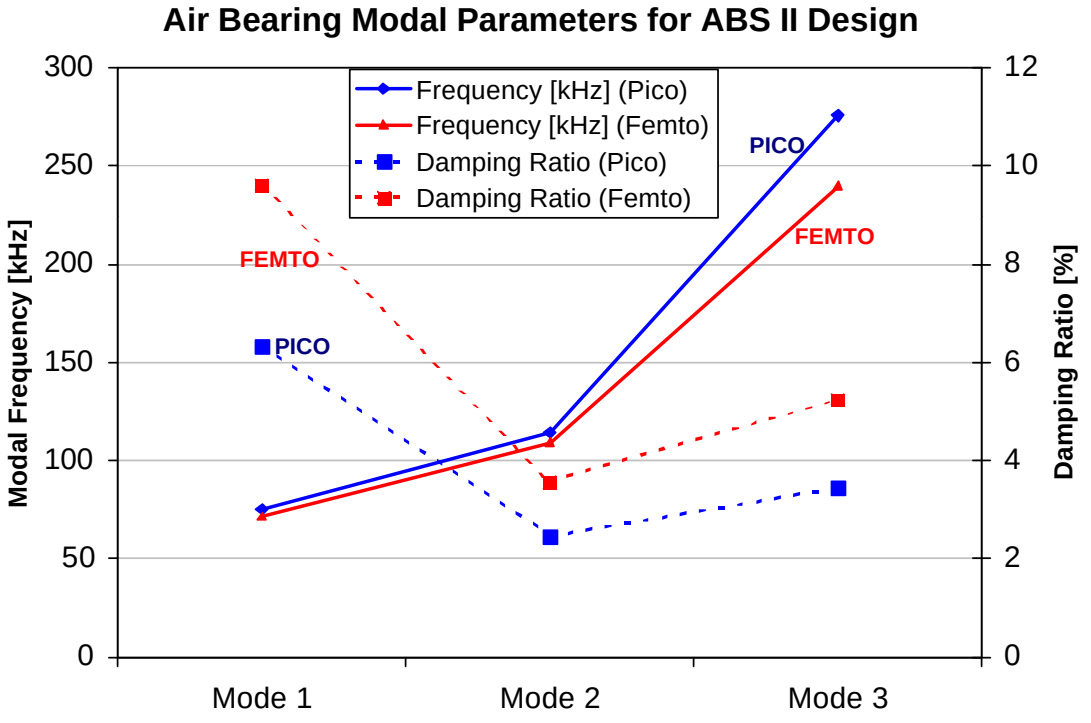

Fig. 4.4. Modal frequencies and damping ratios of the ABS II designs for the pico and femto form-factors.

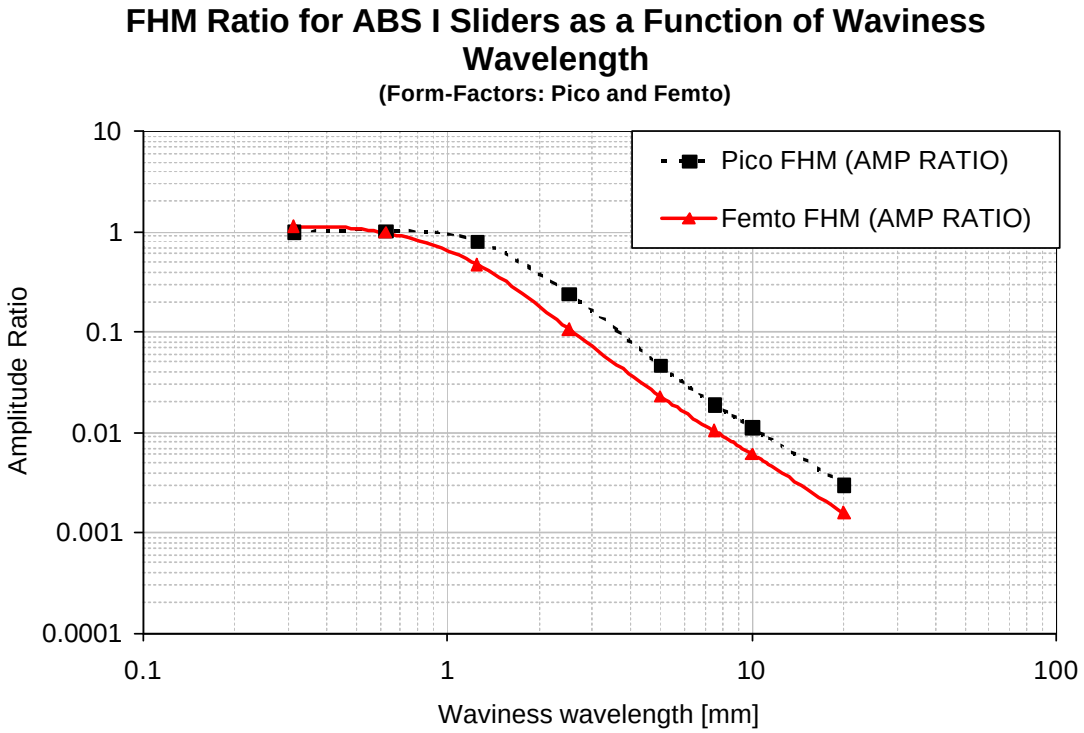

Fig. 4.5. FHM ratio or gain for the ABS I design ABS's as a function of disk waviness wavelength.

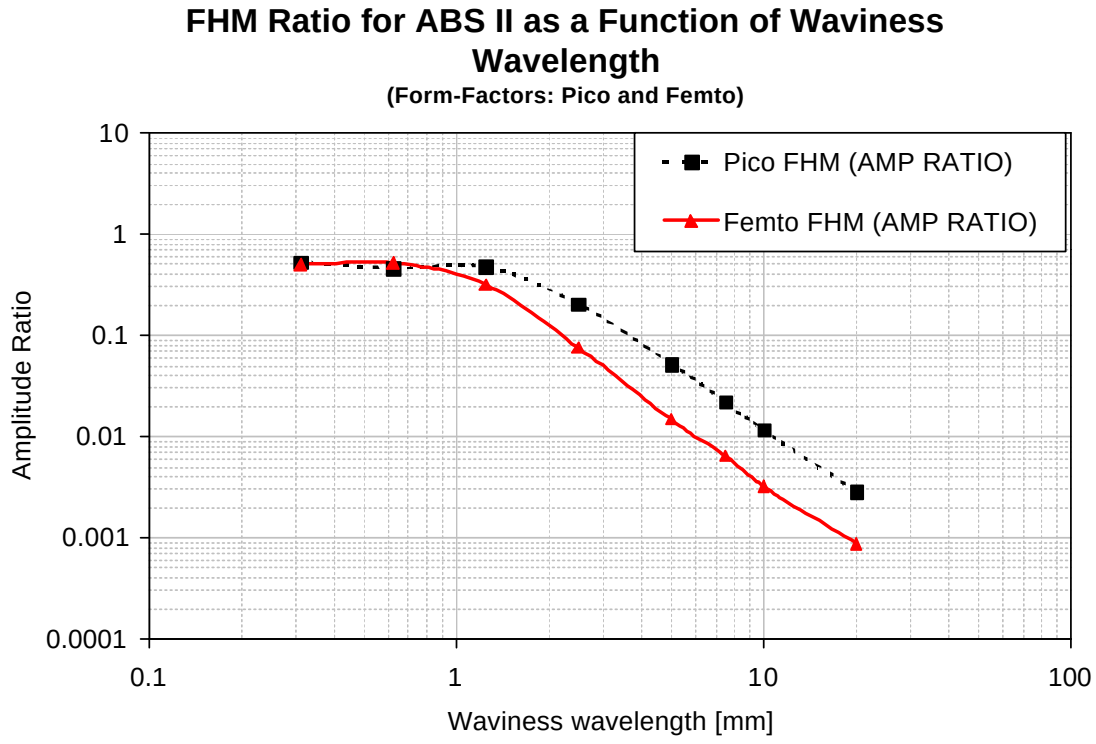

Fig. 4.6. FHM ratio or gain for the ABS II design ABS's as a function of disk waviness wavelength.

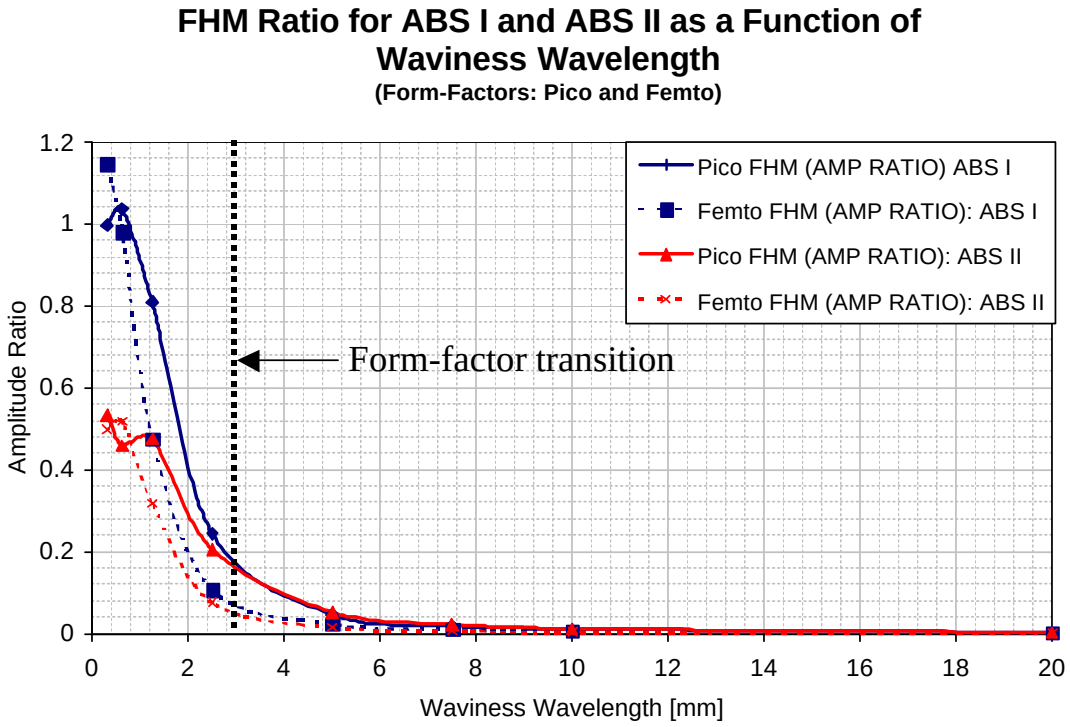

Fig. 4.7. FHM ratio or gain for the ABS I and ABS II ABS's as a function of disk waviness wavelength.

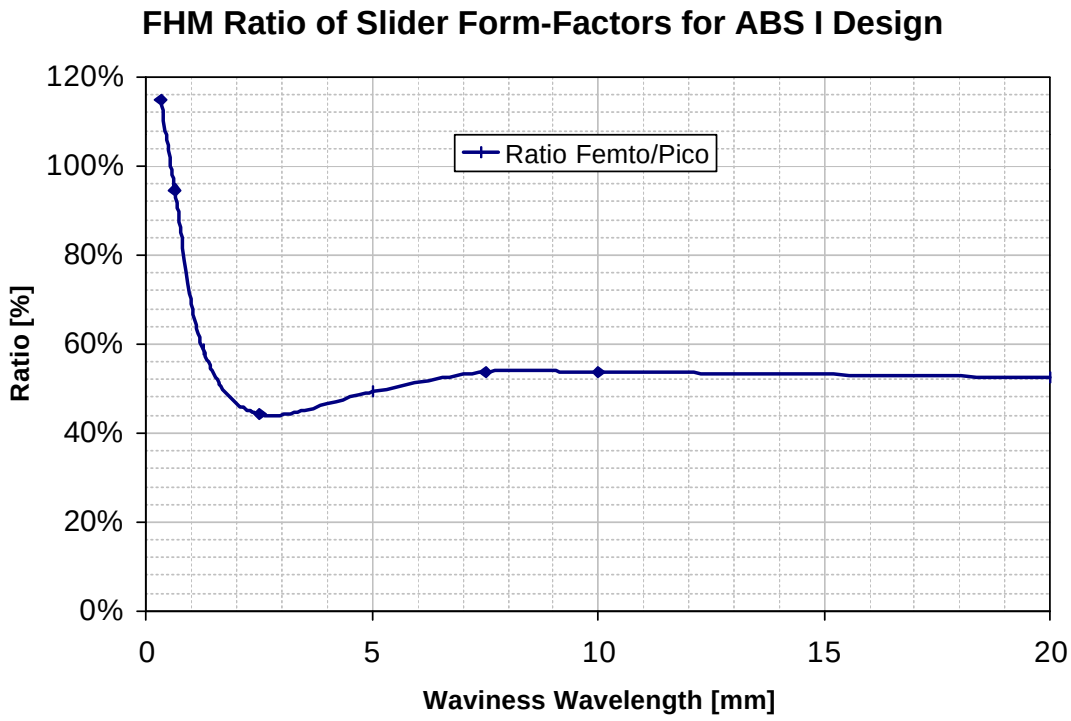

Fig. 4.8. The ratio of FHM ratios of the slider form-factors for the ABS I designs.

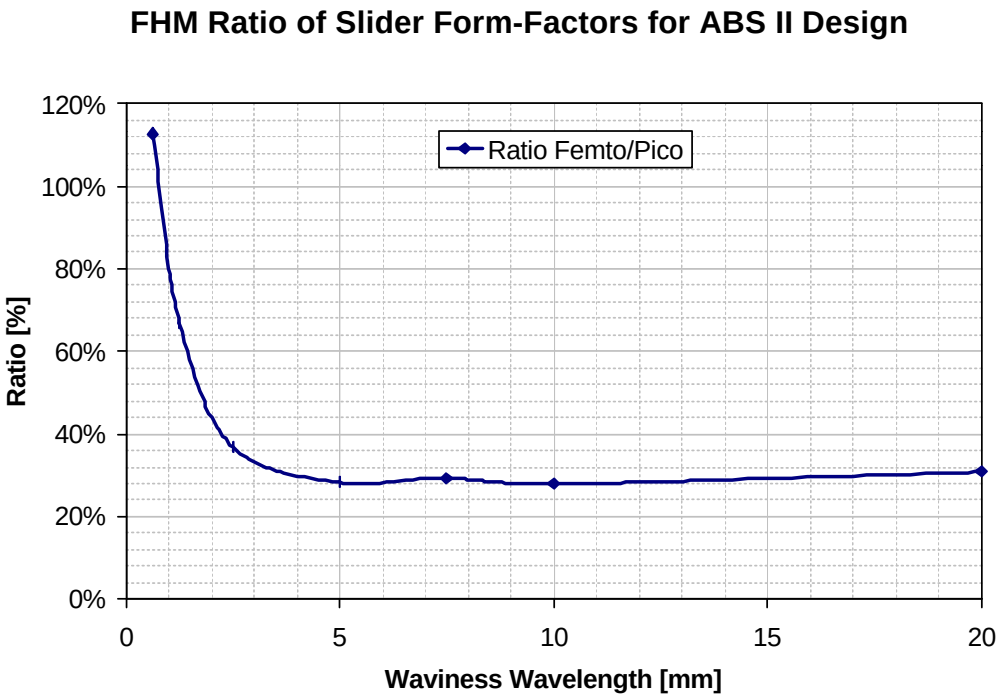

Fig. 4.9. The ratio of FHM ratios of the slider form-factors for the ABS II designs.

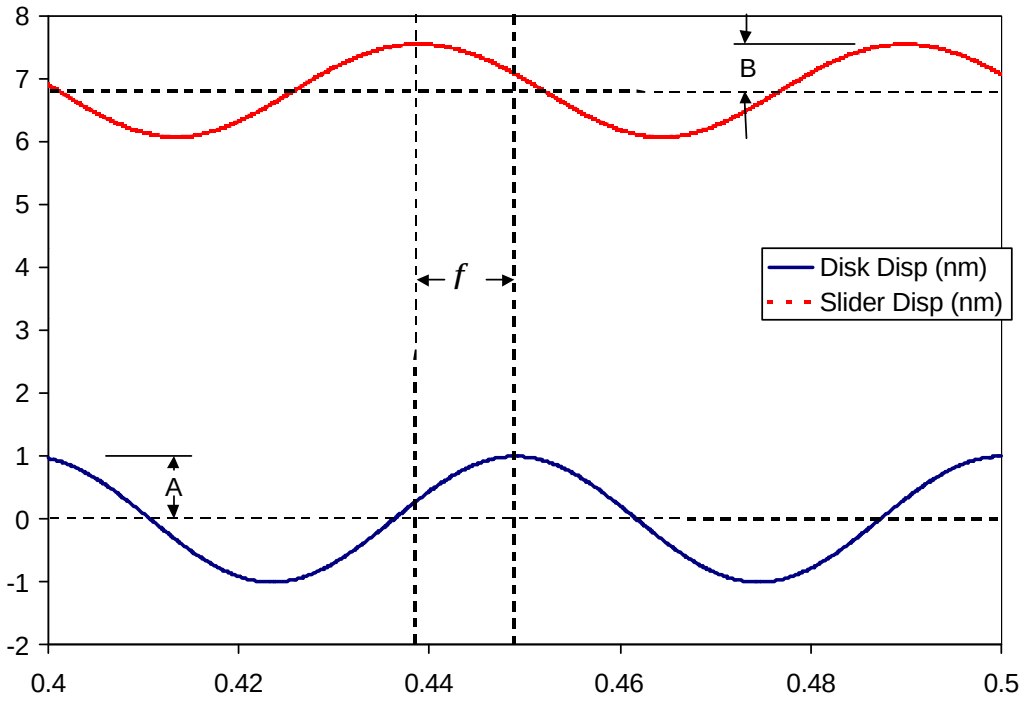

Fig. 4.10. Disk and slider displacement for ABS I in the pico form-factor for a disk waviness wavelength of 0.625 mm.

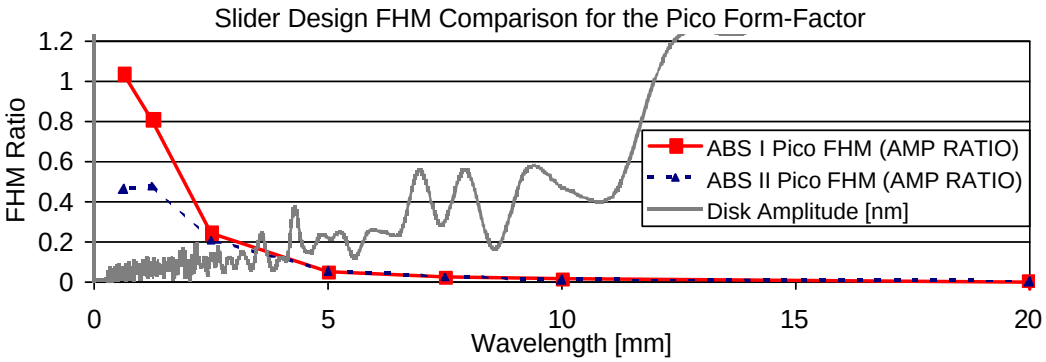

Fig. 4.11. Slider design comparison of the FHM ratios for the pico form-factor with a measured disk topography overlaid.

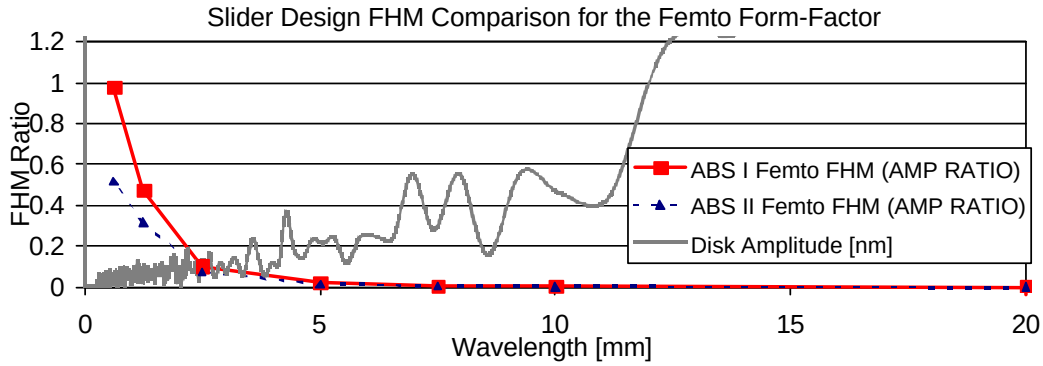

Fig. 4.12. Slider design comparison of the FHM ratios for the femto form-factor with a measured disk topography overlaid.

CHAPTER 5

NON-LINEAR ASPECTS OF AIR BEARING MODELING AND DYNAMIC SPACING MODULATION IN SUB 5 NM AIR BEARINGS FOR HARD DISK DRIVES

Abstract

A new analytical model and method of analysis are proposed for understanding the dynamical behavior of ultra-low flying height air bearing sliders in proximity based on non-linear dynamics. It was found that for sub-5 nm flying height air bearing sliders, the non-linear effects cannot be neglected. These non-linear effects cause a slider's response to become highly non-stationary; making frequency domain analysis by fast Fourier transforms (FFT) an insufficient means of analysis. Joint time-frequency analysis was applied for accurately analyzing the non-stationary slider responses and to verify the non-linear nature of the air bearing for both experimental and simulation results. One degree-of-freedom (DOF) and 2DOF non-linear lumped parameter models were proposed showing the effect of non-linearities on the FFT representations of air bearing slider responses. The 2DOF model was used to further investigate the non-linear coupling effect, and it showed high correlation with experimental results from two different slider designs when they operated in unsteady-proximity conditions. These findings suggest that the non-linearities of the air bearing slider must be considered when modeling slider-disk interface dynamics. Also, complex frequency domain representations of slider responses in proximity can be explained by the non-linear nature of the air bearing slider without contact between the slider and disk contrary to what has been previously proposed by other models.

5.1 Introduction

With areal recording densities increasing in hard disk drives, the physical spacing between the transducer housed on an air bearing slider and the disk media will have to decrease and will require a spacing of 3.5 nm for recording densities of 1 Tb/in^2 [7]. In order to achieve a reliable interface, both magnetically and tribologically, the interactions between the slider and disk must be controlled. With advanced "super-smooth" disk media, it is possible to obtain flying heights (FHs) of sub-5 nm. As a slider's FH decrease to within the glide-height of the disk, a transition between steady flying (i.e. no contact) on a hydrodynamic air bearing film to intermittent contact is observed. This transition region is of interest because the steady-state FH in the sub-5 nm range is near or within this regime and many new phenomena have been observed in these systems.

The air bearing slider system dynamics can be modeled as a three degree-of-freedom (DOF) system – describing pitch, roll, and vertical motions. The dynamics of the system can be analyzed by simulation or experiment to obtain linearized mode shapes, modal frequencies, and damping ratios [17], [21]. The air bearing slider system is by no means linear. However, linear approaches such as linear modal analysis are accurate for steady flying conditions or small perturbations about the steady-state. If the slider is dynamically excited, the response should be a linear combination of the three vibrational modes, and the frequency domain analysis should reveal three or less resonance peaks. However, as the FH decreases, the slider's dynamic response is observed to become more complex in the frequency domain. Harrision *et al.* attributed air bearing harmonics to wave truncation

due to contact, and Knigge *et al.* attributed air bearing harmonics to a non-linear model due to contact with a thickly lubricated disk [22], [23]. However, we have observed even more complex slider responses when flying within "unsteady" proximity without measurable contact.

A new analytical model and method of analysis are proposed for understanding the dynamical behavior of ultra-low FH air bearing sliders in proximity with the disk based on non-linear dynamics. Very few published works have acknowledged the presence or even the effect of air bearing film non-linearities. Knigge *et al.* and Menon *et al.* used joint-time frequency analysis (JTFA) to study the time-frequency evolution of a slider's response to a bump impact [23]-[25]. Sheng *et al.* introduced a non-linear model for the air bearing film and stated that as the slider's response increases in amplitude, the resonance frequency decreases [26]. However, non-linear dynamics is generally more complicated than what is described by their analysis and the idea of a single resonance frequency ceases to exist for non-linear systems.

The modal stiffness of the "vertical" resonance mode (i.e. generally called the second-pitch mode) is found to exponentially increase as the FH decreases. This exponentially increasing stiffness is a predicted result from the generalized Reynolds equation governing the pressure field between the air bearing surface (ABS) and the disk. For sub-5 nm FHs and relatively large perturbations or flying-height modulation (FHM), the air bearing slider's response is no longer stationary in time, and frequency domain analysis using the Fast Fourier transform (FFT) becomes insufficient. JTFA is used here with

experimental and simulation data to show that the slider's response is a non-stationary – frequency modulated response. Simple 1DOF and 2DOF non-linear lumped parameter models are used to reinforce the findings by JTFA, and the effects of slider response amplitude (i.e. the level of non-linearity) and non-linear coupling were studied.

5.2 Preliminaries

5.2.1 Experimental procedure

The experimental data presented are from both sliders A and B shown in Fig. 5.1. The sliders' responses were measured near the pole-tip (PT) location, which is near the trailing edge center (TEC) of the slider body. These measurements were made with a laser Doppler vibrometer (LDV) measuring velocity, which was numerically integrated to obtain displacement. The bandwidth of interest is from 10 kHz to 2 MHz. The test conditions for both experimental and simulation investigations were at the zero-skew radial position.

5.2.2 Experimental results

Figures 5.2a and 5.2b show the frequency domain responses of sliders A and B calculated by FFT analysis averaged 64 times in the frequency domain. Figure 5.2a indicates slider A transitions from steady-proximity to unsteady-proximity as the linear velocity is lowered from 3.8 m/s to 3.6 m/s, and then it further transitions to intermittent contact as the linear velocity is lowered to 3.3 m/s. Figure 5.2b shows a similar transition for slider B. The PT FH for these sliders at the test conditions are within the glide height of the disk – approximately 3-4 nm. Torsion and bending modes of the slider body at 1.25 MHz and

1.6 MHz, respectively, are evidence of contact. Within the region labeled unsteady-proximity, there was no sign of measurable contact. When the sliders fly in steady-proximity, 2-3 air bearing resonance modes are excited at low amplitudes – 112 kHz and 240 kHz for slider A and 167 kHz and 225 kHz for slider B. However, as soon as the sliders transition to unsteady-proximity, many "resonance" peaks appear in the bandwidth of 10 kHz to 1 MHz. The frequency domain response of slider A appears to have a fundamental resonance mode, f_o, at 292 kHz and sub- and super-harmonics at nf_o $(n=1,2,3,\ldots)$ and $(mf_o)/2$ $(m=1,3,5,\ldots)$. Slider B exhibits similar behavior, however, the multiple modes do not show up at simple multiples of a fundamental mode. This region of unsteady-proximity is of interest and is the regime that will be focused upon for the following analysis.

5.3 Air bearing slider dynamics

5.3.1 Governing equations

An air bearing slider's dynamic response is obtained by simultaneously solving the generalized Reynolds equation to attain the pressure distribution over the ABS and the equations of motion describing the rigid body motion of the slider body:

$$\frac{\partial}{\partial x}\left(ph^3 Q \frac{\partial p}{\partial x} \right) + \frac{\partial}{\partial y}\left(ph^3 Q \frac{\partial p}{\partial y} \right) = 6mU \frac{\partial}{\partial x}(ph) + 6mV \frac{\partial}{\partial y}(ph) + 12m \frac{\partial}{\partial t}(ph) \tag{5.1}$$

$$\begin{aligned} m\ddot{z} &= F_s + \int_A (p - p_a) dA \\ I_q \ddot{q} &= M_{sq} + \int_A (p - p_a) \cdot (x_g - x) dA \\ I_f \ddot{f} &= M_{sf} + \int_A (p - p_a) \cdot (y_g - y) dA \end{aligned} \tag{5.2}$$

where p is pressure, h is the local slider-disk spacing, μ is the viscosity of the air, Q is the flow factor, and U and V are the relative velocities in the x and y directions between the slider and disk in Eq. (5.1). In Eq. (5.2), p_a is the ambient pressure, and x_g and y_g are the positions of the slider's center of gravity. F_s, M_{sq}, and M_{sf} are the force and moments applied by the suspension in the z, q, and f directions. I_q and I_f are the slider's moments of inertia and m is the slider's mass. Satisfying these equations simultaneously results in the slider's dynamic response in the vertical (z), pitch (q) and roll (f) DOF's to various inputs. The above equations are based on an assumption of no contact between the slider and disk and are dependent on all the design parameters and flying attitude, and they are highly coupled and non-linear. The CML Dynamic Simulator was developed to numerically solve this set of equations. For small perturbations, the system of equations can be accurately modeled by techniques such as linear modal analysis or perturbation methods [17]. However, when perturbations from steady-state become relatively large, the non-linearities of the equations of motion cannot be ignored.

5.3.2 Non-linear modal coefficients

For simplicity we only address the non-linear nature of the "vertical" mode's stiffness. Although all the modal parameters are non-linear to some degree, the stiffness of the "vertical" mode is the most non-linear one for sub- 5 nm FHs. The "vertical" mode's stiffness was mapped out as a function of FH by adjusting the pre-load value to vary the FH, and then linear modal analysis was preformed with extremely small perturbations to attenuate any non-linear effects. Figure 5.3 is a plot of the stiffness as a function of FH at the PT for the ABS shown in Fig. 5.1a. This slider has a FH of 4 nm at a linear disk

velocity of 3.8 m/s under the simulation conditions. A power law curve fit can be applied to the results giving a stiffness, $k(FH_{PT})$, in units of MN/m as a function of FH at the PT, (FH_{PT}) in units of nm:

$$k(FH_{PT}) = b(FH_{PT})^{a} \tag{5.3}$$

For slider A, the coefficients β and α are determined to be 5.1 and –0.480, respectively. Two important aspects of the non-linear nature of the air bearing film are: (1) as the FH decreases, the stiffness increases exponentially, and (2) the lower the FH, the greater non-linear effects become from small perturbations. By only mapping out the "vertical" stiffness as a function of FH we find that the stiffness is highly non-linear, especially for low FHs.

When large FHM occurs, the "vertical" stiffness of the air bearing slider should change instantaneously according to Fig. 5.3. There no longer exists a single resonance frequency for the "vertical" mode and the larger the amplitude of the slider's response, the more non-stationary the signal becomes, hence the more difficult frequency domain analysis becomes with the FFT.

5.4 Joint-time frequency analysis (JTFA)

In order to accurately represent the frequency content of a signal by FFT analysis, we must assume the signal is stationary or *wide-sense stationary*. The FFT representation, *X(f)*, of a signal, *x(t)*, can be written mathematically as:

$$X(f) = \int_{-\infty}^{+\infty} x(t) e^{-i2\pi ft} dt \tag{5.4}$$

A signal is stationary if it can be written as a discrete sum of sinusoids:

$$x(t) = \sum_{k \in N} A_k \cos[2\pi f_k t + \phi_k] \tag{5.5}$$

According to Fig. 5.3, the slider's response can be approximately represented as a discrete single resonance frequency in Eq. (5.5) and assumed to be *wide-sense stationary* only if: (1) the FH is not below approximately 5 nm, and (2) the perturbations about the steady FH remain relatively small. However, if these conditions are violated, the response of the slider will be highly non-stationary due to the time varying, continuously frequency modulated content of the signal according to Eq. (5.3), and then the response can no longer be accurately represented by FFT analysis.

JTFA has been studied extensively in signal processing to analyze non-stationary signals. More recently it has been introduced in analyzing slider responses to bump impacts [23]-[25]. These studies have acknowledged the presence of a non-linear air bearing effect, however, they explain and represent the non-linear aspects of the air bearing without a physically and theoretically accurate explanation.

A different explanation is adopted here based on the linear reassigned Gabor method [27], [28]. The Gabor representation can be expressed discretely by:

$$G_x[n, m; h] = \sum_k x[k] h^*[k - n] e^{-i2\pi mk} \tag{5.6}$$

where n and m represent the time-frequency plane and h is a Guassian window for localization of the signal in time. This windowing function is defined over an interval of time, and the frequency content is calculated at the center of the window. JTFA can be extremely powerful in representing non-stationary signals, however, its effectiveness is

subject to interpretation. An example of its misrepresentation can be seen in Figs. 5.4 and 5.5. This numerically generated signal is sinusoidally frequency modulated between 0.05 Hz and 0.1 Hz at a period of 51.2 s as seen in the time domain plot in Fig. 5.4a and the time-frequency plot in Fig. 5.4b. Due to the non-stationary nature of this signal, the FFT representation is insufficient in representing the frequency content as seen in Fig. 5.4c. The JTF representations are shown in Fig. 5.5. The differences between these two representations are caused by the different windowing function lengths. The longer the window, the less localized is the captured frequency content. It is seen that one needs a window smaller than the period of the modulated signal in order to accurately represent the frequency content of the signal by JTFA.

The JTF representations of the responses of sliders A and B in unsteady-proximity are shown in Fig. 5.6. It is seen that the responses are non-stationary with frequency content continuously modulated as a function of amplitude or FHM. As the sliders fly lower, the frequency (i.e. stiffness) increases approximately according to the power law shown in Fig. 5.3. Slider B exhibits a slightly more complex signal in both the JTF and FFT representations compared to slider A. The cause of the multiple peaks in the FFT analysis is seen to be a product of the misrepresentation of the non-stationary signal. The following two non-linear lumped parameter models are used to further investigate the non-linear effects.

5.5 Non-linear lumped parameter air bearing slider models

5.5.1 1DOF model

A 1DOF model of the air bearing slider is inaccurate for modeling air bearing slider dynamics. However, it can be useful to provide a basic understanding of the non-linear effects. A schematic of the system is shown in Fig. 5.7, and the equation of motion for unforced free vibration can be written as:

$$m\ddot{z} + c\dot{z} + k(z)z = 0 \tag{5.7}$$

where c is the damping constant, z is the FH with a zero mean (z = FH – steady state FH), and $k(z)$ is given by Eq. (5.3). The CML Dynamic Simulator can be constrained to a 1DOF system by increasing I_q and I_f to prohibit the slider's pitch and roll. Both the 1DOF model and the constrained CML Simulator were then used to simulate an impulse response of the slider in the vertical direction with a large initial perturbation chosen to provide a minimum FH of approximately 1 nm. The FFT was then taken of the response, and it is shown in Fig. 5.8 with the frequency axis normalized to the linearized resonance frequency, f_o. A non-symmetric fundamental mode appears near f_o, and higher harmonics also result from the non-linear stiffness. High correlation is found between the 1DOF model and the constrained CML Simulator simulations. Figure 5.9 shows the effect of the initial amplitude on the FFT representation of the 1DOF model. For a small initial perturbation (0.01 nm), the system behaves linearly showing a single resonance peak. As the initial amplitude is increased, it becomes progressively more difficult to interpret the FFT representation. JTFA can be used to show that this complexity is simply due to a modulated frequency response of the slider. Figures 5.10a and 5.10b show the response

and JTF representations due to a large impulse as simulated by the 1DOF model. Figure 5.10a uses a relatively long window length, *h*, while Fig. 5.10b has a relatively short window length. Figure 5.10b accurately represents the frequency content of the signal while Fig. 5.10a does not. Figure 5.10a is similar to what has been seen by others [23], [26]. Initially, the response amplitude is large and the JTF plot reveals a lower fundamental frequency and harmonics. As the response amplitude decays, the harmonics disappear the fundamental frequency increases to the linear system's resonance frequency. This apparent decrease in the fundamental frequency is an artifact of averaging the non-stationary signal over too long a time period by FFT analysis. This can be seen in Fig. 5.11, which presents the FFT of the response of the undamped 1DOF as the response amplitude increases. Another observation from Fig. 5.11 is the widening of the fundamental peak as the amplitude increases, leading to an interpretation that greater damping is obtained for larger response amplitudes. However, this is again an artifact, or misrepresentation obtained by viewing the non-stationary signal with an FFT.

This 1DOF model and the constrained CML Simulator show complexities of the slider's response when viewed by the FFT are due to the non-linear nature of the air bearing, and they can be explained by only considering the "vertical" mode's non-linear stiffness. However, this model does not explain the sub- and super-harmonics seen experimentally at $mf_o/2$ (m=1,3,5,…) with slider A and the additional peaks with slider B.

5.5.2 2DOF model

A 1DOF model over simplifies the dynamics of the air bearing slider system at the PT location. If we assume that the ABS designs are symmetric and the test condition is at 0^o skew, the roll nodal line will pass extremely close to the PT location, and therefore the roll mode will not contribute to the response. However, there will then be two pitch modes, both of which will contribute to the slider's response at the PT location. This can be modeled by a 2DOF model as shown in Fig. 5.12. The equations of motion of this model for unforced free vibration can be written as:

$$m\ddot{z} + z\cdot\left[k_1(z,\theta)+k_2\right]+\dot{z}\cdot\left[c_1+c_2\right]-l\theta\cdot\left[k_1(z,\theta)-k_2\right]-l\dot{\theta}\cdot\left[c_1-c_2\right]=0$$

$$I_\theta\ddot{\theta} - lz\cdot\left[k_1(z,\theta)-k_2\right]-l\dot{z}\cdot\left[c_1-c_2\right]+l^2\theta\cdot\left[k_1(z,\theta)+k_2\right]+l^2\dot{\theta}\cdot\left[c_1+c_2\right]=0 \qquad (5.8)$$

where $k_1(z,\theta)$ and c_1 are the stiffness and damping coefficients at the TE of the slider body. Similarly, k_2 and c_2 are the stiffness and damping coefficients at the leading edge (LE) of the slider body. The only non-linear element of this system is the TE spring, characterized by $k_1(z,\theta)$, which is a function of both z and θ:

$$k_1(z,\theta)=\beta\cdot(z-l\cdot\theta)^\alpha \qquad (5.9)$$

Since the PT response will be a combination of both pitch modes, which contain the non-linear spring, both modes will be non-linear and coupled. The stiffness values, k_2 and the linearized value of k_1 were selected so as to obtain the same linearized modal frequencies of the first and second pitch modes as seen in slider A. The ratio of the linearized second pitch mode resonance frequency (f_2) to the linearized first pitch mode resonance frequency (f_1) is defined by $R=f_2/f_1$. For this particular ABS design, $R \approx 2.2$. The damping coefficients were chosen to fit the CML Simulator data. This 2DOF model can be compared to the CML Simulator by looking at an impulse response of the slider. Here,

the CML Simulator is no longer constrained as in the previous section. The results are shown in Fig. 5.13 in both the time and frequency (FFT) domains. The frequency axis is normalized by f_2, which is defined to be the fundamental frequency, $f_o = f_2$. There is a high correlation between the 2DOF model and the CML Simulator. These results show a complicated slider response representation by the FFT. This 2DOF exhibits all the sub- and super-harmonics at nf_o $(n=1,2,3,\ldots)$ and at $(mf_o)/2$ $(m=1,3,5,\ldots)$ as seen experimentally for slider A. The FFT also exhibits a split peak around f_1 due to the non-linear coupling between the two modes. Figure 5.14 shows the amplitude effect on both the impulse response and the undamped response. As the amplitude increases the degree of non-linearity increases, causing the FFT representation to become less representative of the system's response.

Also, the resonance frequency ratio, R, has a drastic effect on the slider's response as represented by FFT analysis. Figure 5.15 shows impulse responses for several values of R varying from 1.7 to 3. In most cases the FFT exhibits several peaks extending high above the fundamental frequency, f_o and, in some cases, below f_1. Figures 5.16a and 5.16b show the JTF representations of the responses for R equal to 2.4 and 1.7, respectively. Here it is clearly seen that the frequency signature in the JTF representation changes drastically by varying R. The response of slider A is closely represented by the results shown in Fig. 5.16a with $R \approx 2.2$ and the response of slider B closely resembles the results shown in Fig. 5.16b with $R \approx 1.35$ as can be seen by comparing these figures to Figs. 5.6a and 5.6b.

5.6 Discussion

When air bearing sliders transition between steady flying to intermittent contact, an unsteady-proximity regime exists where complexities of the slider's response are seen in the frequency domain. In this regime, the non-linearities of the air bearing slider system, according to the generalized Reynolds equation, are not negligible. In fact, the "vertical" resonance mode of an air bearing exponentially increases as FH decreases. This non-linearity causes the slider's response to be non-stationary in time and the larger the perturbations are from steady-state flying and the lower the FH, the more pronounced this effect becomes. FFT analysis is a satisfactory means for analyzing the frequency content of stationary or *wide-sense stationary* signals, however it becomes increasingly more difficult to interpret FFT results the more non-stationary the signal becomes.

Linear reassigned Gabor JTFA was used to represent the sliders' responses obtained from both experimental and simulation results. JTFA was used to show that the sliders' responses were non-stationary and demonstrated that the complexity seen by FFT analysis was due to non-linearities.

1DOF and 2DOF non-linear lumped parameter models were introduced to further study the effects of the non-linearities. The 1DOF model was verified by comparing the response to a constrained model simulated by the CML Simulator. This model only simulated the vertical motions of the air bearing slider while constraining the pitch and roll motions. These models were used to show that super-harmonics of the fundamental

linearized resonance frequency were caused by the non-linear stiffening of the air bearing slider system. Also, the level of non-linearity was studied to understand the evolution of a linear to a highly non-linear system and the associated complexities with FFT analysis. This 1DOF model gave a basic understanding of the non-linear effect; however, it was inadequate for completely explaining the experimental results.

A 2DOF model was introduced to more accurately model a slider's response, and it was verified with the CML Simulator. The results show that both pitch modes become non-linearly coupled, causing extreme complexities by FFT analysis. This model explained the sub- and super-harmonics seen experimentally for slider A. Similar to the 1DOF model, the level of non-linearity was again studied to observe the evolution of a linear to a highly non-linear system and the associated complexities with FFT analysis. By changing the linearized modal parameters, specifically the resonance frequency ratio, R, we observed drastic differences in the slider's FFT frequency content. For some values of R the non-linear response did not resemble the linear response by FFT analysis but showed results similar to those of the experimental response for slider B.

5.7 Conclusion

These findings suggest that the non-linearities of the air bearing slider system cannot be ignored for sub-5 nm FH sliders and must be considered when modeling slider-disk interface dynamics. When a slider is within proximity of a disk the complexities of the slider's response can be explained by the non-stationary response, and FFT analysis becomes an inadequate means for frequency domain analysis. A method such as JTFA

must be used to accurately analyze the non-linear, non-stationary response of a slider when it is in the state of unsteady-proximity. Contact between the slider and disk can cause complexities of the slider's response due to the additional boundary conditions when viewed in the frequency domain, however, it is seen that contact is not a necessary condition for producing this phenomenon.

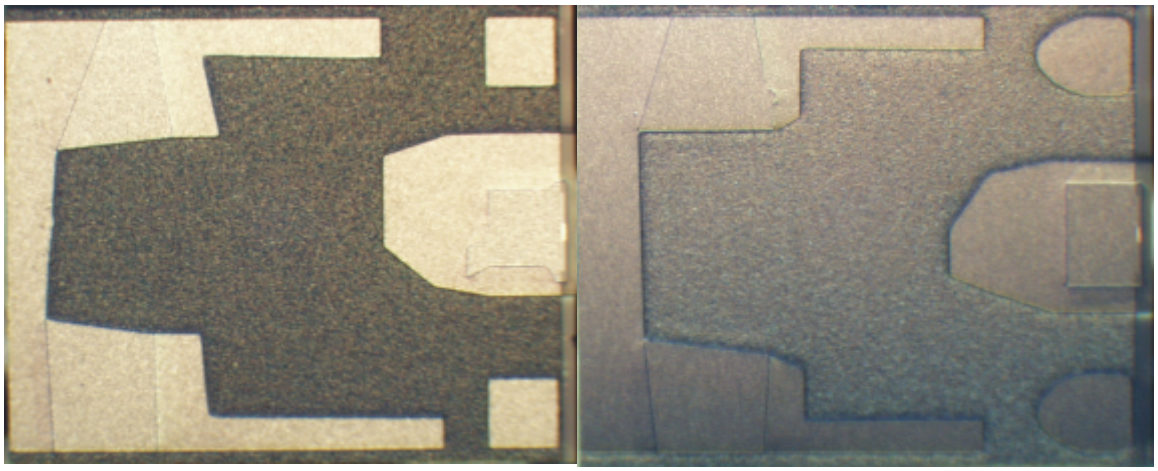

(a) (b)

Fig. 5.1. ABS pictures of (a) slider A and (b) slider B.

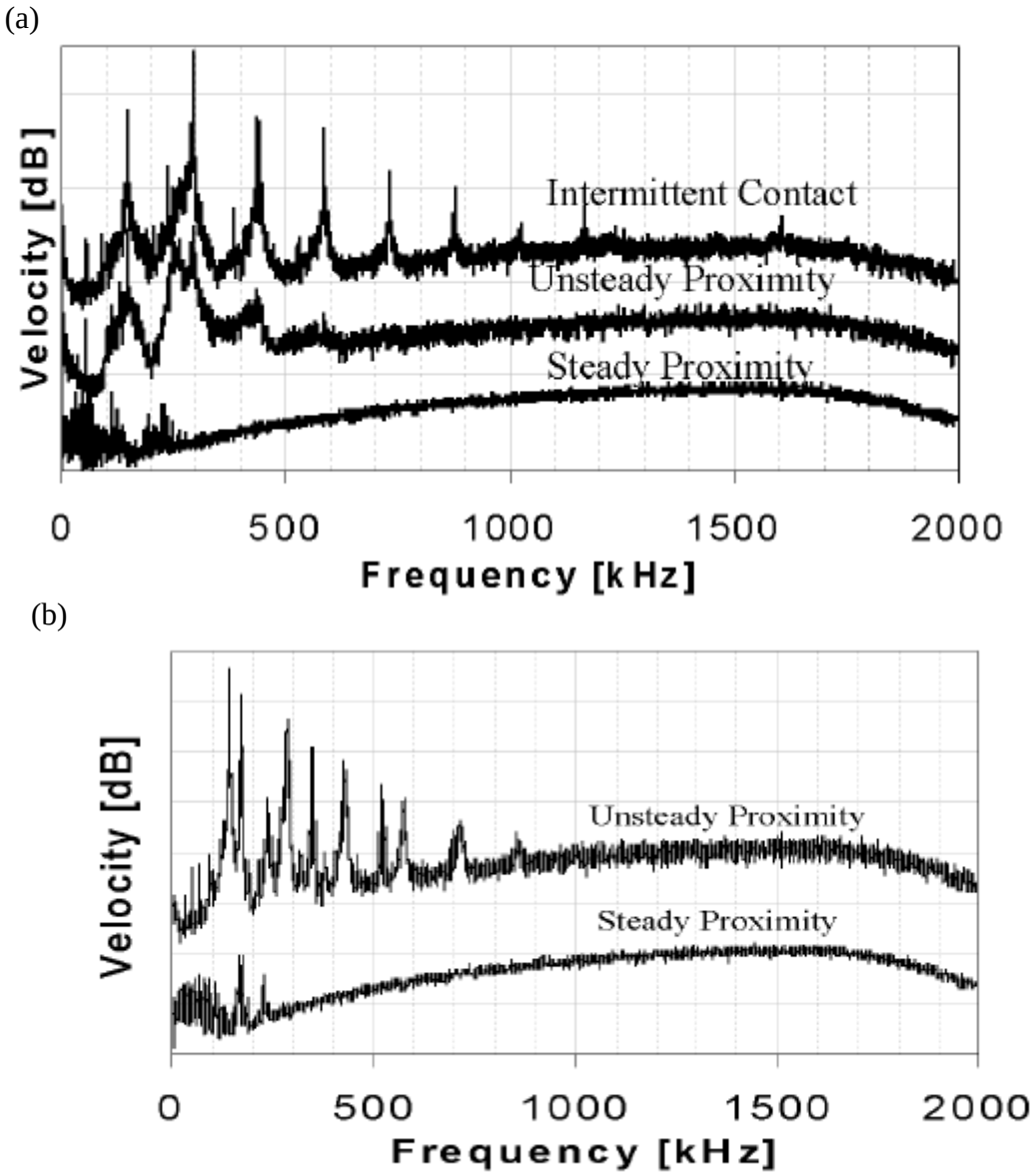

Fig. 5.2. Frequency domain averaged slider velocity response for (a) slider A and (b) slider B transitioning from steady proximity to unsteady proximity and intermittent contact.

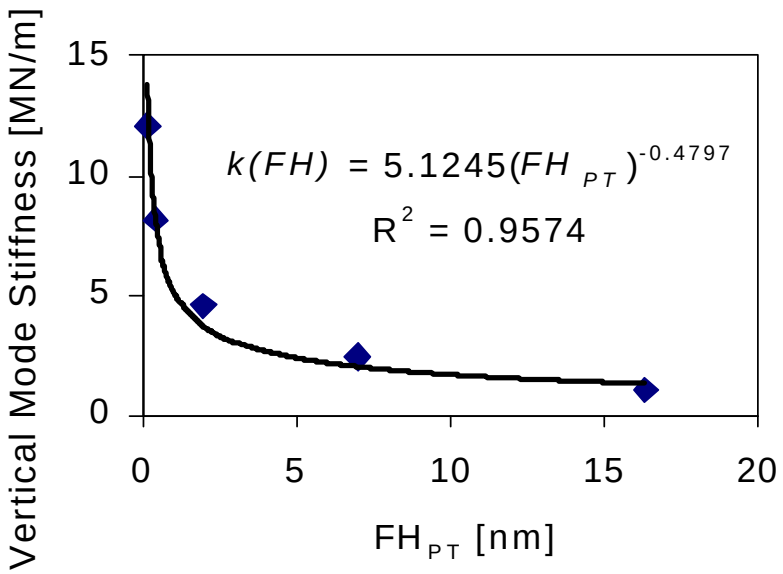

Fig. 5.3. Non-linear “vertical” air bearing stiffness as a function of FH at the PT.

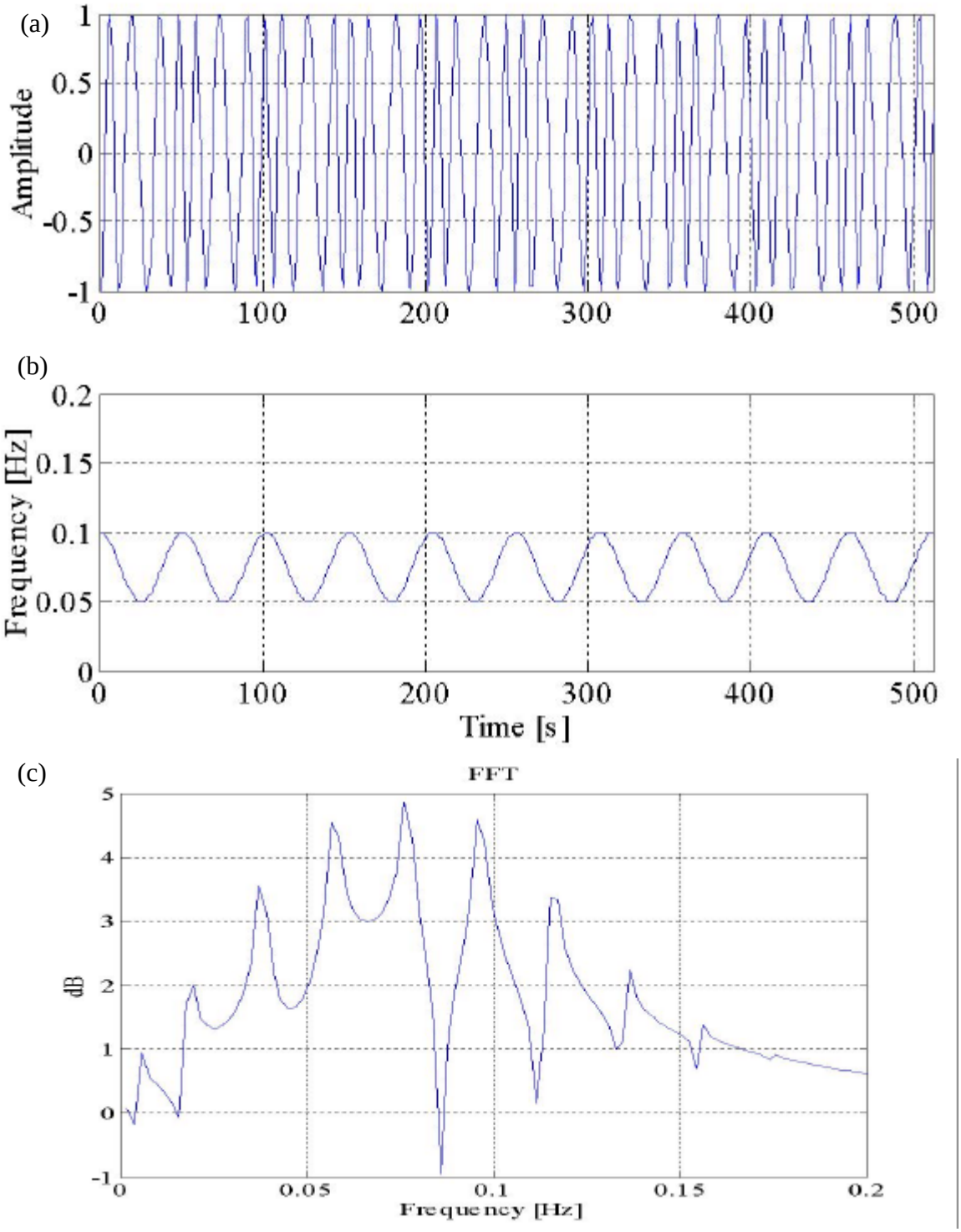

Fig. 5.4. Numerically generated sinusoidally frequency modulated signal shown in the (a) time-amplitude, (b) time-frequency, and the (c) frequency (FFT) domains.

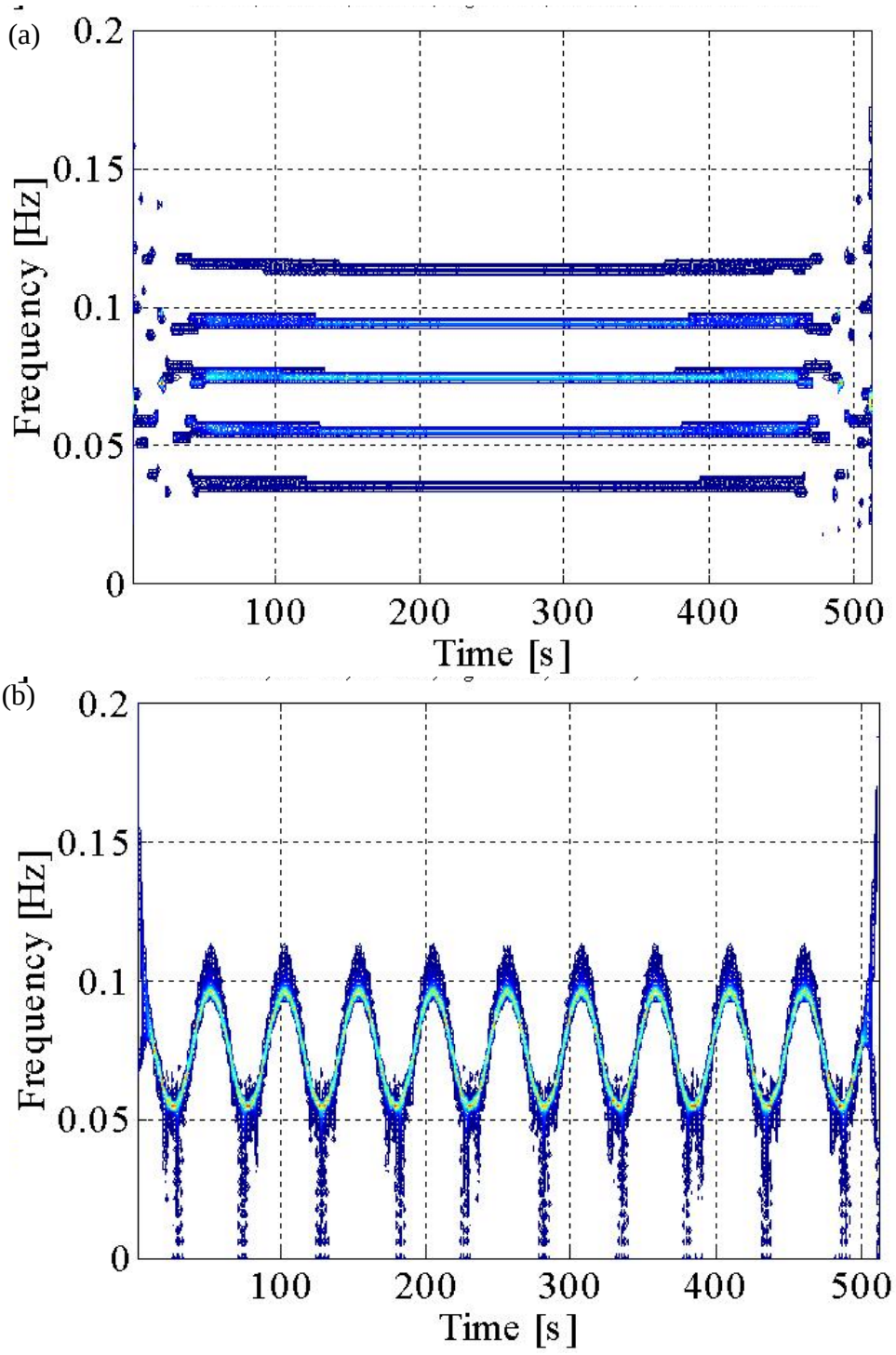

Fig. 5.5. JTF representations of the numerically generated sinusoidally frequency modulated signal with (a) a relatively long and (b) a relatively short windowing function.

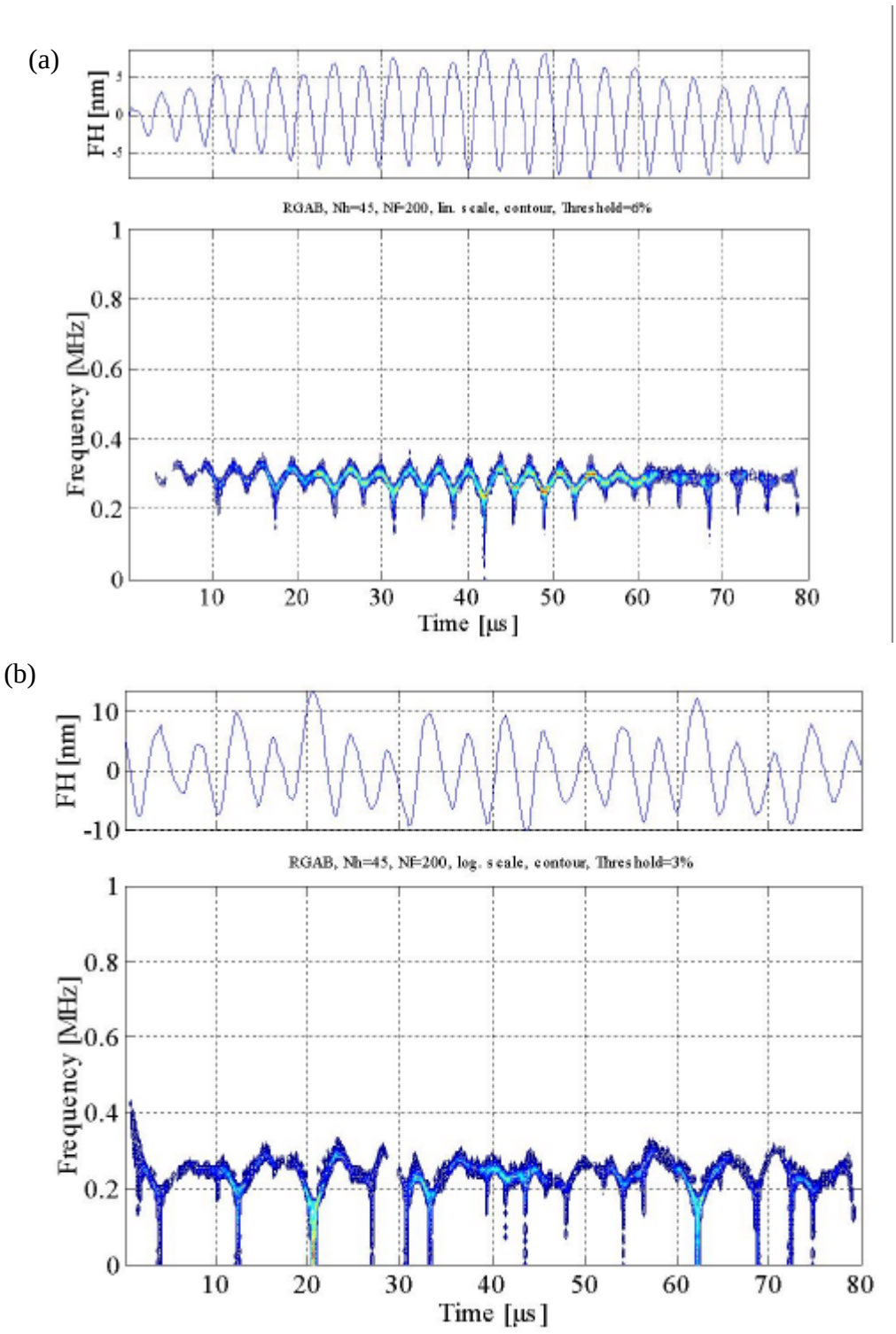

Fig. 5.6. JTF representations of (a) slider A and (b) slider B in unsteady proximity experimentally measured.

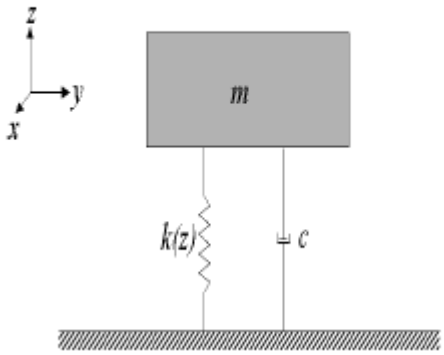

Fig. 5.7. 1DOF model schematic.

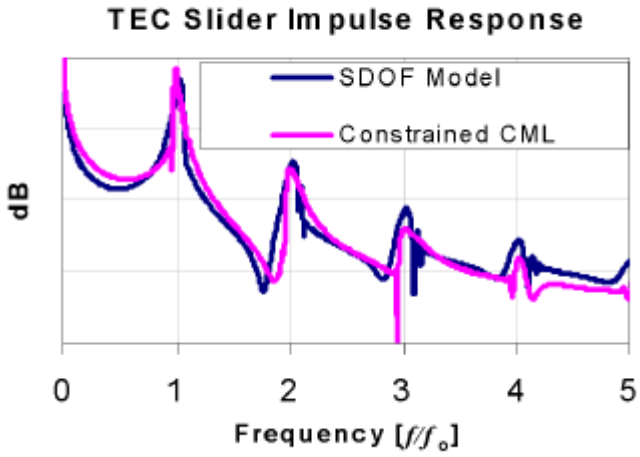

Fig. 5.8. The FFT's of slider A's impulse response simulated by the SDOF model and the constrained CML Simulator.

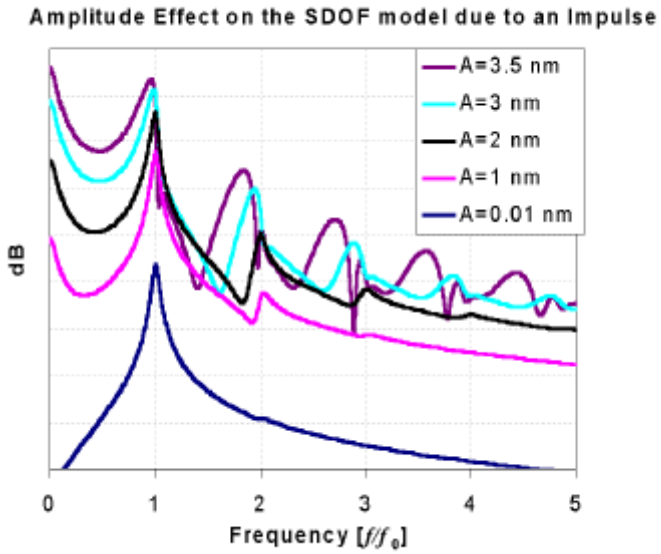

Fig. 5.9. The effect of amplitude (i.e. effect of the level of non-linearity) on the FFT representation of an impulse response simulated by the 1DOF model.

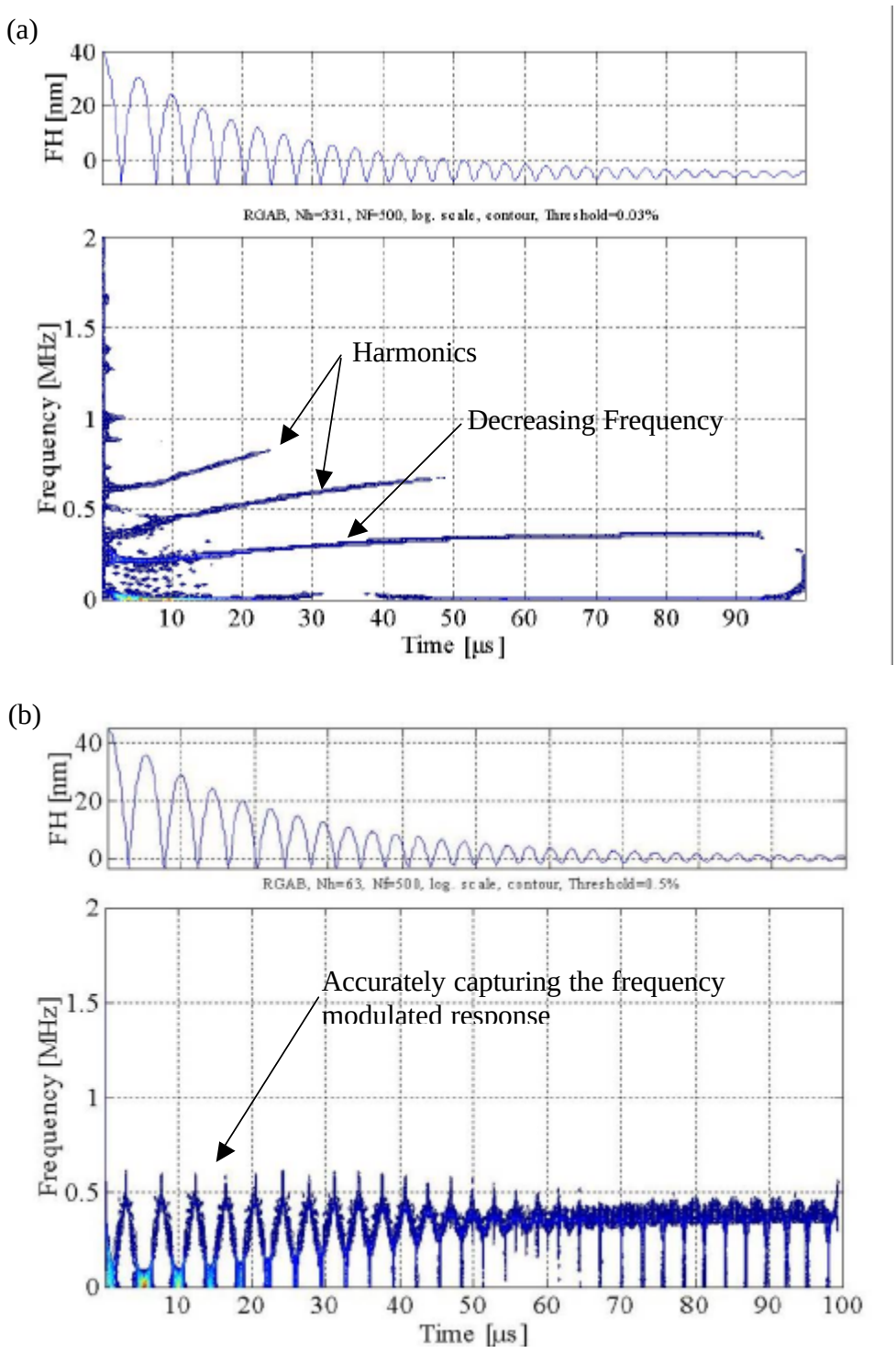

Fig. 5.10. JTF representations of a large impulse response simulated by the 1DOF model with (a) a relatively long windowing function and (b) with a relatively short windowing function.

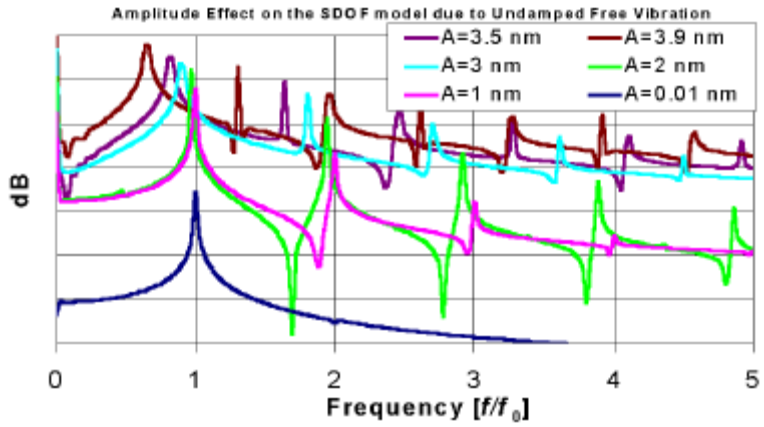

Fig. 5.11. Effect of amplitude (i.e. level of non-linearity) on the FFT representation of the undamped response of 1DOF model.

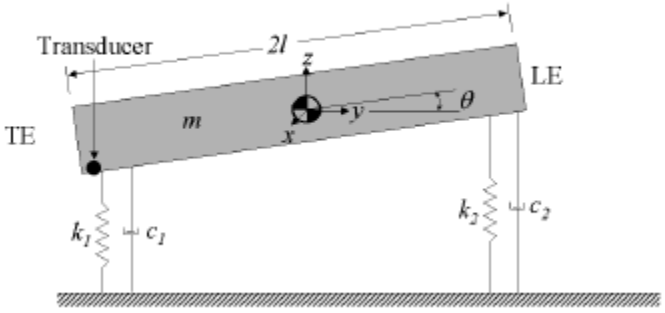

Fig. 5.12. 2DOF model schematic.

(a)

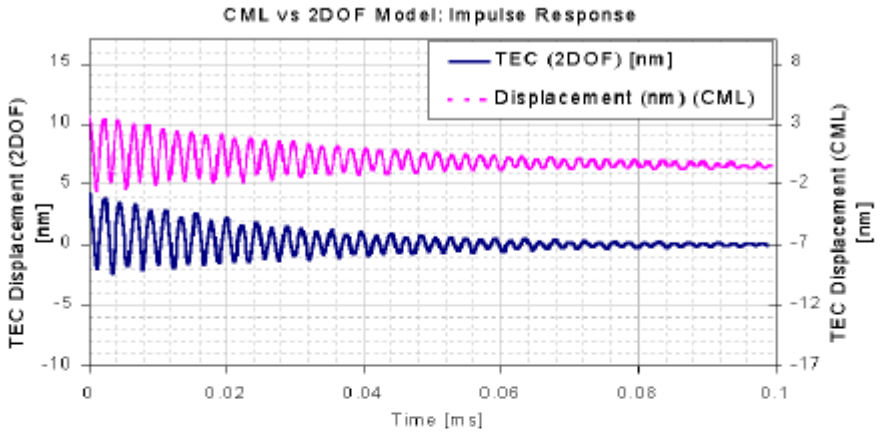

(b)

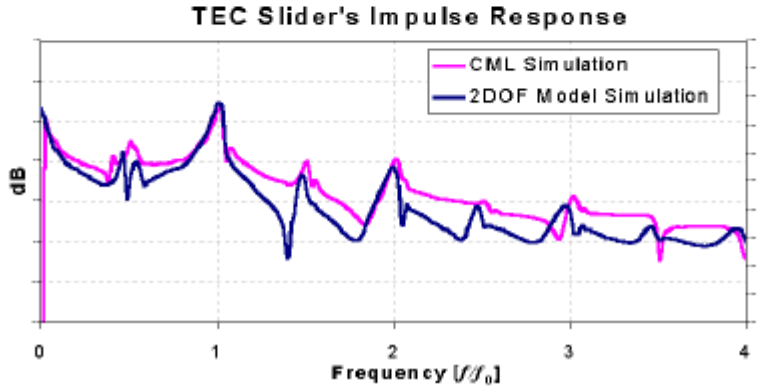

Fig. 5.13. Impulse response of slider A simulated by the 2DOF model and the CML Simulator shown in the (a) time and (b) frequency (FFT) domains.

(a)

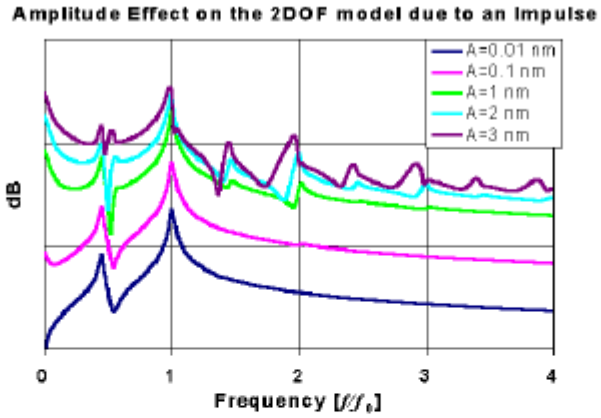

(b)

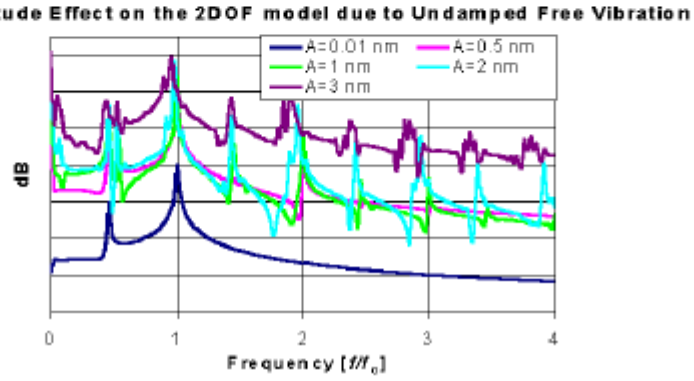

Fig. 5.14. Effect of amplitude (i.e. level of non-linearity) on the FFT representation of an (a) impulse and (b) undamped responses of the 2DOF model.

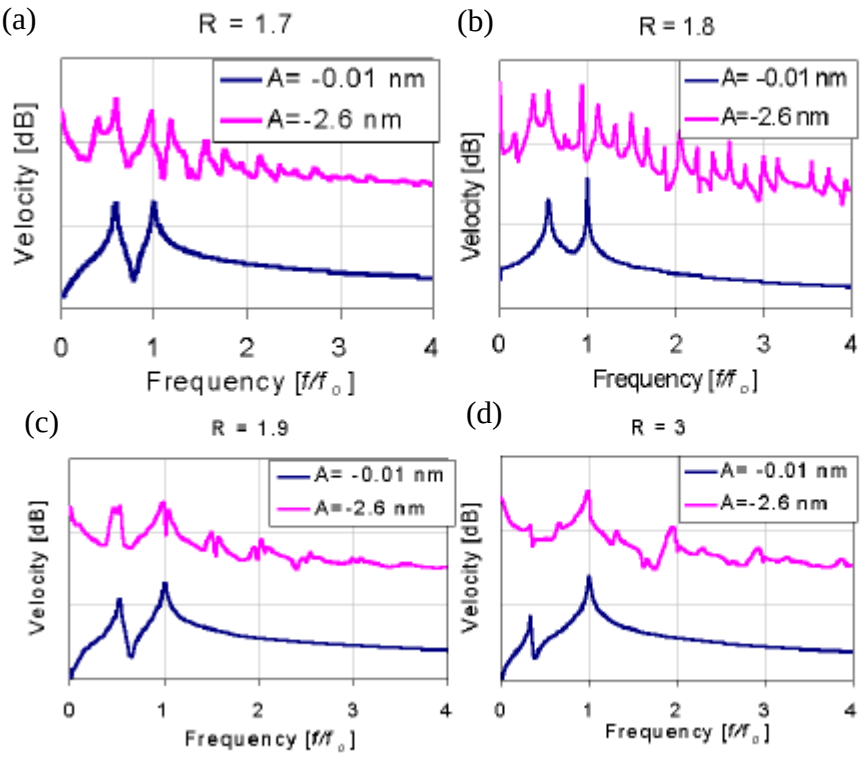

Fig. 5.15. The effect of non-linear coupling the FFT domain by varying *R*: (a) *R*=1.7, (b) *R*=1.8, (c) *R*=1.9, and (d) *R*=3.

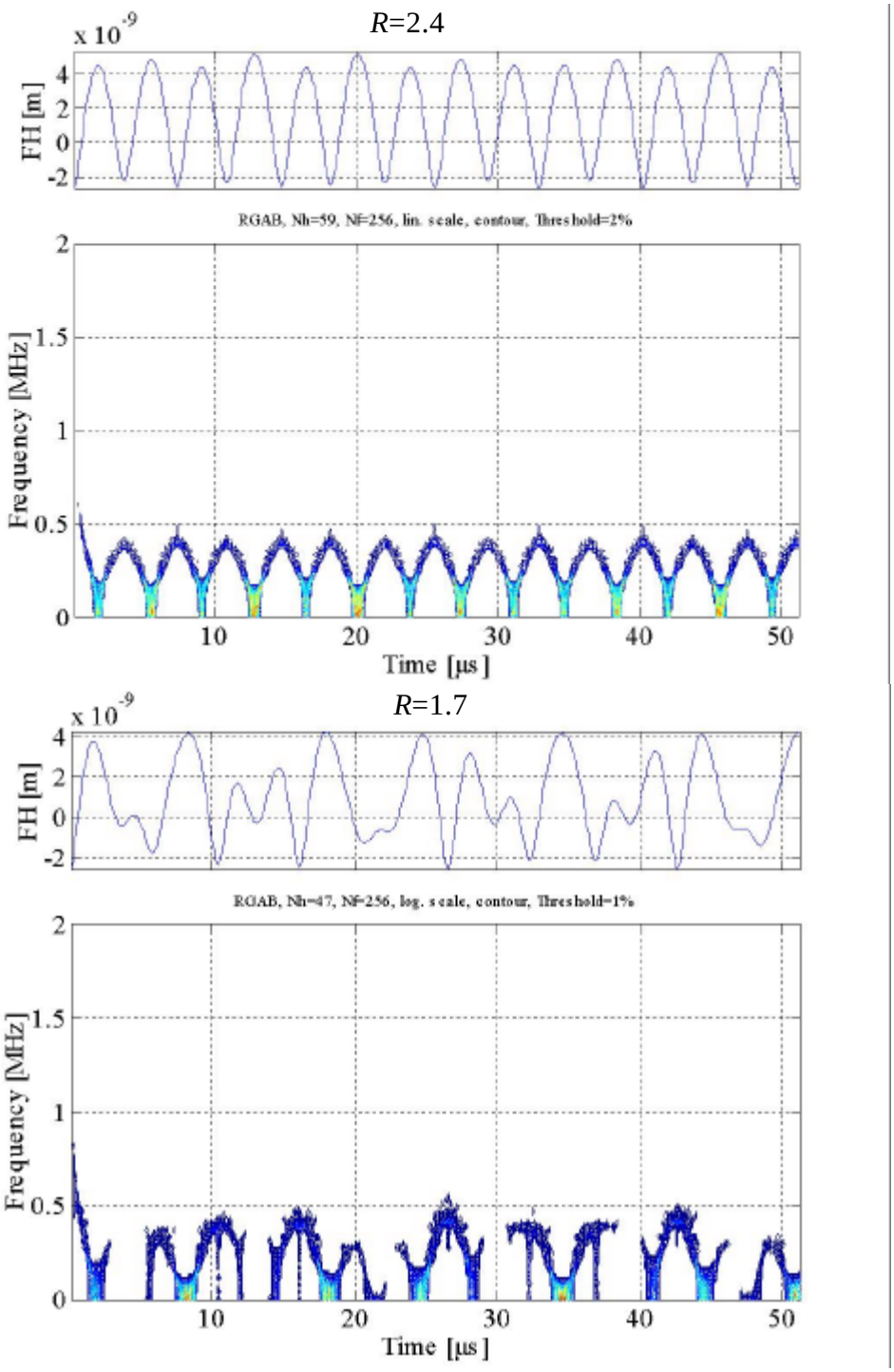

Fig. 5.16. JTF representations of the 2DOF model with (a) R=2.4 and (b) R=1.7.

CHAPTER 6

HEAD-DISK INTERFACE DYNAMIC INSTABILITY DUE TO INTERMOLECULAR FORCES

Abstract

This chapter presents a nonlinear dynamic analysis of the head-disk interface by including intermolecular adhesion forces for sub- 5 nm flying air bearing sliders. Experimental evidence shows that one of the major roadblocks in achieving ultra-low flying-heights is the stability of the head-disk interface. It is found that the inclusion of intermolecular forces between the slider and disk in modeling the head-disk interface leads to dynamic instability of the slider. It is shown by a bifurcation diagram that a slider can easily be forced into unstable, high amplitude oscillations. It is also shown that the experimentally observed spin-down – spin-up flying-height hysteresis, intermittent flying instability, and "snapping" from stable to unstable proximity can be explained by the inclusion of the intermolecular forces. A parametric study is conducted showing the dependence of stability/instability on the variables. By understanding the effect each parameter has on stability, we can achieve air bearing surface and disk morphology system design guidelines. From this study it is found that the head-disk interface can become unstable due to intermolecular forces below a flying-height of about 6 nm. However, from the results of the parametric study, it is shown that a head-disk interface can be designed such that it maximizes stability, although the instability cannot be attenuated completely. By minimizing the intermolecular adhesion forces and the flying-height modulation, and by maximizing the air bearing stiffness and damping, we achieve

maximum stability. Also, it is found that the stiffening effect of the air bearing film increases the stability. The implications of this study are that the head-disk interface stability is dramatically compromised in the sub- 6 nm flying-height regime and that the glide-height of "super-smooth" disks will not only be a function of the disk's morphology but also the intermolecular adhesion force induced instability of the slider.

6.1 Introduction

In order to achieve a magnetic recording areal density of 1 Tbit/in^2 it is expected that the physical spacing between the media and transducer or flying-height (FH) will have to be 3.5 nm [7]. For a head-disk interface (HDI) to perform reliably, both tribologically and magnetically, the fluctuations in the FH must be held to a minimum. One of the roadblocks thus far for realizing a 3.5 nm FH is the dynamic stability of the HDI. We showed experimentally in Chapter 5 that a slider can transition from stable to unstable proximity flying by decreasing the FH only slightly. Also, it has been widely observed that a slider's touchdown and takeoff FH's are not equal. This "snapping" effect between stability and instability and the difference in a slider's touchdown and takeoff FH's are evidence of a complicated dynamical system when operating in the sub- 6 nm FH regime. As the slider to disk spacing is decreased, the interface surface interactions are evidently no longer negligible. Two adhesion models have been proposed to account for the interactions between the slider and the disk: one is based on lubricant interacting with the slider causing a meniscus force and the other is based on intermolecular forces between the two intimate surfaces.

Previous publications have studied the effects of lubricant on HDI stability and flying characteristics [30] - [33]. Kato *et. al.* used an equilibrium meniscus force model in simulations to account for the dynamic slider-lubricant interactions [31] - [33]. However, their use of this meniscus force model neglects some very important assumptions of the model: extremely thin liquid lubricant film thickness ($\approx$ 15 Å) and the kinetic formation of a meniscus. Generally, lubricant is highly bonded to the disk surface, thus only a fraction of the lubricant layer is available to behave as a liquid in the formation of a meniscus making a meniscus more energetically difficult to form. Also, on the time scale of interest for "bouncing" or unstable proximity of the air bearing slider, the liquid volume required to form the meniscus does not have time to be transported and is far from the equilibrium state described by a kinetic meniscus formation model [34].

Intermolecular adhesion forces can be extremely large when two very flat surfaces come within proximity. In fact, it has been shown that intermolecular adhesion forces are the mechanism that allows gecko lizards to "stick" on molecularly smooth surfaces [35]. Therefore, when flying an extremely smooth air bearing slider over a "super-smooth" disk at ultra-low FH's, intermolecular forces must be accounted for. Thus far, publications investigating the effect of intermolecular forces on the HDI have been based on static analysis [36] - [38]. It has been shown that for air bearing sliders flying in the sub- 5 nm regime, intermolecular forces can become important and cause a significant decrease in static FH [36]. However, the implications of intermolecular forces on the dynamic stability of the HDI have not been published.

In this chapter we present some experimental evidence of the abrupt stable to unstable flying transition and the FH hysteresis, which are measures of instability for the HDI. We also show that even for non-lubricated disks HDI instability occurs, suggesting this phenomenon is more likely to be caused by intermolecular forces than by meniscus forces. By accounting for the intermolecular forces through a Lennard-Jones potential and representing the HDI by a lumped parameter one degree-of-freedom (1DOF) model, we show that the system becomes highly nonlinear in the proximity region. It is shown that the dynamics of this nonlinear system are extremely complicated and can even be chaotically unstable. From a nonlinear dynamics analysis with nominal values and from a parametric study, the variables implicating the HDI stability/instability are discussed, including design guidelines to minimize HDI instability due to intermolecular forces.

6.2 Experimental results

It has been observed that when the FH of a slider is gradually reduced to within proximity of an extremely "super-smooth" disk the slider can be easily set into unstable high amplitude oscillations. Figure 6.1a shows the absolute displacement of the trailing edge center of slider 2 shown in Fig. 6.2 flying in proximity of the disk at linear velocities of 3.6, 3.4 and 3.2 m/s. This result is measured by a laser Doppler vibrometer (LDV) in the bandwidth of 10kHz – 2 MHz. It is seen that the slider transitions abruptly from stable to intermittently unstable and then further to indefinitely unstable as the velocity is lowered slightly. The high amplitude oscillations of the slider appear to be self-excited as opposed to asperity contact induced. This "snapping" effect from stable to unstable suggests complex dynamics of the HDI system.

It has been widely observed that as a slider is forced into and back out of contact by decreasing and increasing disk speed or pressure a FH hysteresis is present (i.e., touchdown FH ≠ takeoff FH) [39]. Experiments investigating HDI instabilities as a function of the FH were conducted on a TTi T1000 spinstand for various sliders and disks while controlling the FH with the spindle speed of the disk. The sliders instability and contact was initially measured by both LDV and an acoustic emission (AE) sensor, however, the LDV was found to be much more sensitive than the AE sensor. Therefore, the sliders vertical motion was measured by a LDV and highpass filtered at 60 kHz to obtain air bearing resonance vibration and slider body vibration modes to detect unsteady proximity and contact, respectively. This signal was then acquired through a RMS circuit sampled at 4 kHz. A typical FH hysteresis can be seen in Fig. 6.1b, which shows the sliders RMS vertical velocity as the disk spindle RPM is lowered until the slider comes into unsteady proximity and/or contact with the disk (touchdown) and then the disk spindle RPM is increased and the slider ceases to contact and flies in steady proximity over the disk (takeoff). It has been observed that the touchdown RPM is lower than the takeoff RPM or the touchdown height (TDH) is less than the takeoff height (TOH). This difference in RPM or FH is what constitutes this hysteresis (TOH - TDH). Several sets of experiments were conducted using four different sub-ambient pressure pico sliders and a set of disks with varying lubricant thickness. The four air bearing surfaces (ABS) are shown in Fig. 6.2. Two types of disks were used in this experiment: B2 with R_a = 0.3 nm and B4 with R_a = 0.2 nm both with glide-heights of 2.5 to 4 nm. The disks were all processed in exactly the same manner with the only variation being the lubricant

thickness: 0 (not lubricated), 8, 12, 16 and 20 Å. The lubricant is a perfluoropolyether (PFPE) with a high bonding ability to the disk of approximately 80%. For every test, new samples were used so as to not affect the experimental results by lubricant pickup on the slider, wear and other factors. Figures 6.3 through 6.6 summarize the experimental results for sliders 1 – 4. The bar graphs show the touchdown, takeoff, and hysteresis RPM's as a function of lubricant thickness. It is interesting to notice that for all of the lubricant thicknesses tested, there is no trend in the FH hysteresis as a function of lubricant thickness. What is common among all the tests is that a FH hysteresis is present for all disks and sliders tested including the non-lubricated disks and that the takeoff RPM was always higher than the touchdown RPM. This FH hysteresis can be used as a measure of instability of the HDI. For example, take the case of slider 3 flying over the disk with 0 Å of lubricant (see Fig. 6.5). If the slider is flying at any speed between 3500 RPM (touchdown) and 8000 RPM (takeoff) the slider has the ability to become unstable and remain unstable until the RPM is increased beyond the 8000 RPM (takeoff). Also, the intensity of the sliders vibration can be measured from the RMS value of the LDV signal. For sliders 1 – 3, the intensity of vibration saturated the data acquisition system. However, slider 4 exhibited very low vibration amplitude, as seen in Fig. 6.7 compared to the other sliders. The main difference between sliders 1 –3 and 4 is the small diamond-like carbon pads distributed across the entire ABS. These small pads on slider 4 decrease the actual proximity/contact area substantially and lead to less adhesion force, which could explain the results seen in Fig. 6.7. Also, the sliders vibration amplitude in Fig. 6.1b is asymmetric, showing that the maximum slider vibration does not occur when the RPM is the lowest.

Both the “snapping” effect from steady to unsteady proximity flying and the presence of a FH hysteresis are new phenomena not well understood. By simulating a quasi-static FH and the touchdown-takeoff process, accounting for all of the forces shown in the free-body diagram in Fig. 6.8, we would not predict this “snapping” effect from stable to unstable proximity or the FH hysteresis. Therefore to explain the above experimental observations, it appears that additional forces at the HDI can no longer be neglected for such low FH’s.

6.3 Adhesion forces at the HDI

With FHs decreasing and the probability of contact increasing, a better understanding of the interface interactions are becoming more important in developing a reliable HDI. Also, with the intimate surfaces of the slider and disk becoming extremely smooth (i.e., close to atomically smooth) and with the presence of a thin layer of lubricant on the disk surface, the interface interactions become very complicated. Generally the interface is a diamond-like carbon (DLC) coated slider surface – the air – a lubricant interface during flying, and a DLC coated slider surface – lubricant surface interface during contact. If the disk is not lubricated, the interface would include the DLC coated disk instead of the lubricant layer. The source and nature of the interface forces acting between the slider and the disk can be very complicated. Such forces can be generated through electrostatic charging, tribocharging, and adhesion. In this chapter we will only consider adhesion forces acting at the interface.

At least two types of adhesion forces can be generated at the HDI: capillary (meniscus) and intermolecular. In order for meniscus forces to be generated, a liquid layer must be present at the interface. In the case of the HDI, the liquid layer would consist of primarily the mobile lubricant and possibly a very thin condensed water vapor layer. Also, the formation of a meniscus force is kinetic, hence, highly time dependent [34]. It has been shown through experiments and simulation that the meniscus force is negligible when the slider and lubricant are in contact over a short enough time period and increases to a steady-state value over a time period on the order of minutes [34], [40]. Under dynamic instability of the slider, it can be seen from Fig. 6.1a that the slider is in contact with the lubricant layer for less than 800 ns; far too short to form a measurable meniscus force as predicted from a kinetic meniscus formation model and previous experimental results. Also, for the high velocity vibration of the slider under unstable proximity, it is still unknown if the lubricant behaves as a liquid or a solid when the slider impacts the lubricant. Our experimental results agree with the above analysis. If meniscus forces were partially the cause of the additional interface forces, then we would expect the FH hysteresis to increase as the lubricant thickness increases, and little or no FH hysteresis should exist for an interface without lubricant. Our experimental results shown in Figs. 6.3 – 6.6, show no clear trend in the FH hysterisis with increasing lubricant thickness and that a FH hysterisis is present even for an interface without lubricant.

Meniscus forces and/or other lubricant interactions could possibly cause new dynamic HDI phenomena; however, the above experimental results showed very little correlation between a meniscus force effect and instability. For the following analysis the

contribution of adhesion due to meniscus formation under the unsteady proximity regime seems unlikely and adhesion due to intermolecular forces, which is time independent for unsteady proximity of the HDI, is considered to be the sole contributor to adhesion. To get an idea of the magnitude of the adhesion force generated by intermolecular forces we focus on a particular system. For a flat area, A_s = 15,000 μm^2 (approximate area of the alumina at the trailing edge of slider 2) placed parallel to a flat disk surface, the van der Waals intermolecular adhesion force as a function of separation distance, D, is [41]

$$F = \left(\frac{A}{6pD^3} \right) \cdot A_s \tag{6.1}$$

where A is the Hamaker constant assumed to have a value in the range of 0.4×10^{-19} - 4×10^{-19} J for condensed phases across air or vacuum [41]. Figure 6.9 shows the adhesion force as a function of separation distance for the range of Hamaker constants given above. It is seen that at a separation distance of 3 nm, the adhesion force can range from 0.12 – 1.2 gm, which is quite significant at the HDI. This example does not take into account the slider's attitude, crown, camber and twist or roughness effects. In the following analysis we account for the slider geometry parameters and will comment on the effect of slider/disk roughness in the discussion section.

6.4 Head-disk interface model

6.4.1 Modeling intermolecular forces

For modeling of the intermolecular forces, we adopted the method of Lin and Bogy who implemented an additional force into the CML Static Air Bearing Simulation Code via the Lennard-Jones potential [36]. The Hamaker constant, A, was taken to be 10^{-19} J and the repulsion constant, B, was taken to be 10^{-76} Jm^6. This method takes the slider air

bearing geometry and flying attitude into account, however, it assumes mathematically smooth surfaces. The fixed attitude solution is found by fixing the attitude of the slider (FH, pitch, and roll) and solving for the forces acting on the slider. When the forces and moments acting on the slider equal those of the suspension, the static solution is obtained. Figure 6.10a shows the resultant intermolecular force acting on the pico size ABS shown in Fig. 6.2 (slider 2) as a function of minimum FH for a roll angle of 1.5 μrad and pitch angle of 40 μrad; similar to the conditions under which slider 2 exhibits unstable proximity. It is seen that as the FH decreases, an attractive force becomes present around 5 nm and by further decreasing the FH, a strong repulsive force becomes present, as expected. The Lennard-Jones model does not allow for physical contact between the slider and disk. The Lennard-Jones modeled force becomes unbounded as the spacing goes to zero due to the repulsion term to simply model physical contact. This simplification in the repulsion term modeling physical contact will be commented on in the discussion section. However, it will be shown that even though the Lennard-Jones repulsion and physical contact are modeled differently, they predict similar dynamic instability results.

6.4.2 Static force analysis

Figure 6.10b shows the resultant force exerted on the slider as a function of minimum FH for the fixed attitude solution. The force consists of the positive and negative (sub-ambient) air bearing forces and the adhesion and repulsion forces from the Lennard-Jones potential. When the intermolecular forces are accounted for there can exist up to three equilibria – two stable and one unstable. It is seen that for small perturbations about the

nominal FH solution of 7 nm, the solution is stable. However, at 2.8 nm, there exists an unstable equilibrium and another stable equilibrium at 0.2 nm. These additional equilibria suggest a very complicated nonlinear system, which is the focus of the following dynamic analysis.

6.4.3 Nonlinear one degree-of-freedom HDI model

In order to simplify the HDI for the following analysis, we used the simple lumped parameter 1DOF model depicted in Fig. 6.11. In this model, the air bearing slider system is modeled with a nonlinear spring, *k(s)*, mass, *m*, and proportional damping, *c*. The nonlinear air bearing stiffness is a function of the slider – disk spacing, *s*, and takes the power-hardening form

$$k(s) = b \cdot s^{a} \tag{6.2}$$

where α and β are constants found by matching with the CML dynamic simulation code as was shown in Chapter 5. The air bearing force can be found from

$$F_{ab}(x) = -k(s) \cdot x = -b \cdot (FH_{ss} + x - d)^{a} \cdot x \tag{6.3}$$

where FH_{ss} is the steady-state FH without accounting for the intermolecular force and x is the slider's absolute displacement: $x = s + d - FH_{ss}$. The disk topography, *d(t)*, can be modeled in various ways; as a numerically generated random wavy surface, a harmonic excitation, or using an experimentally measured disk topography. The intermolecular force, F_{vdW}, acting on the slider takes the form

$$F_{VdW}(s) = -\frac{A'}{s^3} + \frac{B'}{s^9} = -\frac{A'}{(FH_{ss} + x - d)^3} + \frac{B'}{(FH_{ss} + x - d)^9} \tag{6.4}$$

where A' and B' are constants found from curve fitting plots similar to Fig. 6.10a where the first term is the attraction force and the second term is the repulsion force. The equation of motion for this system can be written in terms of the sliders absolute displacement, x

$$m\ddot{x} + c\dot{x} + (k - F_{VdW})x + (F_{VdW} - k)d - c\dot{d} = 0 \tag{6.5}$$

Due to the intermolecular force in Eq. (6.4) and the nonlinear spring stiffness in Eq. (6.3), Eq. (6.5) becomes highly nonlinear, and due to the addition of the intermolecular force, the solution is not simple.

6.5 Head-disk interface nonlinear analysis

6.5.1 Stability

Stability of the HDI model can be analyzed by considering the energy of the system. If we assume no forcing, $d(t) = 0$, and no damping, $c = 0$, the system is conservative and a potential energy method can be used to show equilibria and local stability. The potential energy of the system, U_{sys}, is comprised of the potential energy of the air bearing spring, U_{ab}, and the potential energy of the intermolecular force, U_{vdW}, derived from the Lennard-Jones potential. These conservative forces are related to their potential energies through

$$F(x) = -\frac{\partial U}{\partial x} \tag{6.6}$$

The total potential energy can be found by integrating the air bearing force, F_{ab}, and the intermolecular force, F_{vdW}

$$U_{sys} = U_{ab} + U_{vdW} = -\left[\int F_{ab}dx + \int F_{VdW}dx\right] =$$
$$-\left[\int -\left(b\left(FH_{ss}+x\right)^{a}x\right)dx + \int\left(-\frac{A'}{\left(FH_{ss}+x\right)^{3}} + \frac{B'}{\left(FH_{ss}+x\right)^{9}}\right)dx\right] \tag{6.7}$$

The criteria for equilibrium, x_i^*, is satisfied when the system's potential reaches an inflection point

$$\frac{\partial U_{sys}}{\partial x} = 0 \tag{6.8}$$

and the equilibrium point is stable if the potential evaluated at equilibrium is a local minimum

$$\left.\frac{\partial^2 U_{sys}}{\partial x^2}\right|_{x_i^*} > 0 \tag{6.9}$$

and is unstable if the potential evaluated at equilibrium is a local maximum

$$\left.\frac{\partial^2 U_{sys}}{\partial x^2}\right|_{x_i^*} < 0 \tag{6.10}$$

For the nominal coefficients used, as shown in Table 6.1, equilibria and stability as a function of FH_{ss} can be obtained. Figure 6.12 shows the potential energies of the air bearing, the Lennard-Jones potential and the total system potential at FH_{ss} = 7.75 nm as a function of spacing. It is seen that when the air bearing and the Lennard-Jones potentials are added, the system has one equilibrium, FH_{eq}, and it is stable, where $FH_{eq} = x_i^* + FH_{ss}$. In Fig. 6.13, the total potentials for FH_{ss} = 7.75, 5.75, 4.75, and 1.25 nm are shown as a function of spacing. It is seen, at FH_{ss} of 7.75 nm, one stable equilibrium exists at FH_{eq} = 7.75 nm. At FH_{ss} = 5.75 nm, there exists two stable and one unstable equilibria at FH_{eq} =

5.75, 0.35, and 0.7 nm, respectively. At FH_{ss} = 1.25 nm, the air bearing is overcome by the intermolecular force and only one stable equilibrium exists, FH_{eq} = 0.25 nm. The equilibria and stability as a function of FH_{ss} can be summarized in the bifurcation plot shown in Fig. 6.14. It is seen that when FH_{ss} is greater than 6.3 nm only one equilibrium exists, x_1^*, the nominal FH solution. Between FH_{ss} of 1.35 nm and 6.3 nm, three equilibria exist – two stable, x_1^* and x_3^* and one unstable, x_2^*. At FH_{ss} of 1.35 nm, only one stable equilibrium exists, x_3^*. The regime where the three equilibria exist is of utmost interest – both theoretically and for practical application.

Between FH_{ss} of 1.35 nm and 6.3 nm in Fig. 6.14 three equilibria exist and within this regime the potential energy takes on a special form generally called a "double-well" or "two-well" potential. Double-well potential systems have been studied for the past two decades in the field of nonlinear dynamics [42] - [45]. Many systems have exhibited double-well potentials with very interesting dynamics, from mechanical systems to super conductivity. Within this regime, the dynamics of the system are extremely complex and can even be chaotic [42] - [45]. A detailed nonlinear dynamics analysis of this system investigating periodic solutions, limit cycles, and transitions to chaos are interesting to study, however, the practical issues associated with the HDI would be over shadowed in such a complete study. The details concerning the HDI stability and instability are of more interests to us here, and they are discussed in detail.

6.5.2 Unforced system

This system is considered to be unforced when the disk forcing is zero, $d(t) = 0$ (e.g. for a perfectly smooth disk surface). From the bifurcation plot in Fig. 6.14 we observe one very important characteristic of the unforced system. This observation can be explained by a touchdown (TD) – takeoff (TO) simulation by decreasing and then increasing the FH_{ss}. From Fig. 6.14, the FH_{eq}'s can be found as a function of FH_{ss} as the FH_{ss} is lowered from 10 nm to 1 nm and then increased back to 10 nm. As the FH_{ss} is decreased from 10 nm to 1.35 nm, the equilibrium follows the nominal solution, x_1^* (a-b). However, at the FH_{ss} of 1.35 nm, the air bearing is overcome by the intermolecular force and the nominal solution is annihilated by x_2^* and the slider "snaps" down to the other stable equilibrium, x_3^* (b-c). Upon increasing the FH_{ss} back to 10 nm, the equilibrium solution will remain along x_3^* until it is annihilated by x_2^*, at a FH_{ss} of 6.3 nm (d-e). At $FH_{ss} = 6.3$ nm the equilibrium solution "snaps" from x_3^* to x_1^*, back to the nominal solution (e-f). This is illustrated in Fig. 6.15, which depicts an unforced TD – TO simulation showing the slider remaining "stuck" on the disk until the FH_{ss} reaches 6.3 nm. The difference between the FH_{ss} at which the slider becomes "stuck" while decreasing the FH_{ss} and where the slider becomes "unstuck" while increasing the FH_{ss} is the unforced "FH hysteresis". It is seen that for the unforced system the FH hysteresis is bound by the regime were multiple equilibria exist – namely the three equilibria, x_1^*, x_2^*, and x_3^*.

Figure 6.16 shows a sketch of the energy surface in state-space (x versus $\dot{x}$) and the trajectories projected onto the state-space within the regime where the multiple equilibria exist, $1.35 < FH_{ss} < 6.3$ nm. Since the unforced and undamped system is conservative, the

systems trajectory remains on a level contour of the energy surface. Depending on the initial conditions the system will behave differently. In Fig. 6.16b, it is seen that for a relatively low energy state, $E < E_2$, with initial conditions near x_3^* or x_1^*, the slider oscillates about x_3^* or x_1^*, respectively, with small amplitudes. However, if enough initial energy is applied, $E > E_2$ the system remains in high amplitude oscillations about both x_1^* and x_3^*. The energy state that separates the oscillations about x_1^* or x_3^* and oscillations about both x_1^* and x_3^*, E_2, is defined as the homoclinic orbit or separatrix shown in Fig. 6.16. By adding damping, c, the systems trajectory would end up spiraling down into either x_1^* or x_3^* depending on the initial conditions as seen in Fig. 6.17. Two sets of initial conditions were chosen to illustrate the sensitivity to initial conditions: *(FH , velocity) = (6.3 nm , -0.3945 mm/s)* and *(FH , velocity) = (6.3 nm , -0.394 mm/s)*. It is seen that one of the trajectories spirals into x_1^* and the other spirals into x_3^*. The dynamics associated with the unforced system are rather simple as described above. However, once this type of system is forced, the sliders response becomes very nontrivial and highly unpredictable.

6.5.3 Forced system

Forced double-well potential systems have been found to exhibit *strange attractors* causing chaos and sensitivity to initial conditions; however, the important result for the HDI can be summarized as follows [42]-[45]. As long as the model of the HDI exhibits a double-well potential the forced solution can be periodic, non-periodic, or chaotic for simple harmonic forcing. The homoclinic energy level separating oscillations about x_1^* or x_3^* and x_1^* and x_3^* can no longer be used to approximately predict the slider's response.

That is, for the nominal parameters used, this system can exhibit non-predictable chaotic dynamics between FH_{ss} of 1.35 nm and 6.3 nm. The slider motion is defined as *stable* if it oscillates about the x_1^* equilibrium and *unstable* of all other motions. This choice of terminology describes the nominal flying condition as stable and large chaotic slider oscillations as unstable.

6.5.3.1 Touchdown – takeoff simulations

The topography of a disk is composed of harmonic and non-harmonic content at all wavelengths or frequencies as the disk spins. Figure 6.18 shows the experimentally measured frequency spectral contents of two disk's morphology as seen by the slider as the disk spins. Both disks are "super-smooth" media, however, it is seen that disk A is smoother than disk B across the entire spectral band. Figure 6.19 shows a TD – TO numerical simulation that is similar to that shown in Fig. 6.15, however the system is now forced with the measured disk topography from disk A. It is found that while decreasing FH_{ss} the slider "snaps" from stable motions about x_1^* into chaotic high amplitude oscillations. Upon increasing FH_{ss}, stable slider motion is resumed about x_1^*, exhibiting a FH hysteresis. Because this system exhibits *strange attractors* in the sub- 6 nm FH regime, the characteristics of the chaotic slider motion are highly dependent on the disk forcing. However, for all disk topographies investigated an unstable motion exhibiting a FH hysteresis was always present due to the intermolecular force. By qualitatively comparing the experimental result in Fig. 6.1b with the simulation results in Fig. 6.19 we see that the maximum amplitude of vibration does not occur at the lowest FH_{ss}, but rather it occurs after the minimum FH_{ss} has been reached and increases with increasing FH_{ss}.

6.5.3.2 Transition between stable and unstable flying

Experimentally it was shown that by changing the FH only slightly the transition between stable and intermittent unstable flying was abrupt (see Fig. 6.1a). Numerical simulations have also been carried out showing this phenomenon in which the FH_{ss} is held fixed. Within the regime where the system exhibits a double-well potential, it has been shown that the slider can be easily forced into unstable high amplitude oscillations. Figure 6.20 shows the slider motion exhibiting intermittent instability at FH_{ss} = 3.35 nm. Figure 6.21 shows a similar simulation without including the intermolecular force. These two figures show that the intermittent instability here is due to the inclusion of the intermolecular force. By slightly increasing the FH_{ss}, the instability ceases to exist and by slightly decreasing the FH_{ss}, the instability will persist indefinitely. Under these conditions, the slider has the ability to oscillate about x_3^*, x_1^*, or both x_3^* and x_1^* and can switch between oscillation states chaotically. Figure 6.22 presents a plot of the state-space showing oscillations about x_3^*, x_1^*, and both x_3^* and x_1^*. Figure 6.23 shows the chaotic nature of the system as it switches between oscillation states. It is seen that when the system becomes unstable, the most likely oscillation state of the slider is oscillation about both x_3^* and x_1^*. It is possible for the slider to oscillate about x_3^* but due to the disk forcing, the slider cannot continue oscillating about this equilibria. If a slider could remain in the state of oscillation about x_3^*, a stable sub- 1 nm FH slider could be realized. However, due to disk waviness, roughness and glide-height, the result is high amplitude unstable oscillations.

6.6 Parametric study

The above 1DOF system used to simulate the HDI is greatly simplified to give an understanding of the effects of adding intermolecular forces in the system and to show how certain parameters affect HDI dynamic stability. However, due to the assumptions made in reducing the HDI to a 1DOF system, the results must be viewed as merely qualitative. It is desired to make the HDI as stable as possible, and thus far it has been shown that stability can be highly compromised when flying in the sub– 6 nm regime due to the presence of intermolecular forces. Nominal values have been used in the simulations presented. Next we present some qualitative results on how these parameters affect the HDI stability as they are varied.

It was shown that the slider has the ability to become unstable when multiple equilibria exist. Therefore, if it were possible to exclude this regime of multiple equilibria, the slider system dynamics would be much simplified, and not exhibit instability and a FH hysteresis due to intermolecular forces. However, the inclusion of the intermolecular forces in the modeling will always predict this regime. The bifurcation plot in Fig. 6.14 is useful in visualizing the regime where multiple equilibria exist, and the model elements controlling the location and length of this regime are both the intermolecular and the air bearing forces.

6.6.1 Intermolecular force

The cause of the complicated dynamics of this system stems from the intermolecular force. By simply scaling the intermolecular force in Eq. (6.4) as shown in Fig. 6.24, we

obtain the corresponding bifurcation plots as shown in Fig. 6.25, which clearly illustrates its effect on HDI stability. It is seen that by decreasing the intermolecular force to one-fourth and one-half its nominal value, the multiple equilibria regime shrinks from $1.35 < FH_{ss} < 6.3$ nm to $0.9 < FH_{ss} < 1.8$ nm and $1.1 < FH_{ss} < 3.3$ nm, respectively. These decreases result in much smaller FH regimes where the system has the ability to become unstable. On the other hand, by increasing the intermolecular force by two times its nominal value, the multiple equilibria regime increases to $1.65 < FH_{ss} < 12.3$ nm. Figure 6.26 presents plots of the slider's motion flying over a measured disk topography at a FH_{ss} of 3 nm for different amplitudes of the intermolecular force. It is seen that as the intermolecular force increases, so does the instability of the HDI. Figure 6.27 shows the TD – TO FH hysteresis simulation results as a function of intermolecular force amplitude. It is seen that as the intermolecular force is increases, so does the FH hysteresis.

Even though the intermolecular force cannot be attenuated completely, there are ways to reduce its effect. Decreasing the effective slider area within proximity of the disk is the most effective method (recall Eq. (6.1)). This reduction in area can come from texturing the ABS, through design of the ABS rails, form-factor (nano, pico, femto, etc.) and by slider attitude. Figure 6.28 shows the intermolecular force as a function of minimum spacing for different pitch angles and form-factors for two different ABS designs. It is seen that the larger the rear ABS rail within proximity of the disk surface, the higher the adhesion force. Also, other factors such as crown, camber and twist will substantially affect the adhesion force. By simply decreasing the rear ABS pads area, the adhesion

force decreases, however, for manufacturability, flyability, stability, and other design criteria, the rear ABS pad has to have certain minimum dimensions. Also, the intermolecular force scales proportionally with the Hamaker constant. In this analysis, a nominal value of $A = 10^{-19}$ was used, however, this value is only approximate. A more accurate value of the Hamaker constant needs to be obtained for the HDI. Also, surface chemistry could also change the Hamaker constant between various lubricants and DLC coatings. Some recently published values of the HDI Hamaker constant are $A = 0.724\times10^{-19}$ J with lubricant on the disk surface and $A = 1.80\times10^{-19}$ J without lubricant at the interface [38]. These values are close to what has been used in this analysis; therefore it is expected that the adhesion force will always be present below 3.5 nm FH's causing possible HDI instabilities.

6.6.2 Air bearing stiffness: nonlinear

The air bearing stiffness is another variable affecting the nature of multiple equilibria. The air bearing stiffness is a function of the ABS design, suspension pre-load, slider attitude, relative disk velocity, and other design parameters. Generally, the linearized "vertical" resonant mode of vibration of an air bearing – slider system is between 150 kHz and 400 kHz. For large oscillations, the slider exhibits a power hardening stiffness as modeled in Eq. (6.2). A change in the stiffness by factors in the range of 0.25 – 4 changes the linearized resonant frequency half to twice the nominal value: 108.6 – 434.4 kHz. The bifurcation plots associated with the factors 0.25 and 4 are shown in Fig. 6.29. A series of simulations was performed at a FH_{ss} of 3 nm showing how the stiffness affects the HDI stability. It is seen from the results shown in Fig. 6.30 that stability increases as the

air bearing stiffness increases. Also, the TD – TO FH hysteresis was simulated as a function of air bearing stiffness, and the results are shown in Fig. 6.31. The trend between the FH hysteresis and air bearing stiffness does not appear to be monotonic. This is due to the complex disk forcing function and the varying air bearing resonant frequency as the stiffness changes. The disk topography frequency spectra is not uniform across the frequency band, and at different resonant frequencies, the disk affects resonance differently. However, there is an overall decreasing trend of the FH hysteresis as the stiffness is increased.

6.6.3 Air bearing stiffness: linear

If the air bearing stiffness were linear and not a power-hardening nonlinear spring as described in Eq. (6.2), the bifurcation plot would be affected as would be the stability. In Fig. 6.32 the bifurcation plots are shown for linear stiffnesses of $k_o = 3\times10^6$ N/m, $k = k_o*2$, and $k = k_o*4$. In comparing these results with those for a nonlinear air bearing stiffness in Fig. 6.29 we see that the FH regime where all three equilibria exist (unstable regime) is larger for the linear stiffness cases. By increasing the extent of the unstable regime, we know that the stability of the HDI would be less. We conclude that the power-stiffening air film of an actual air bearing is extremely beneficial in increasing the stability of the HDI.

6.6.4 Air bearing damping

As with the air bearing stiffness, air bearing damping is also a function of many parameters. Generally, the linearized “vertical” mode damping is between 1 % to 5 % of

critical damping. In the previous two sections the bifurcation plots were used to show the degree of instability. On the other hand, air bearing damping does not change the bifurcation plots. In nonlinear systems, generally, more damping enhances stability. Indeed we find similar results here. Figure 6.33 presents the effect of damping on slider instability at a FH_{ss} of 3.4 nm as the damping is varied from 0.46 to 3.64 %. It clearly shows that the higher the damping, the more stable the HDI becomes. Also, the dependence of the FH hysteresis on damping as determined by TD – TO simulations is summarized in Fig. 6.34, which shows that the FH hysteresis decreases as the damping is increased.

6.6.5 Disk topography

As seen in Fig. 6.18, disk topographies can vary substantially depending on substrate material, texturing, and other process conditions. The forcing and initial conditions of nonlinear systems of the type described here are the most sensitive variables to their chaotic nature that leads to the unstable oscillations. When the HDI model exhibits a double-well potential chaotic oscillations can arise even when it is forced by a single harmonic excitation. Figure 6.35 shows a plot of single frequency disk forcing amplitude, A_d, where the slider steady-state motion becomes unstable versus disk forcing frequency, f_d, where $d(t) = A_d \sin(2\pi f_d)$ and the initial conditions are *(FH , velocity) = (3.4 nm , 0 mm/s)* at a FH_{ss} =3.4 nm. Above the curve shown in Fig. 6.35, the slider's response is unstable and below it, the response is stable for a single frequency excitation. It is observed that the most sensitive forcing frequency is around the systems linearized resonant frequency of approximately 175 kHz. Unfortunately a technique such as

superposition cannot be used to extend the results in Fig. 6.35 to the complicated disk forcing by an actual disk. Figure 6.36 compares the TD – TO FH hysteresis simulation results for the two disks A and B described in Fig. 6.18. It is observed that as the FH_{ss} transitions from 12.65 – 4.65 – 12.65 nm, disk B forces the HDI to transition into unstable slider oscillations while the forcing of disk A is too small at these FH_{ss} to transition the slider into unstable oscillations. This result suggests that wavier and rougher disks result in HDI instability at much higher FH_{ss} values. By just varying the amplitude of the waviness and roughness of disk A we perform another parametric study with the results presented in Fig. 6.37, which shows the TD – TO FH hysteresis simulations for amplitude multiples of 0.25 to 4 times its original topography. It is observed that as the disk topography amplitude is increased the FH hysteresis remains relatively constant at $DFH \approx 1$ nm, but the unstable response amplitude increases.

6.7 Discussion

Experimental evidence of low FH slider instabilities is evident from two effects: (1) the "snapping" effect from stable to intermittently unstable and further to indefinitely unstable proximity and, (2) the presence of the TD – TO FH hysteresis. Adhesion forces due to capillary (meniscus) effects appear unlikely to be the cause of these instabilities due the short time duration the slider is in contact with the lubricant film. Also, the experimental FH hysteresis results showed no dependence on lubricant thickness, for the thickness range tested. On the other hand, the time independent intermolecular adhesion force was shown to be significant when a slider and disk come within proximity of each other. The Lennard-Jones model was used to incorporate additional adhesion and

repulsion forces into the CML Static Air Bearing Simulation Code solutions and into a simple lumped parameter 1DOF model. The 1DOF model was used for investigating the experimentally observed nonlinear dynamics associated with the HDI. It was shown from bifurcation plots of the system, that as the FH approaches sub– 6 nm, multiple equilibria exist. Also, for lower FH, the intermolecular force overcomes the air bearing load capacity and the slider "snaps" down onto the disk. From a static analysis, one would expect that the only effect caused by intermolecular forces are at low FH's would be a static spacing loss, and by further decreasing the FH, the intermolecular forces would overcome the air bearing load capacity (Fig. 6.10b). However, a much greater effect arises when including the intermolecular force that has not been previously addressed – that of dynamic instability. It was shown that the possibility of the HDI becoming dynamically unstable is restricted to a regime where multiple equilibria exist, which extends into FH's much higher than those resulting from static analysis. The dynamics associated with a double-well potential system can be quite complicated when the system is forced, as was shown. The chaotic characteristic of the system with a double-well potential is what causes the HDI instability due to intermolecular forces. By numerically investigating both constant FH and the hysteresis TD – TO process, we were able to reproduce the experimental findings of HDI instability and FH hysteresis. Also, several qualitative features demonstrated by the experimental and simulation results are in agreement, including the effect of adding small DLC pads to decrease the sliders instability vibrations (decreases adhesion forces) and the asymmetric slider vibration amplitude during the TD – TO process.

These results imply that the HDI has a fundamental lower limit of FH at which the slider remains stable. This lower limit is a function of not only the disk morphology but also the ABS design and slider attitude. For the nominal values studied here it was shown that the slider transitions into unstable oscillations at a FH_{ss} of 3 nm and 4.6 nm while flying over two different disks, A and B, respectively. It was shown by a parametric study that the FH at which instability occurs, as well as the severity of the oscillations, change with the parameters. The effect of the parameters discussed must be understood to obtain a stable HDI design when flying extremely low. Also, it was shown that the power-stiffening feature of an air bearing increases the HDI stability. In order of importance, we found that the following parameters can be adjusted to obtain maximum HDI stability: (1) the intermolecular force should be reduced, (2) the disk morphology and slider should be optimized to produce minimum FHM, (3) air bearing stiffness should be increased, and (4) air bearing damping should be increased. It was shown for all the parameter values studied that HDI stability can always be compromised, however, by considering the findings in this chapter, the instability due to intermolecular forces can be minimized.

The analysis presented here is based on adhesion modeled by the Lennard-Jones potential. The functional form of the repulsion term in Eq. (6.4) stems from the need for a repulsion term as the two mating surfaces contact one another. This approach lacks physical basis due to the fact that the two surfaces never actually come into contact. A more physical and complicated approach would be to model the repulsion as a contact force, similar to what was done in the Derjaguin-Muller-Toporov (DMT) model and the extension that Cheng, Etsion and Bogy (CEB) made [46] - [48]. In the DMT and CEB

models, the attractive force is similar to Eq. (6.4) but the repulsion force stems from physical contact as seen in Fig. 6.38. For a simple spherical asperity impinging on a flat surface the forces generated as a function of separation distance are [46], [47]:

$$F_{vdW}(x) = -\frac{AR}{6x^2} \qquad \text{for } x > a_o$$

$$F_{DMT}(x) = -\frac{AR}{6x^2} + \frac{4}{3}E^*\sqrt{R}(a_o - x)^{3/2} \qquad \text{for } x \le a_o \tag{6.11}$$

where R is the radius of the spherical asperity, E^* is the effective elastic modulus, and a_o is the intermolecular distance usually taken to be about two angstroms. However, by comparing the additional force that is generated by Eq. (6.4) (see Fig. 6.24) and by the DMT and CEB models, we find that similar force curves are generated. Therefore, by using either the simplistic approach of the analysis in this chapter in modeling the repulsion by Eq. (6.4) or by including a complex contact force from the CEB model, we would expect to find qualitatively similar dynamic instability results.

Another simplification of the modeling here was to neglect surface roughness effects. It can be seen from Eq. (6.1) that the adhesion force scales proportionally with the area within proximity. Due to the qualitative nature of the 1DOF HDI model, the roughness effect can be discussed only qualitatively. By including the surface roughness of the slider and disk, we would expect the adhesion force to be effectively decreased. This effect is covered in the parametric study of scaling the intermolecular force. Increasing roughness decreases the intermolecular force, hence, leads to an increase in HDI stability. However, in order to achieve a non-contact 3.5 nm FH HDI, the slider and disk surfaces must be extremely smooth.

6.8 Conclusion

Experimentally it is observed that as a slider flies within proximity of the disk HDI dynamic stability is lost. Additional forces due to capillary and intermolecular adhesion were considered. Due to the kinetic formation of a meniscus and the experimental results presented, we concluded that meniscus forces need not be considered in the dynamic modeling of the HDI. A nonlinear dynamic analysis of a modeled HDI incorporating intermolecular forces revealed a new kind of dynamics that cannot be captured by static analysis. By analyzing the systems equilibria and stability, it was found that multiple equilibria exist in the sub – 6 nm FH regime associated with a double-well potential. Within this regime the sliders motion can be stable or chaotically unstable when it is externally forced by a disk topography. From the analytical and numerical analysis presented here, the experimentally measured FH hysteresis, the intermittent slider instability and the abrupt transition between stable and unstable proximity can be explained. A parametric study was used to show how the variables affect HDI stability. Also, the effect of the power-hardening air bearing stiffness was shown to be beneficial in increasing HDI stability. By optimizing the parameters such as the air bearing design and the disk morphology, the stability of the HDI can be improved. However, for practical values of the parameters, it is found that instability is likely to occur when flying below 6 nm. From these results, we are forced to conclude that there may be a fundamental lower FH limit for a given slider – disk combination, below which the slider would not be able to fly due to HDI dynamic instability caused by intermolecular adhesion forces.

Parameter	Nominal Value	Parameter	Nominal Value
b	244.1 [N/m]	B'	2.7×10^{-88} [N·m^9]
a	-0.48	m	1.6158×10^{-6} [kg]
A'	1.8×10^{-30} [N·m^3]	c	0.08 [N·s/m]

Table 6.1. Nominal values of constants used.

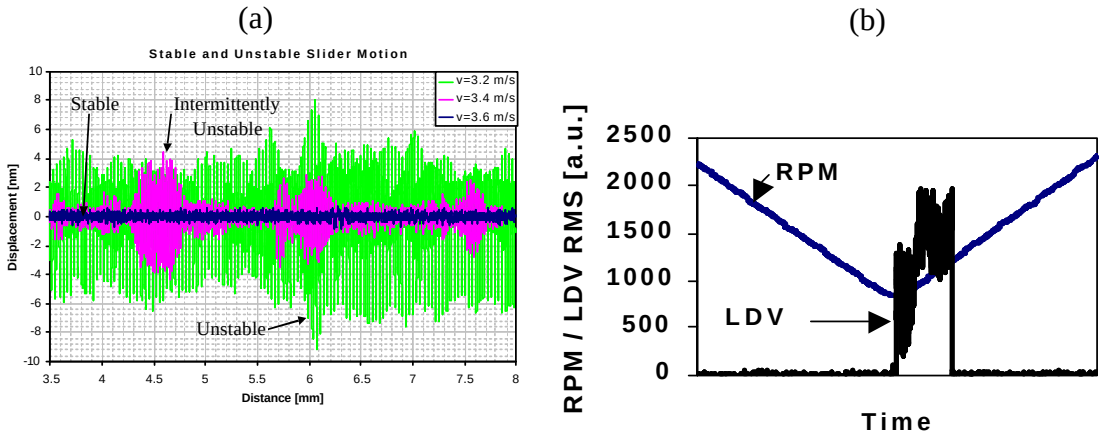

Fig. 6.1. (a) Time trace of the stable, intermittently unstable, and indefinitely unstable slider motion measured by LDV. (b) Measurement of the FH hysteresis as the FH is lowered and increased by changing the disk RPM.

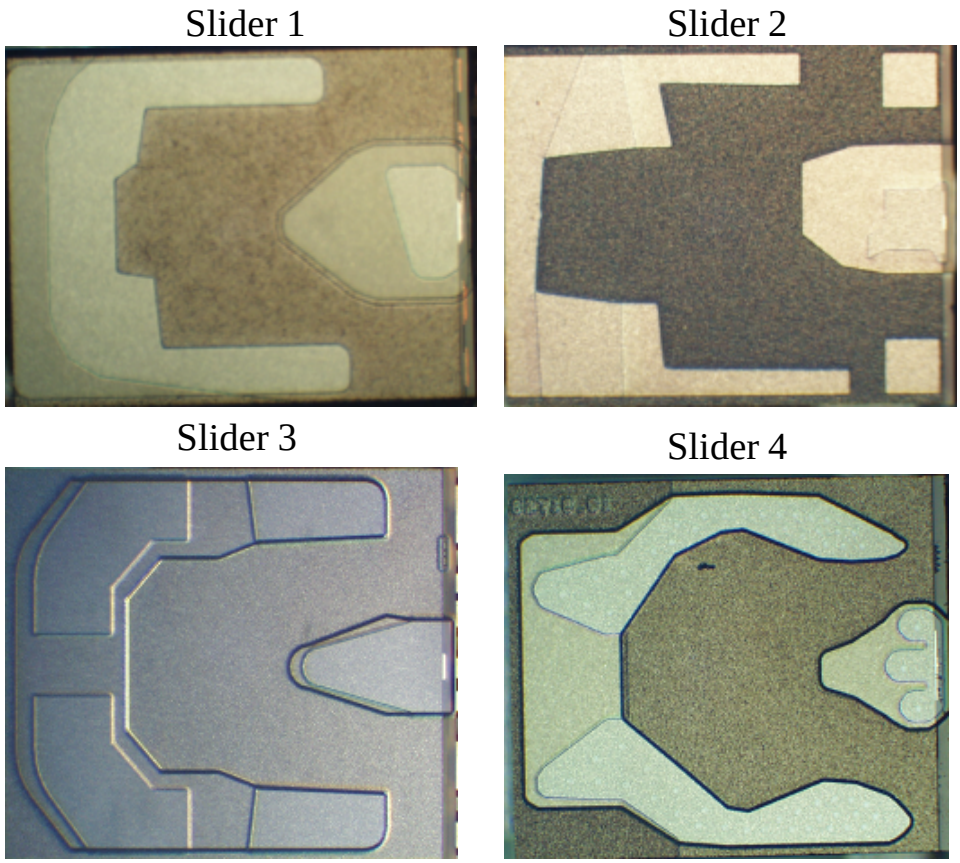

Fig. 6.2. Air bearing surface designs of four different pico size sub-ambient sliders.

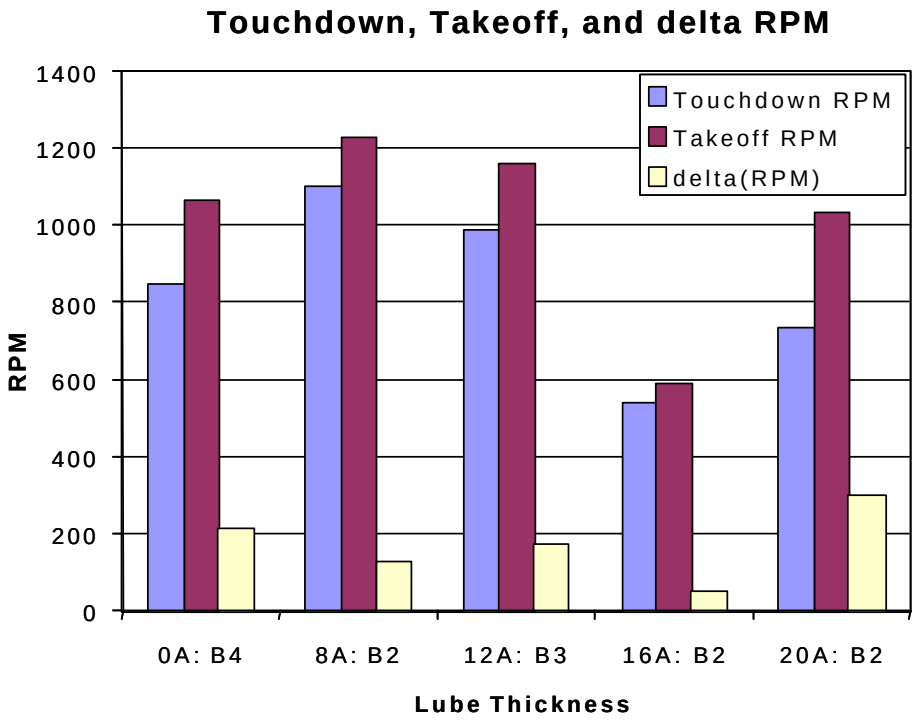

Fig. 6.3. Touchdown, takeoff, and FH hysteresis as a function of lubricant thickness for slider 1.

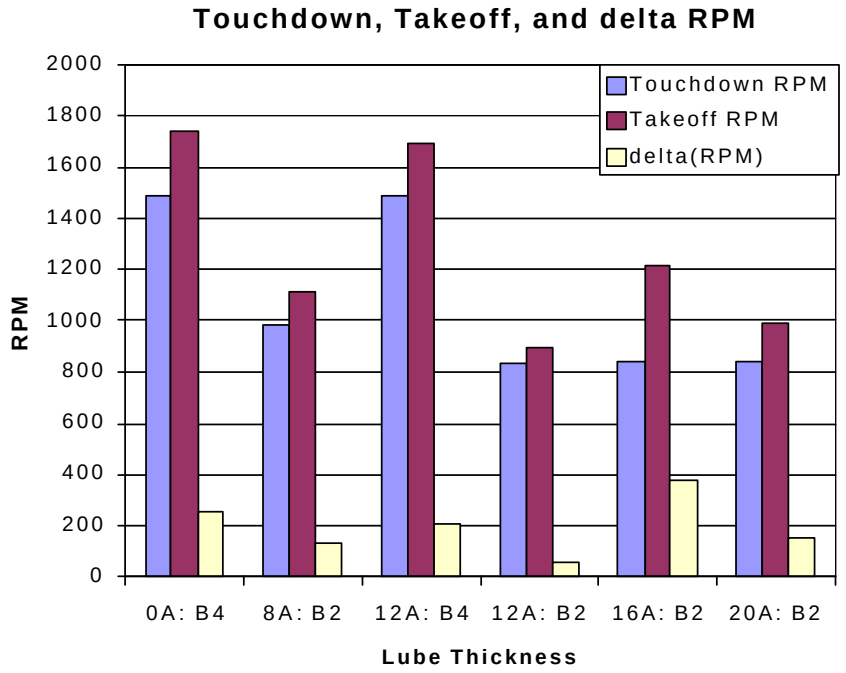

Fig. 6.4. Touchdown, takeoff, and FH hysteresis as a function of lubricant thickness for slider 2.

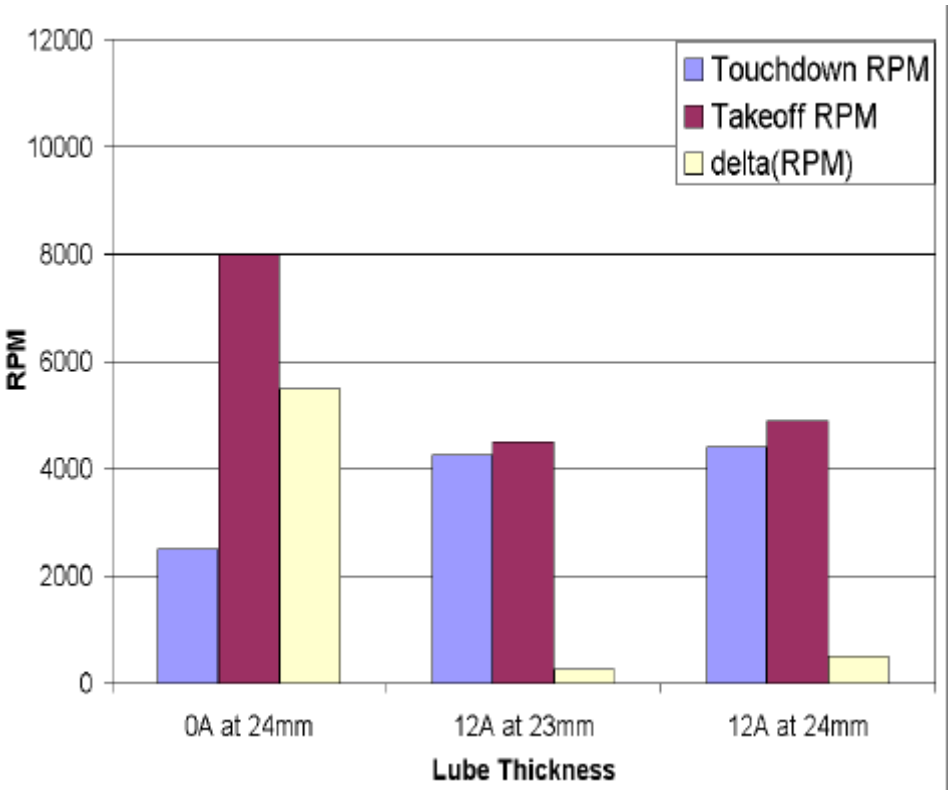

Fig. 6.5. Touchdown, takeoff, and FH hysteresis as a function of lubricant thickness for slider 3.

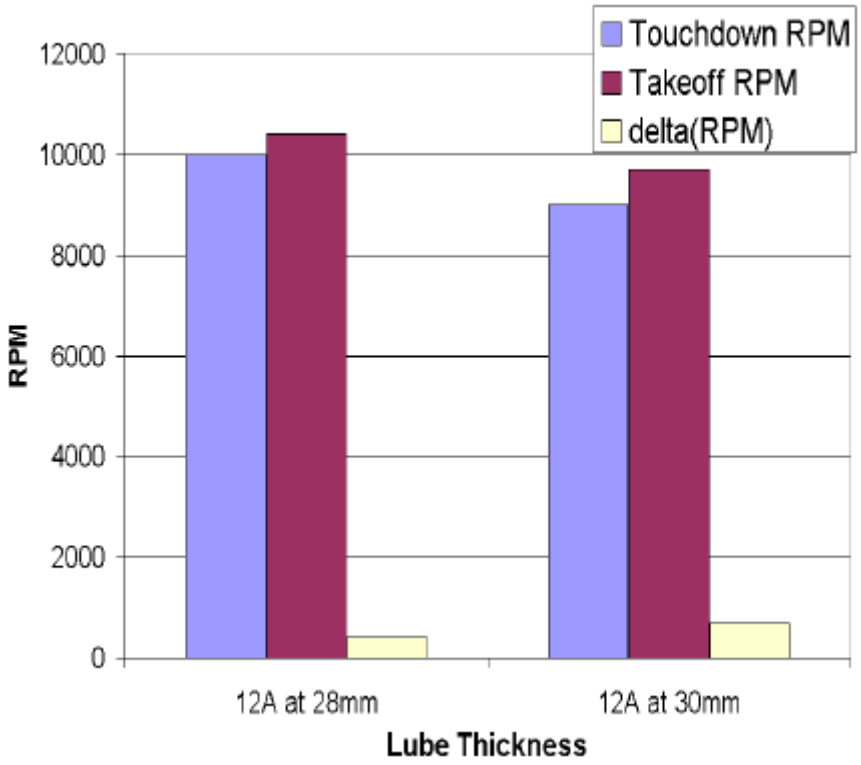

Fig. 6.6. Touchdown, takeoff, and FH hysteresis as a function of lubricant thickness for slider 4.

(a) (b)

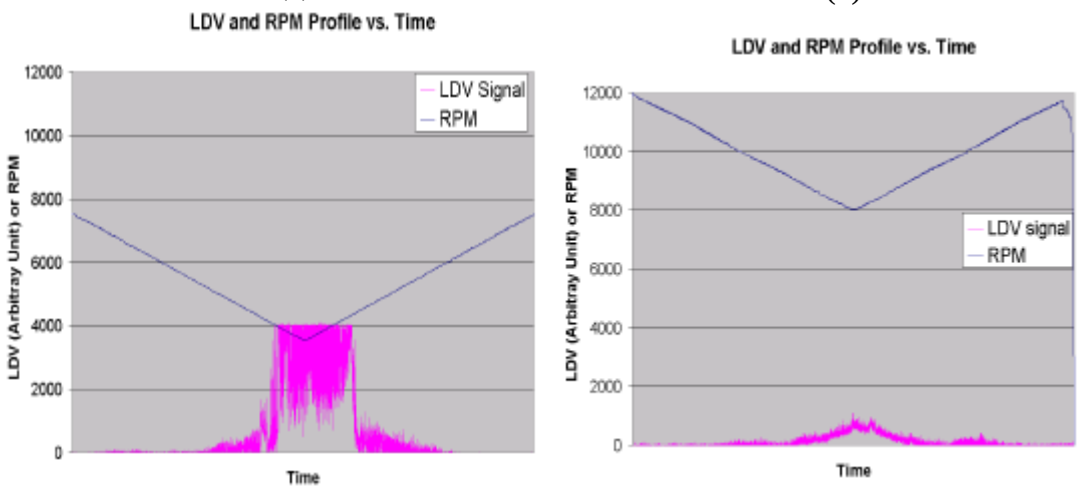

Fig. 6.7. Typical time traces of the RPM and LDV RMS for sliders (a) 1- 3 and slider (b) 4.

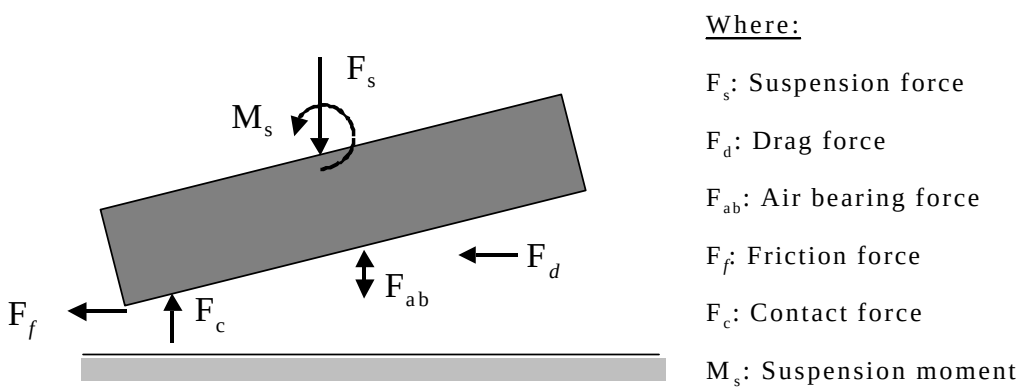

Fig. 6.8. Free-body diagram of the air bearing – slider model.

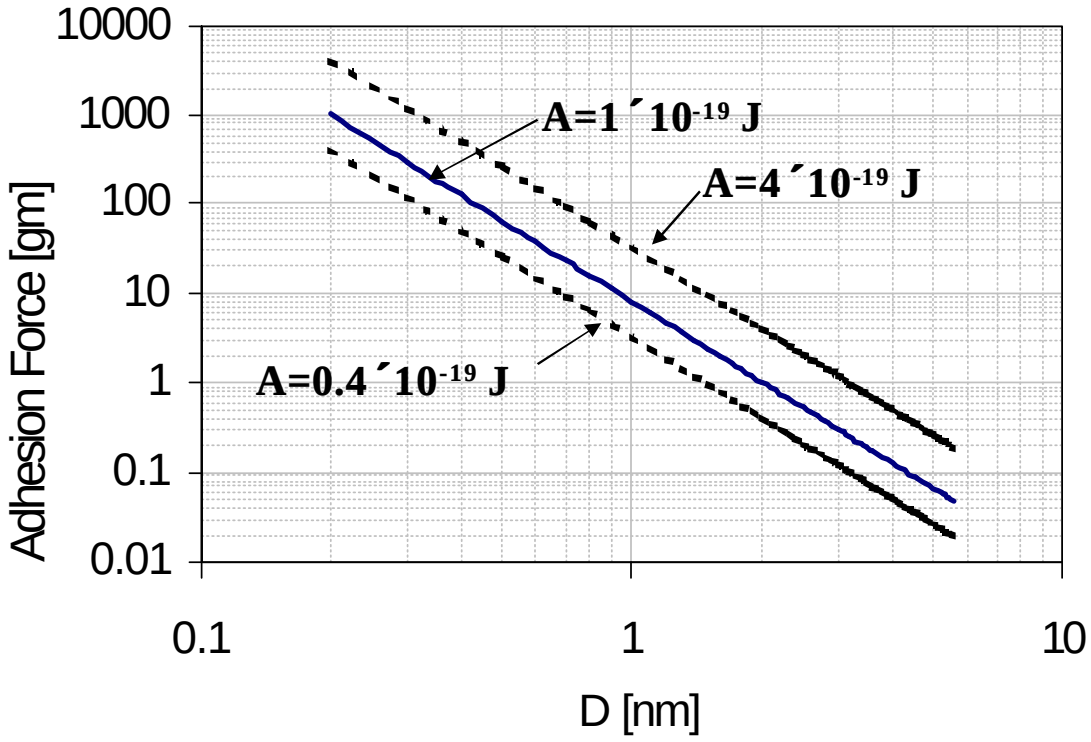

Fig. 6.9. Intermolecular adhesion force as a function of separation distance for two parallel flat surfaces.

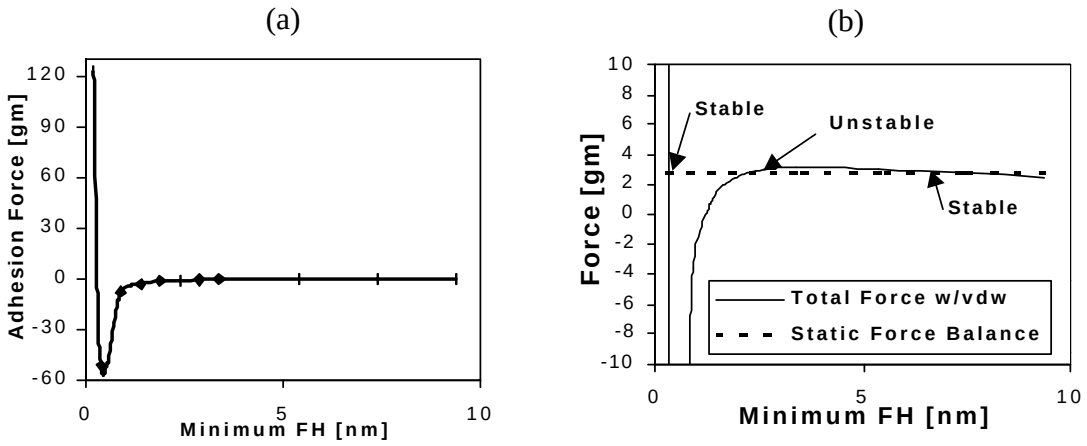

Fig. 6.10. (a) Intermolecular adhesion force modeled by the Lennard-Jones potential and (b) the resultant force acting on the air bearing as functions of the minimum FH.

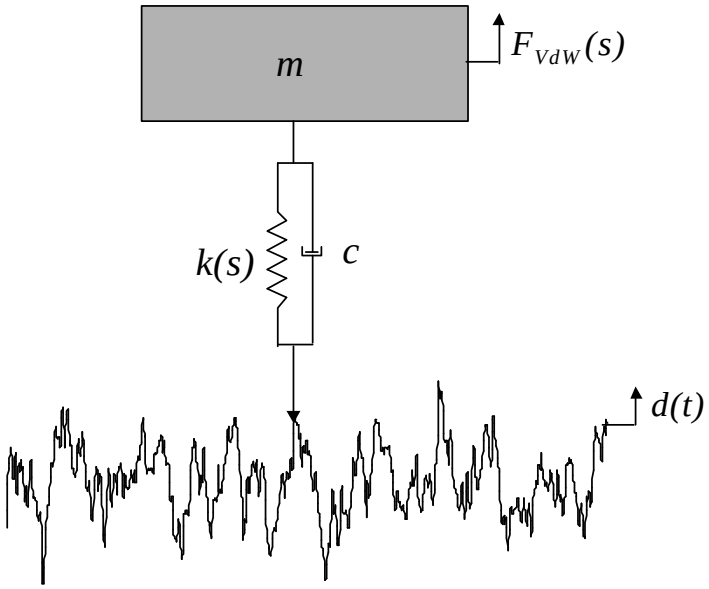

Fig. 6.11. Schematic of the 1DOF nonlinear model.

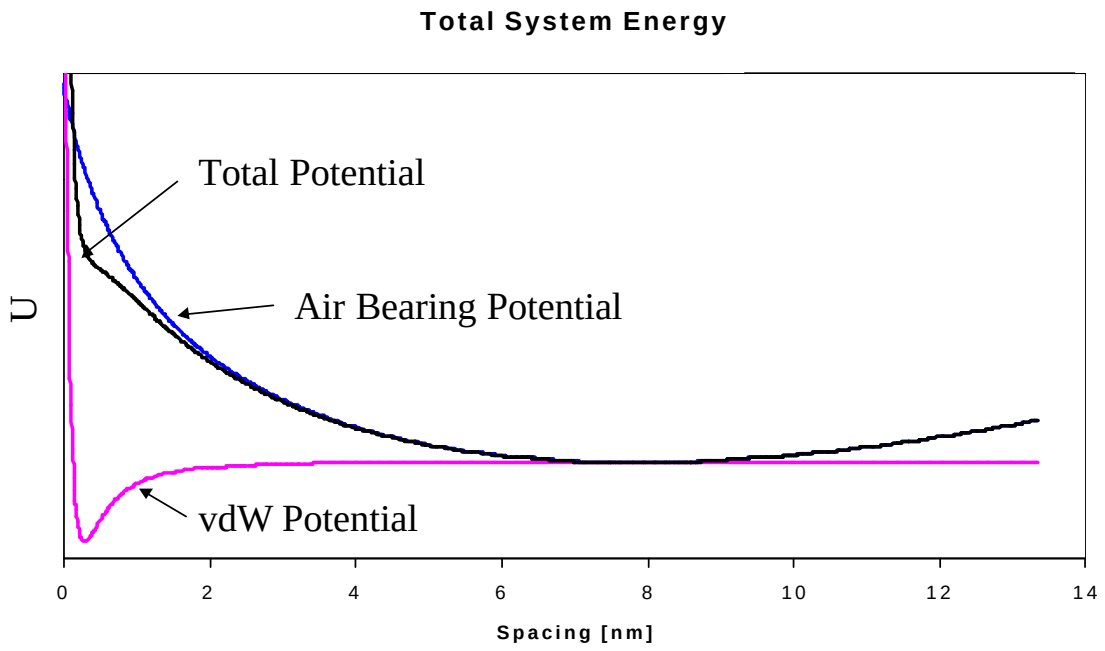

Fig. 6.12. Potential energy curves of the air bearing, Lennard-Jones and the total system at a FH_{ss} of 7.75 nm.

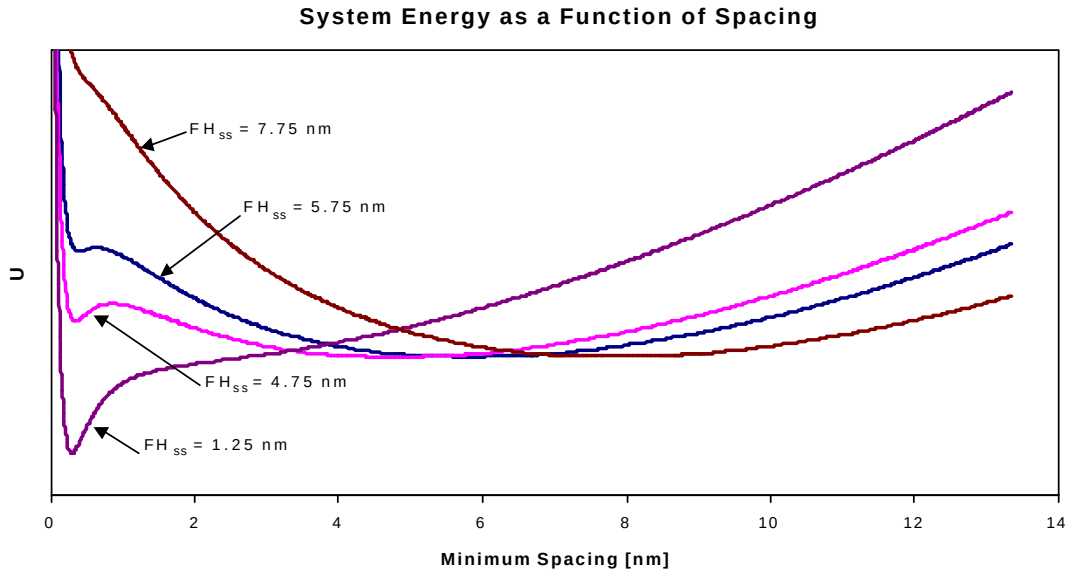

Fig. 6.13. Total system potential energy curves at a FH_{ss} of 7.75, 5.75, 4.75, and 1.25 nm.

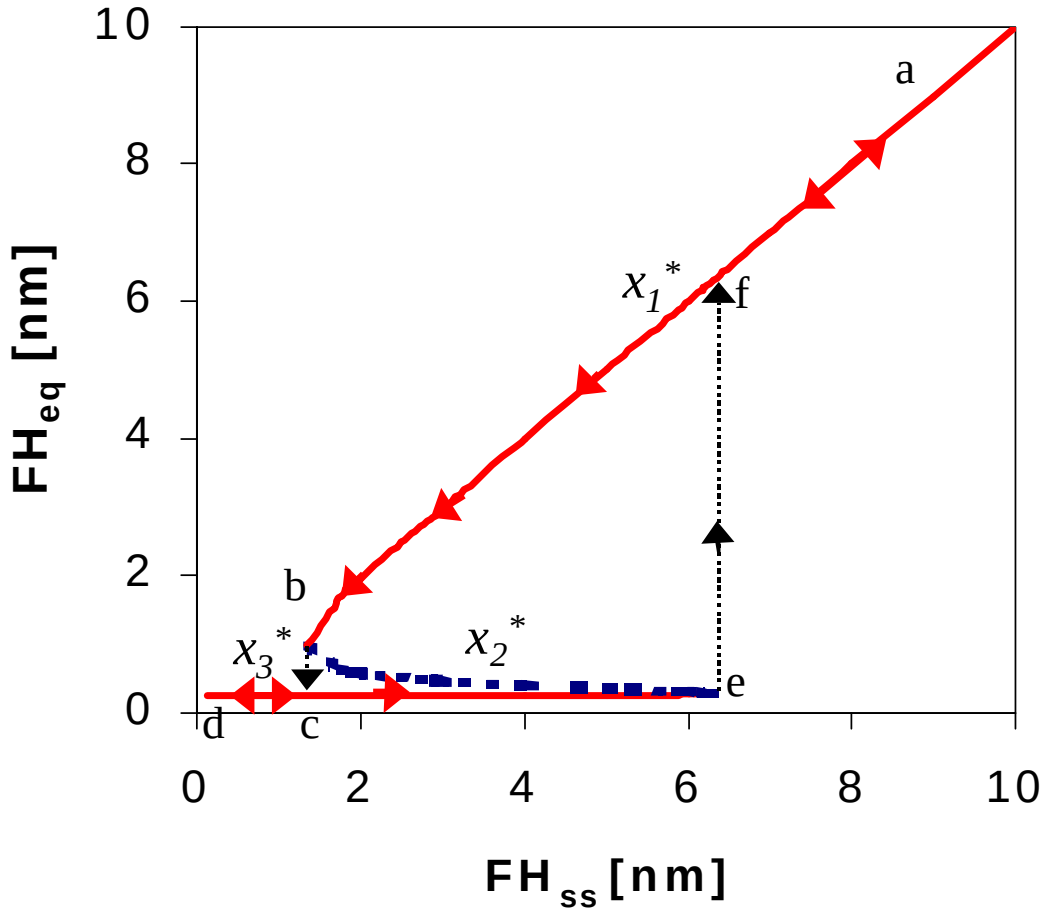

Fig. 6.14. Bifurcation plot showing FH_{eq} as a function of FH_{ss}. (–) stable, and (- -) unstable.

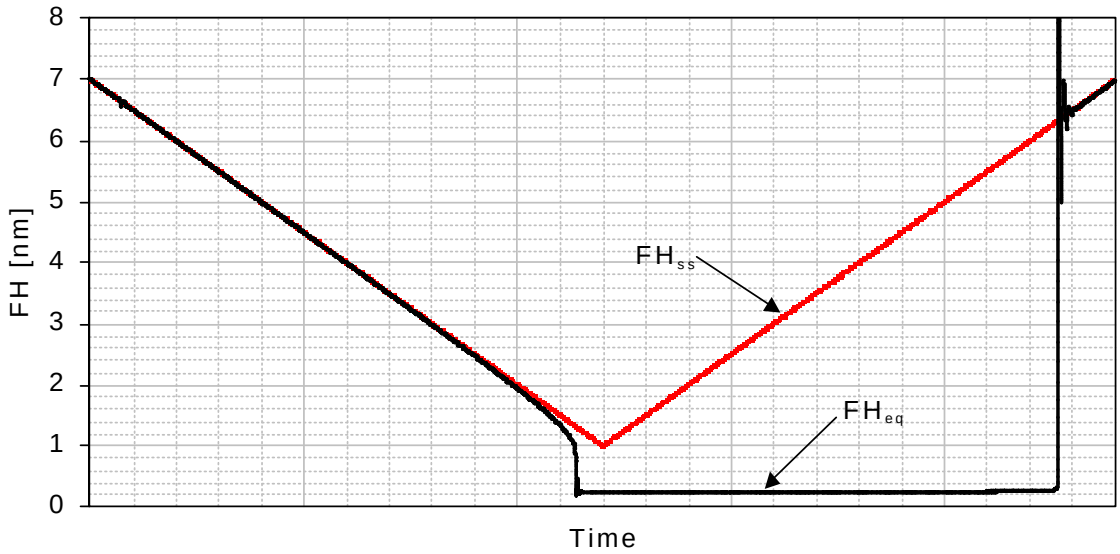

Fig. 6.15. Unforced TD – TO simulation showing the FH hysteresis is bound by the multiple equilibria regime.

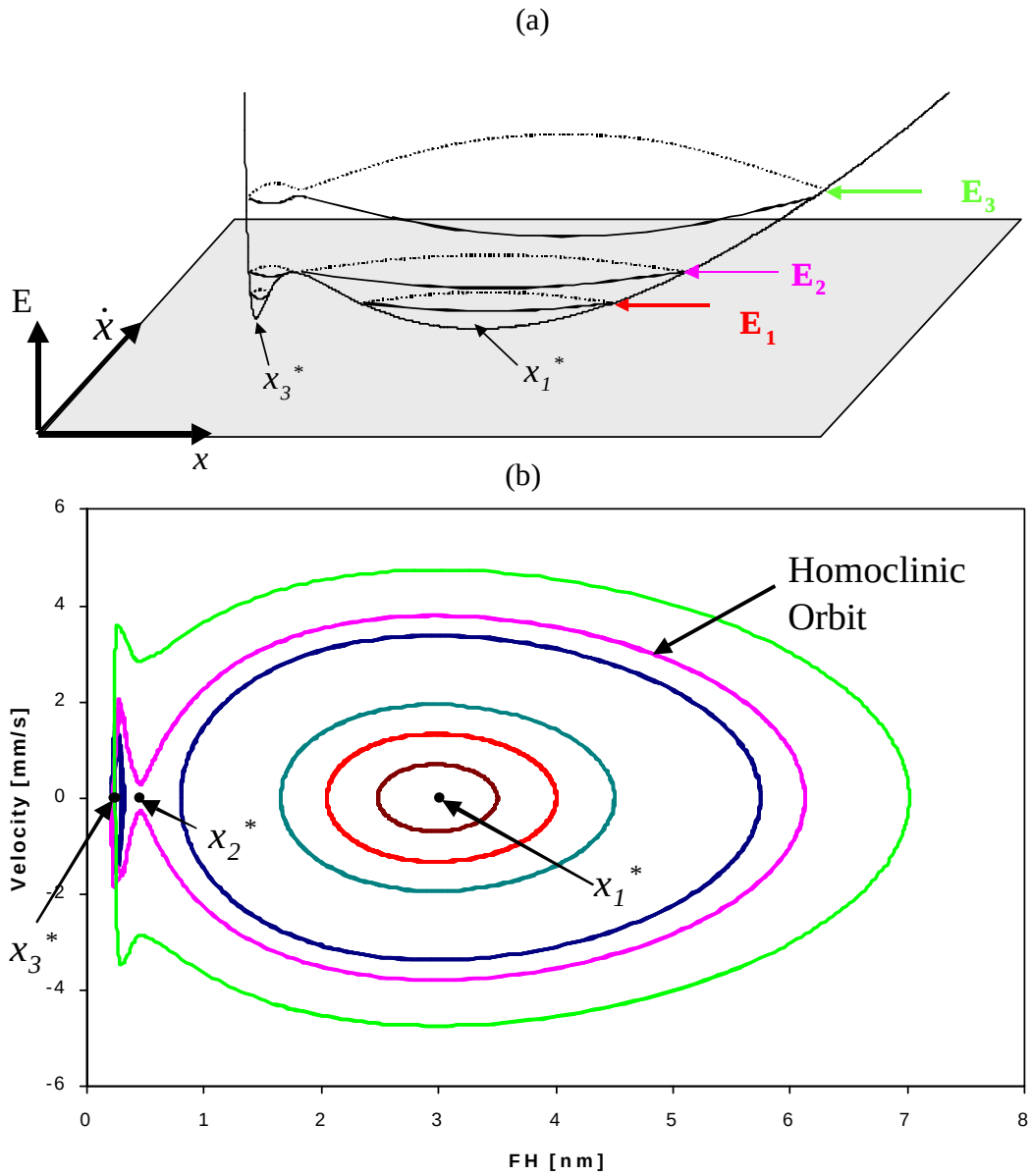

Fig. 6.16. (a) Sketch of the energy surface in state-space and (b) the trajectories projected onto the state-space plane for the unforced, undamped system.

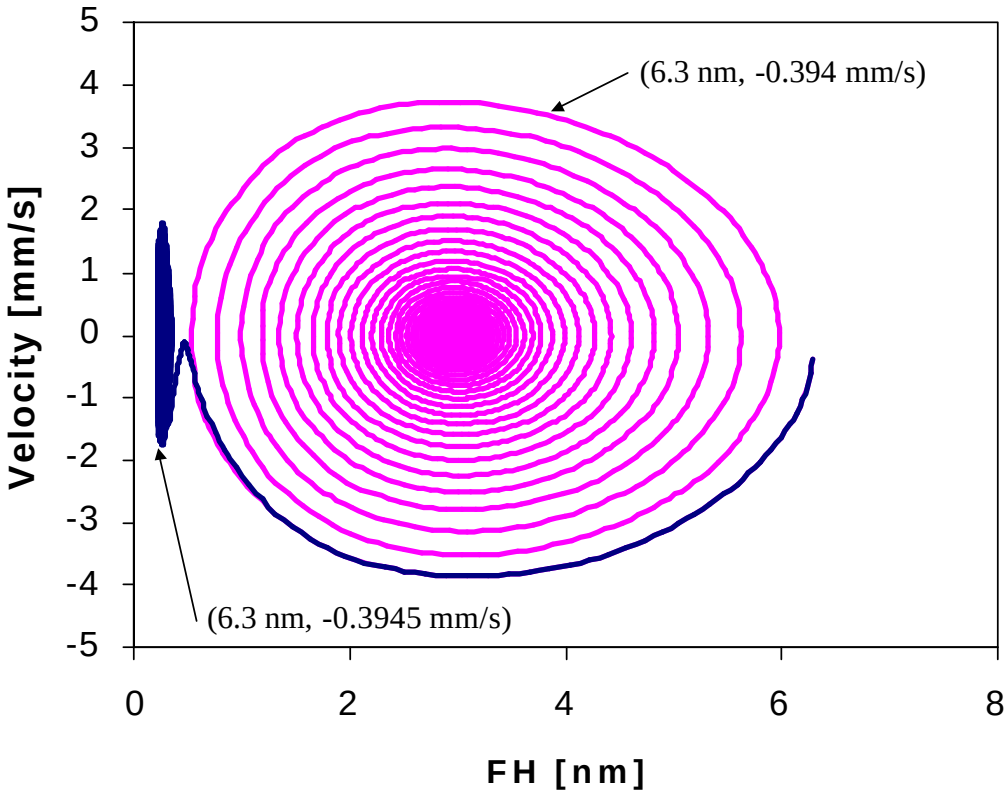

Fig. 6.17. State-space trajectories of the unforced system showing sensitivity to initial conditions.

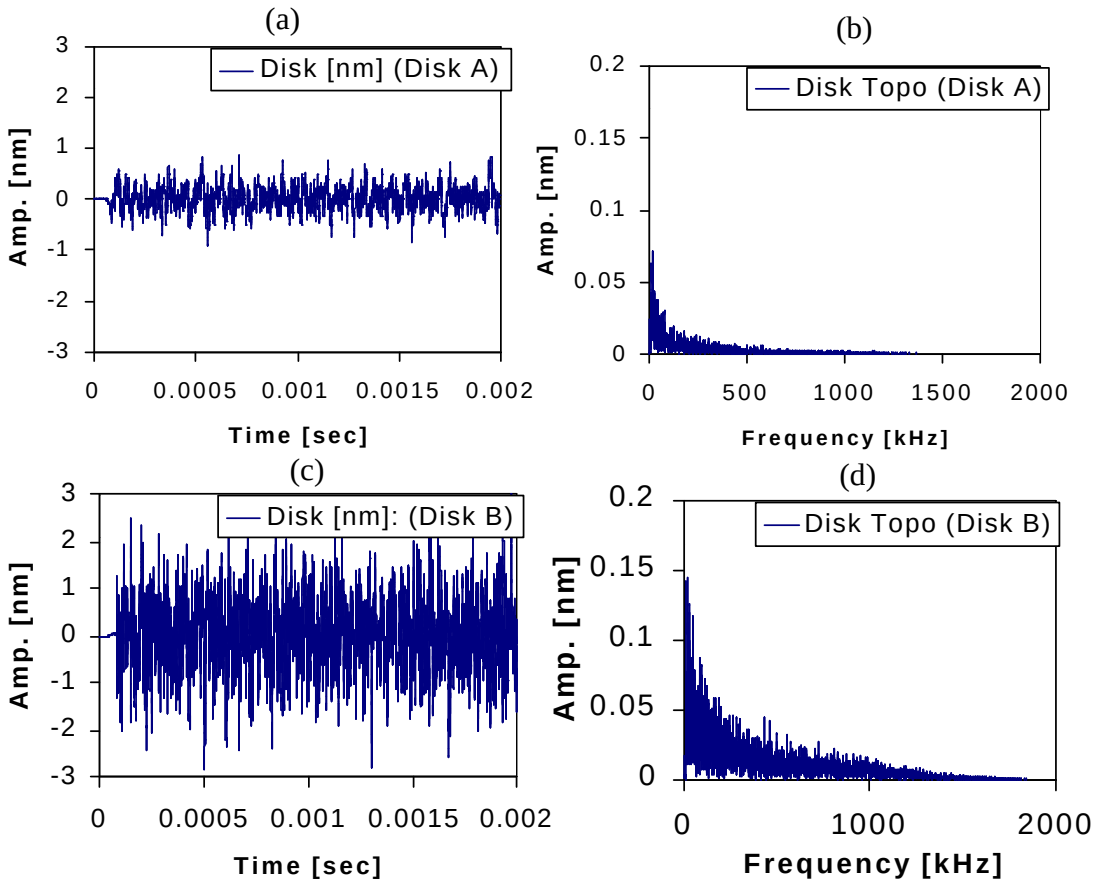

Fig. 6.18. (a) Topography of disk A and (b) its frequency content. (c) Topography of disk B and (d) its frequency content.

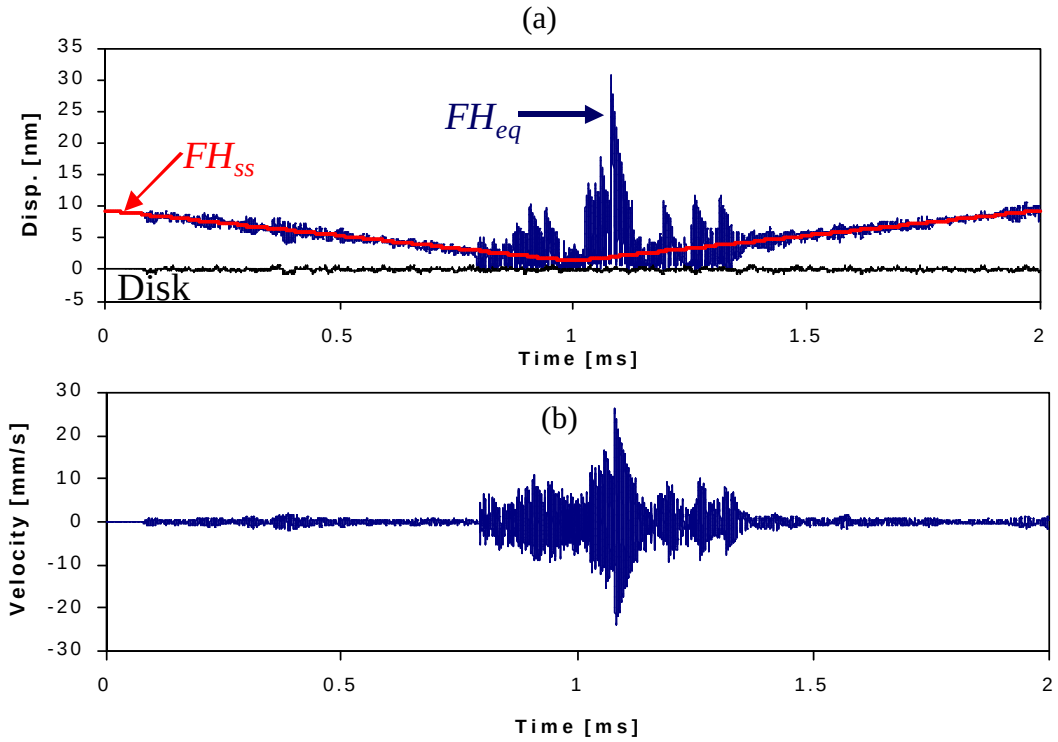

Fig. 6.19. Forced TD –TO simulation showing the (a) disk, FH_{ss} and FH_{eq} and (b) the sliders velocity as functions of time.

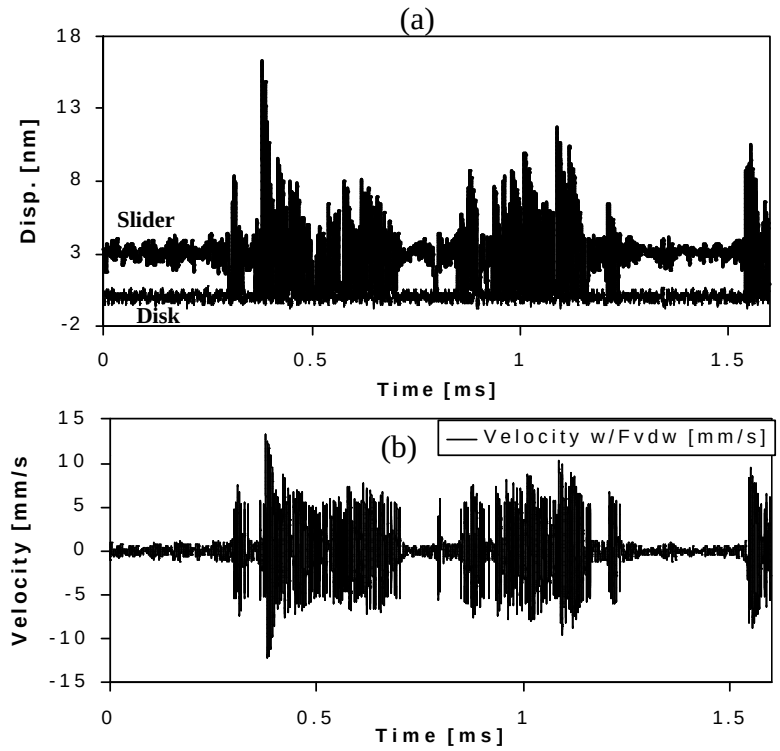

Fig 6.20. Forced constant FH_{ss} simulation showing the (a) disk and sliders displacement and (b) the sliders velocity as functions of time.

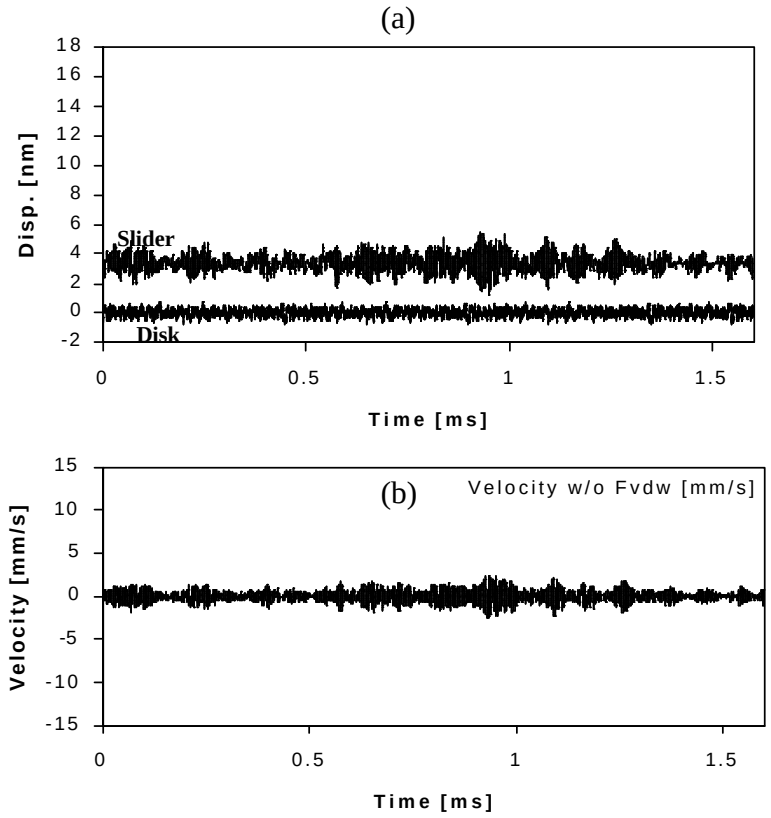

Fig. 6.21. Forced constant FH_{ss} simulation without including the intermolecular adhesion force showing the (a) disk and the sliders displacement and (b) the sliders velocity as functions of time.

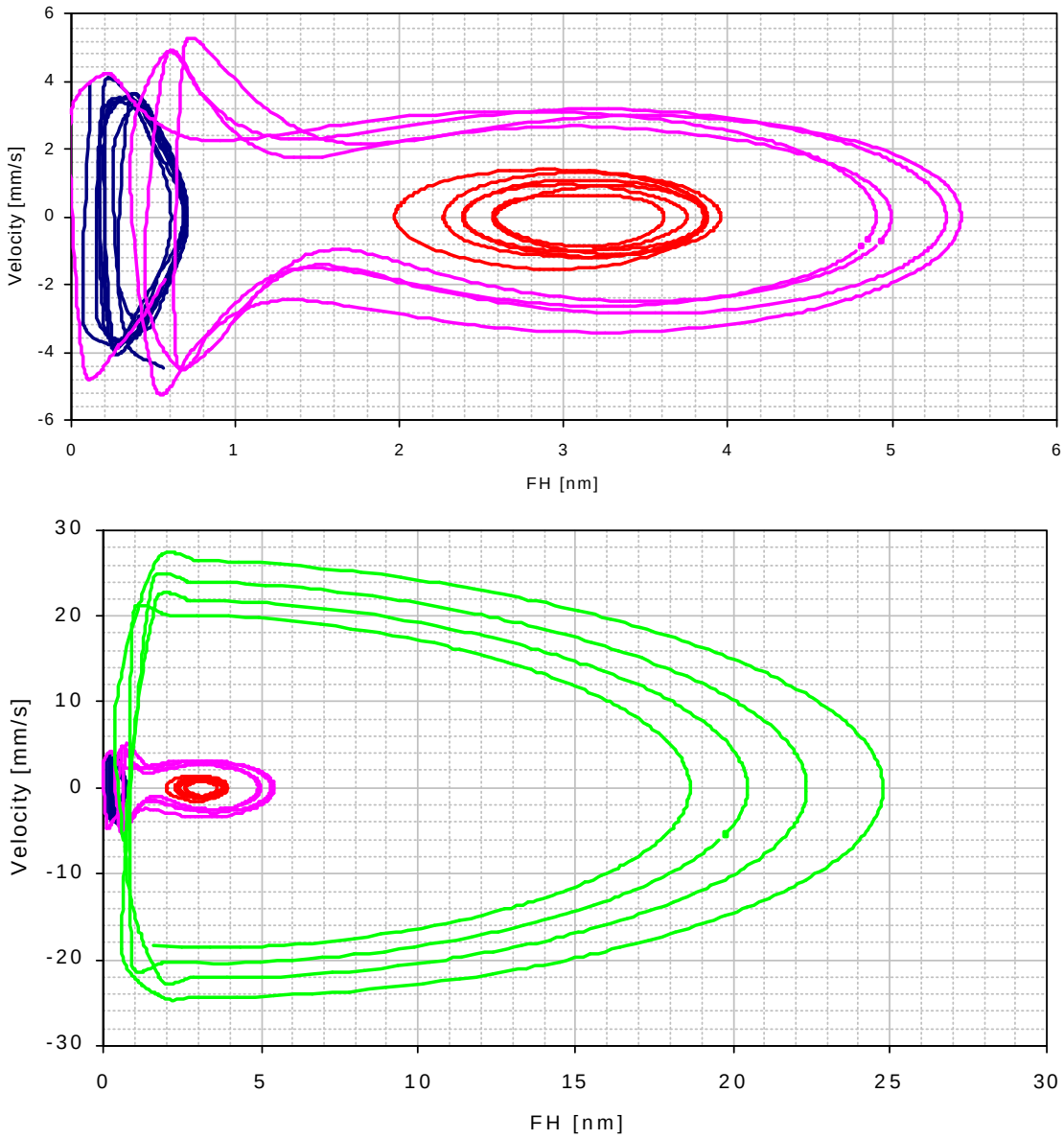

Fig. 6.22. The state-space trajectories for the forced system showing the different oscillation modes.

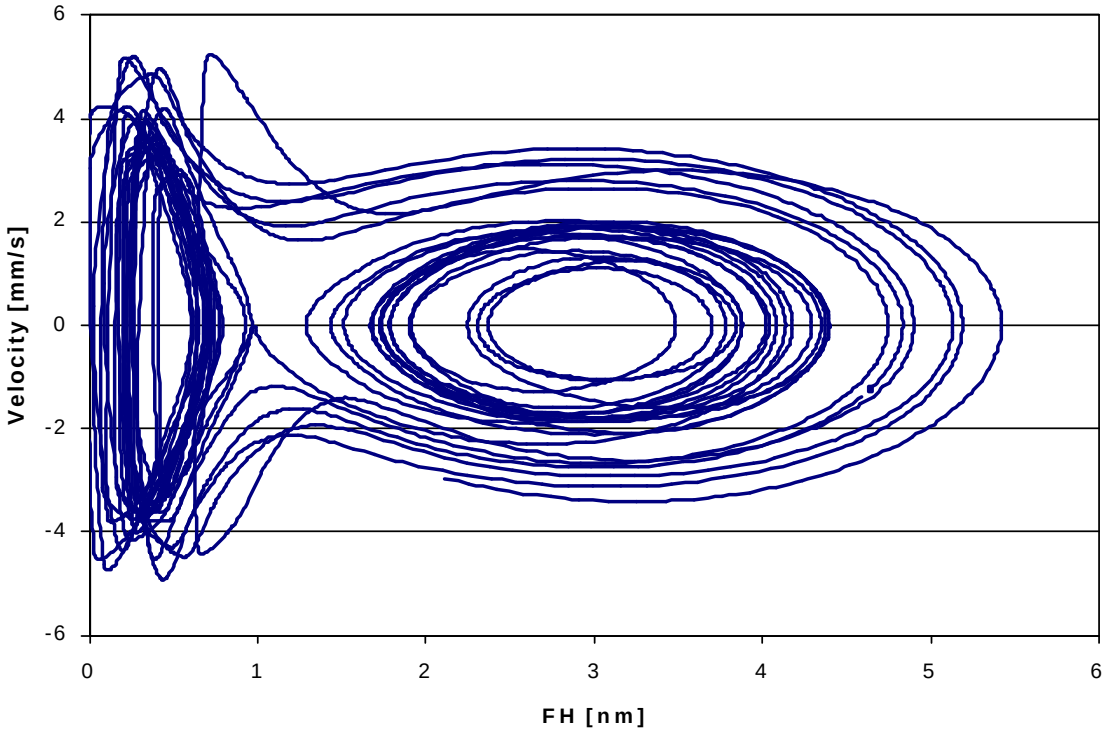

Fig. 6.23. The state-space trajectories for the forced system showing the switching between all oscillation modes randomly or chaotically.

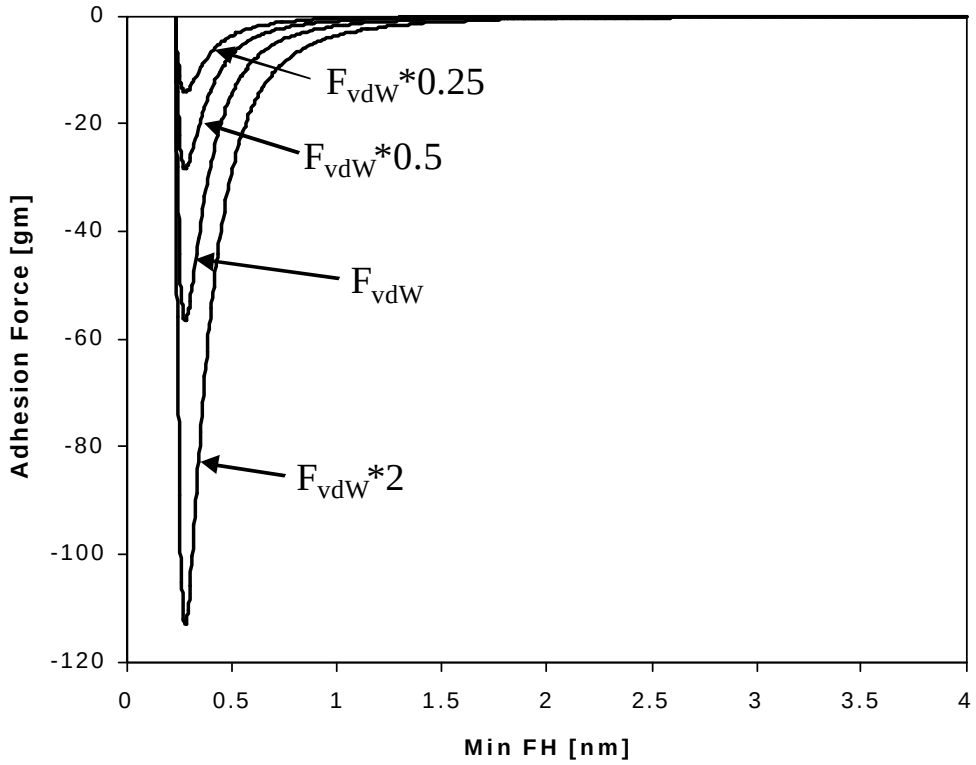

Fig. 6.24. Intermolecular adhesion forces used in the parametric study.

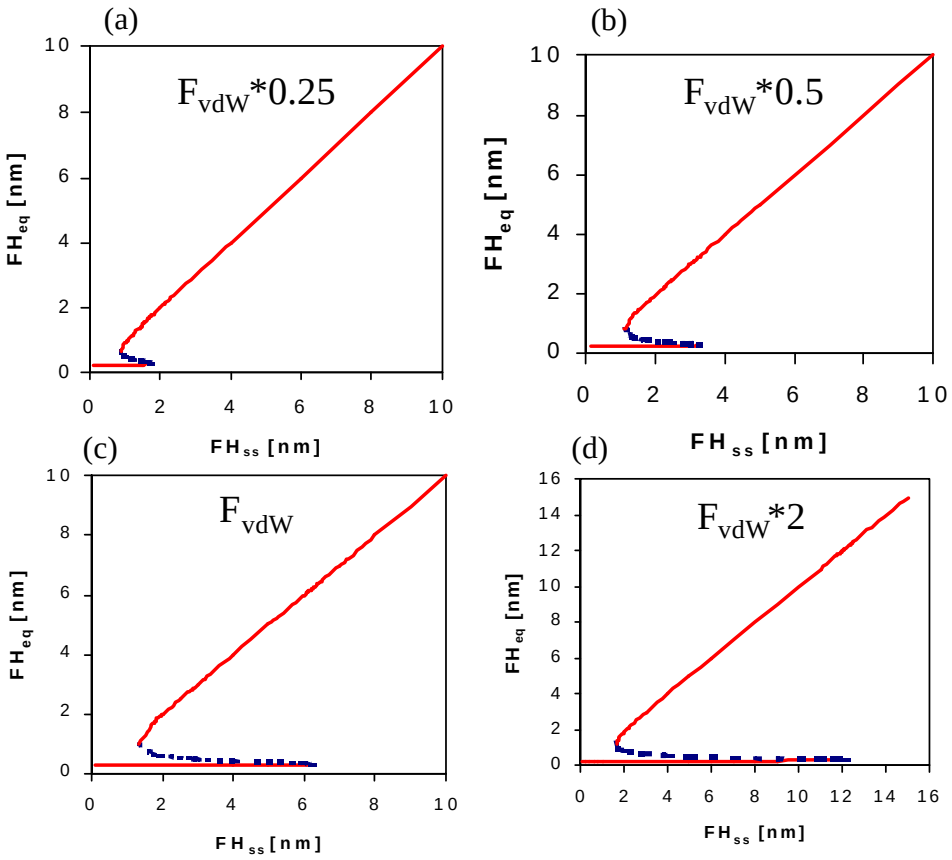

Fig. 6.25. Bifurcation plots for intermolecular adhesion forces equal to (a) F_{vdW}*0.25, (b) F_{vdW}*0.5, (c) F_{vdW}*1, and (d) F_{vdW}*2. (–) stable, and (- -) unstable.

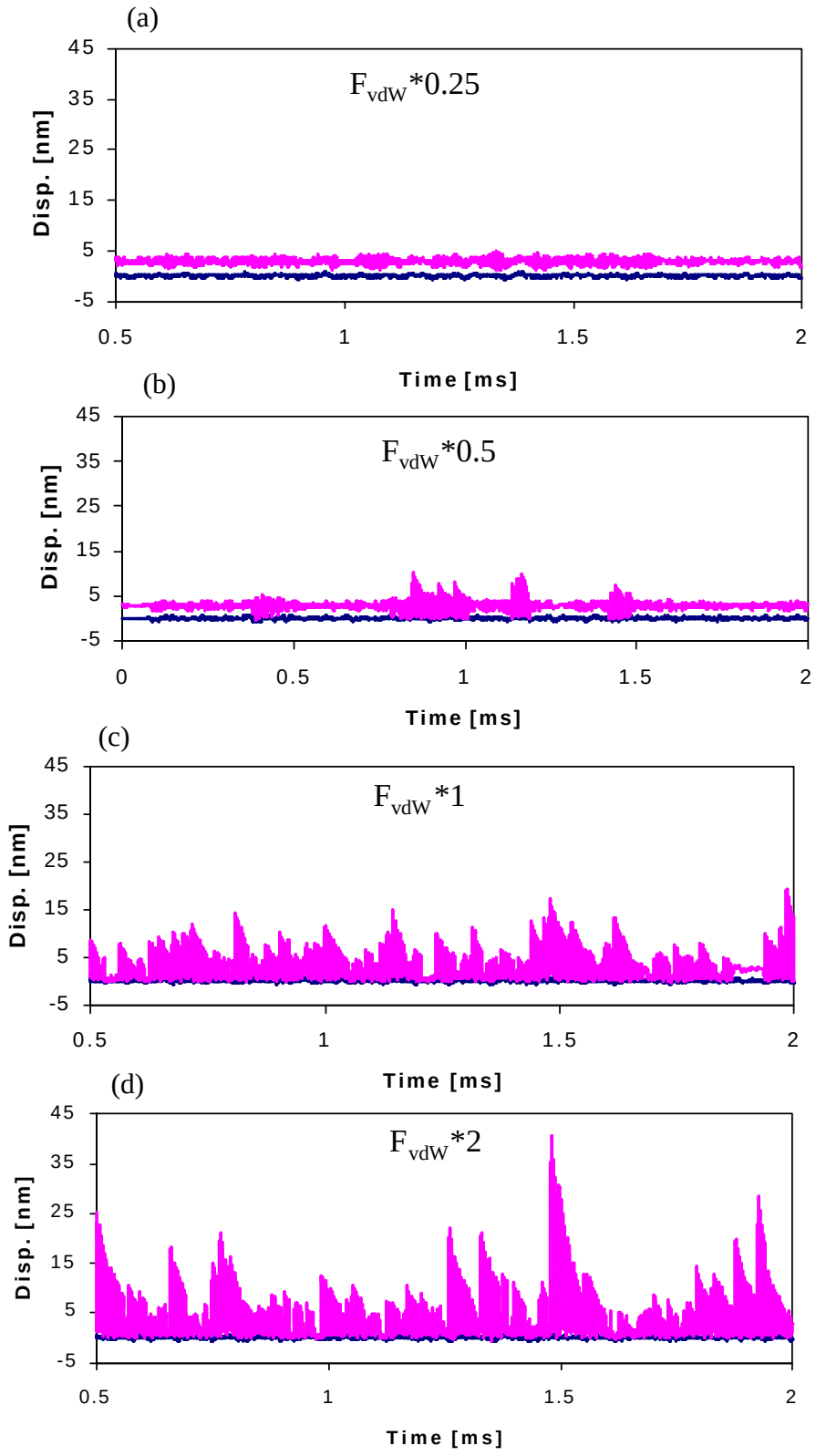

Fig. 6.26. Constant FH_{ss} simulations for intermolecular adhesion forces equal to (a) F_{vdW}*0.25, (b) F_{vdW}*0.5, (c) F_{vdW}*1, and (d) F_{vdW}*2.

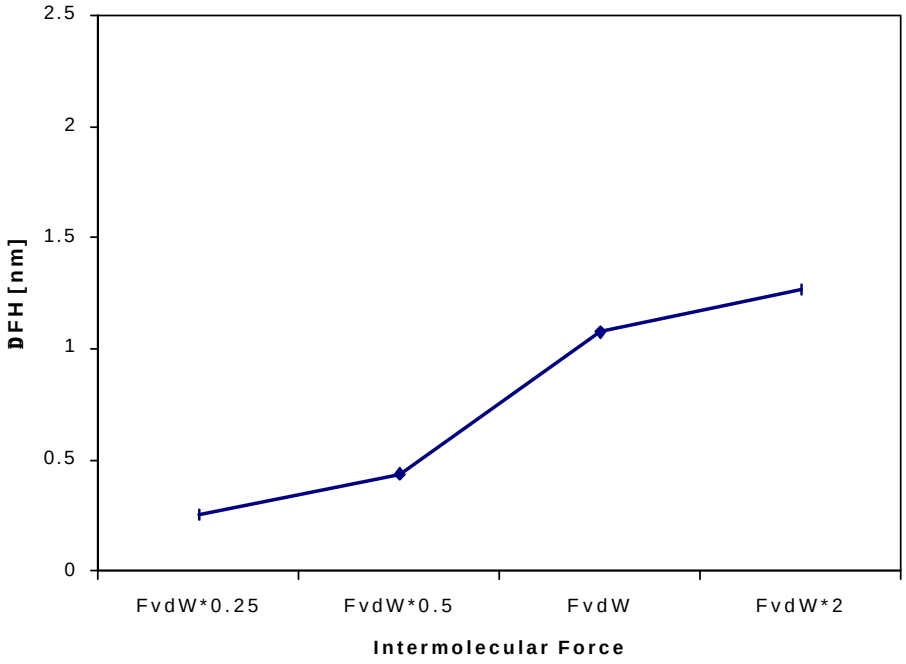

Fig. 6.27. FH hysteresis as a function of intermolecular adhesion force magnitude.

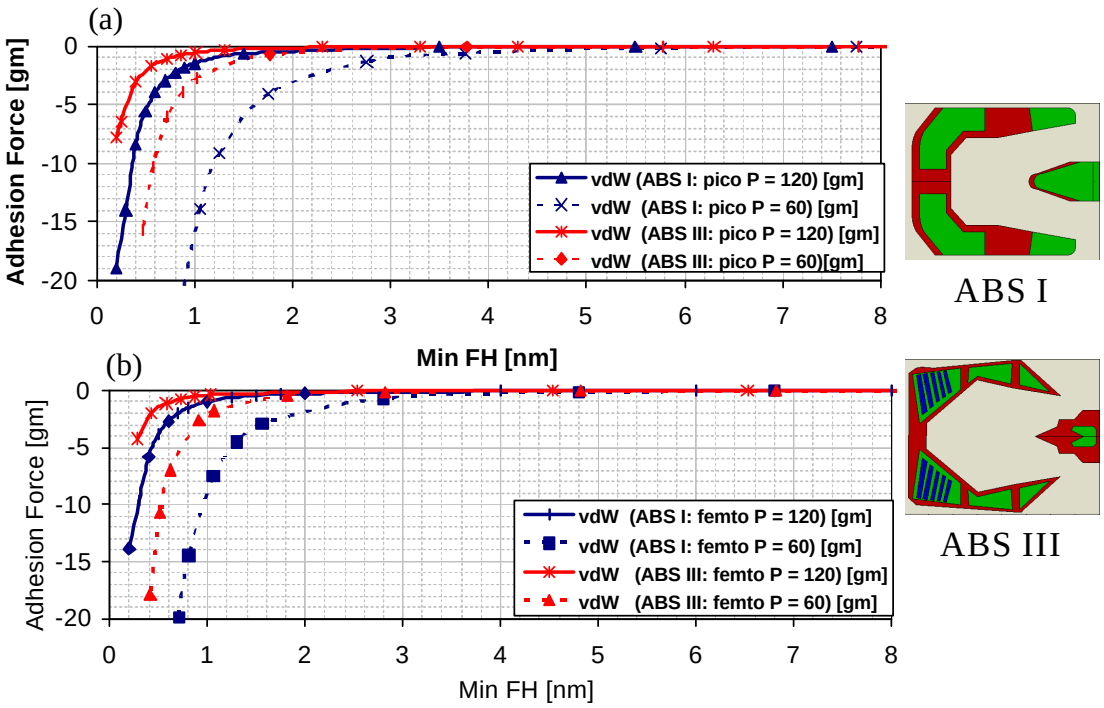

Fig. 6.28. Intermolecular adhesion force magnitude as a function of minimum spacing for (a) pico and (b) femto form-factors for two different ABS designs and two different pitch attitudes.

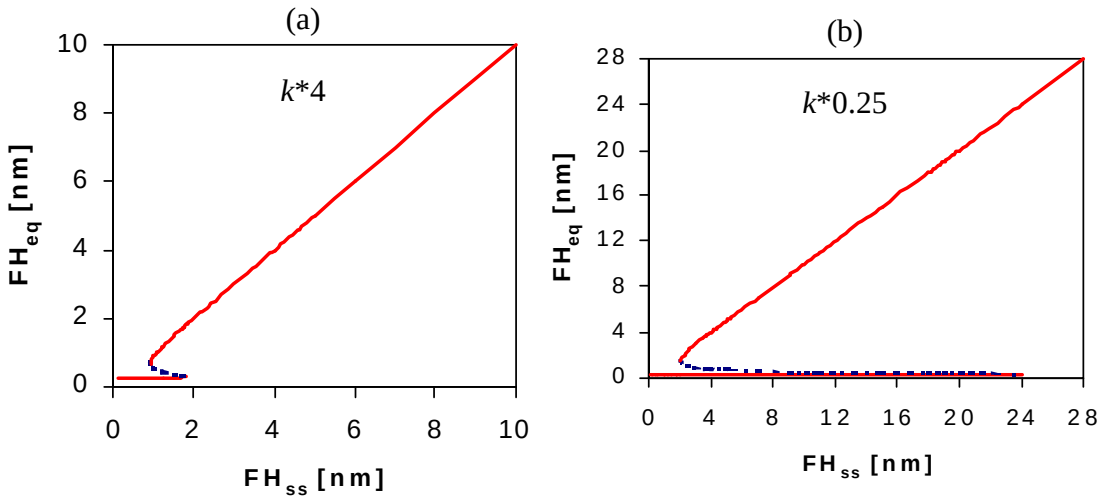

Fig. 6.29. Bifurcation plots for the nonlinear air bearing stiffness equal to (a) k*0.25, (b) k*4. (–) stable, and (- -) unstable.

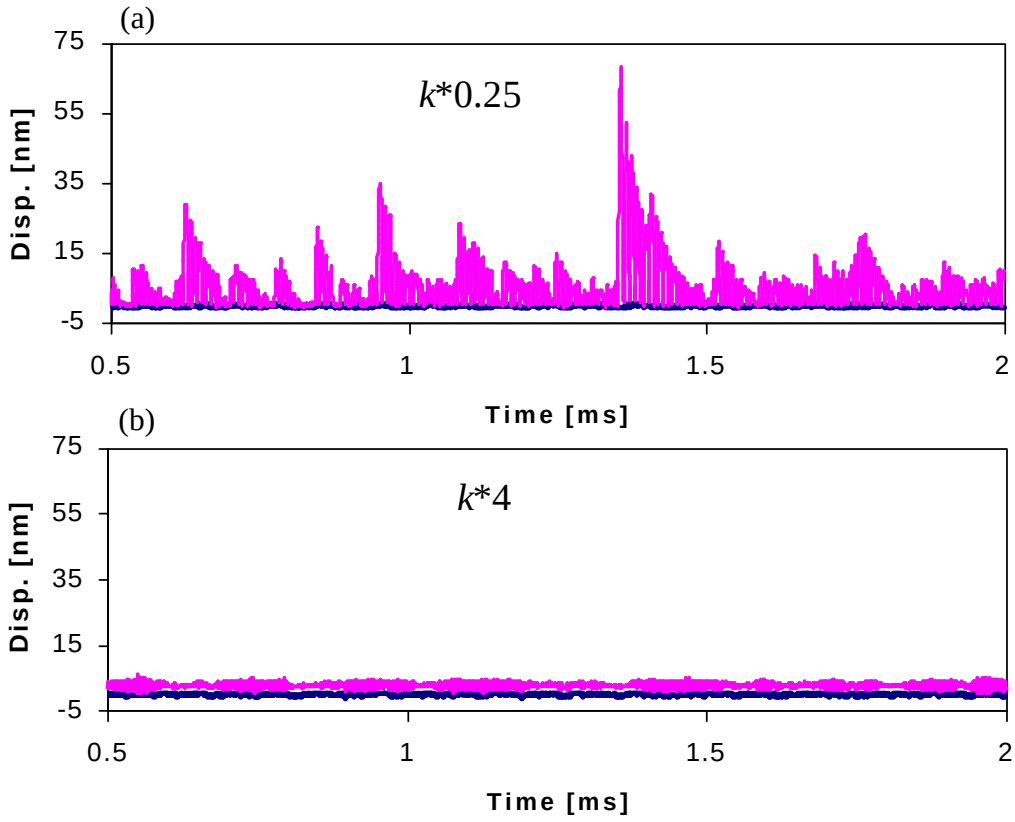

Fig. 6.30. Constant FH_{ss} simulations for the nonlinear air bearing stiffness equal to (a) k*0.25, (b) k*4.

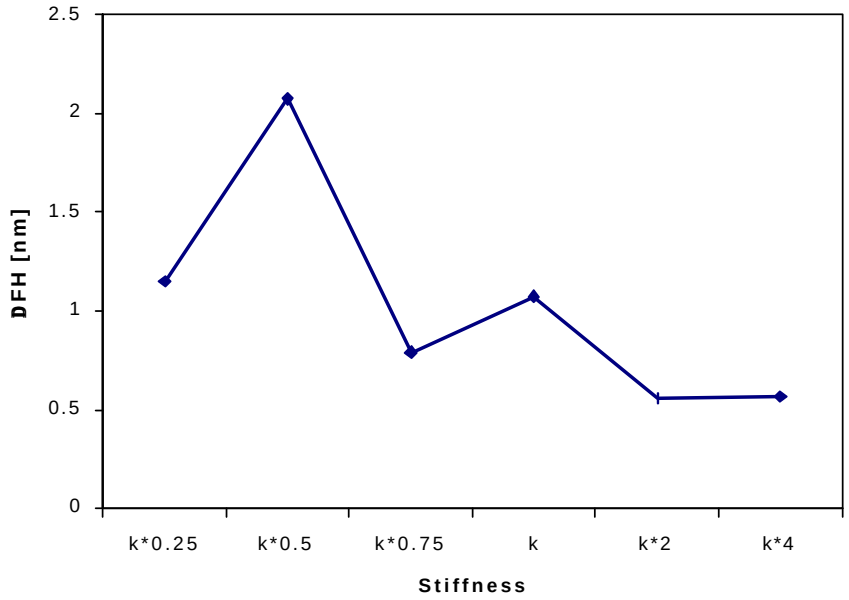

Fig. 6.31. FH hysteresis as a function of the nonlinear air bearing stiffness.

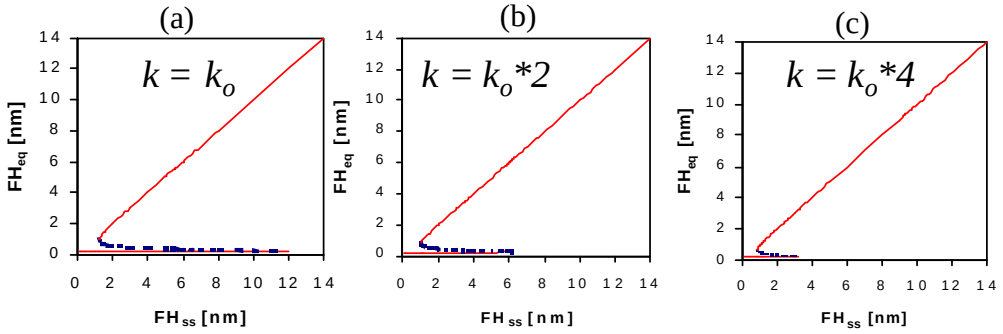

Fig. 6.32. Bifurcation plots for the linear air bearing stiffness equal to (a) k_o, (b) k_o*2 and (c) k_o*4. (–) stable, and (- -) unstable.

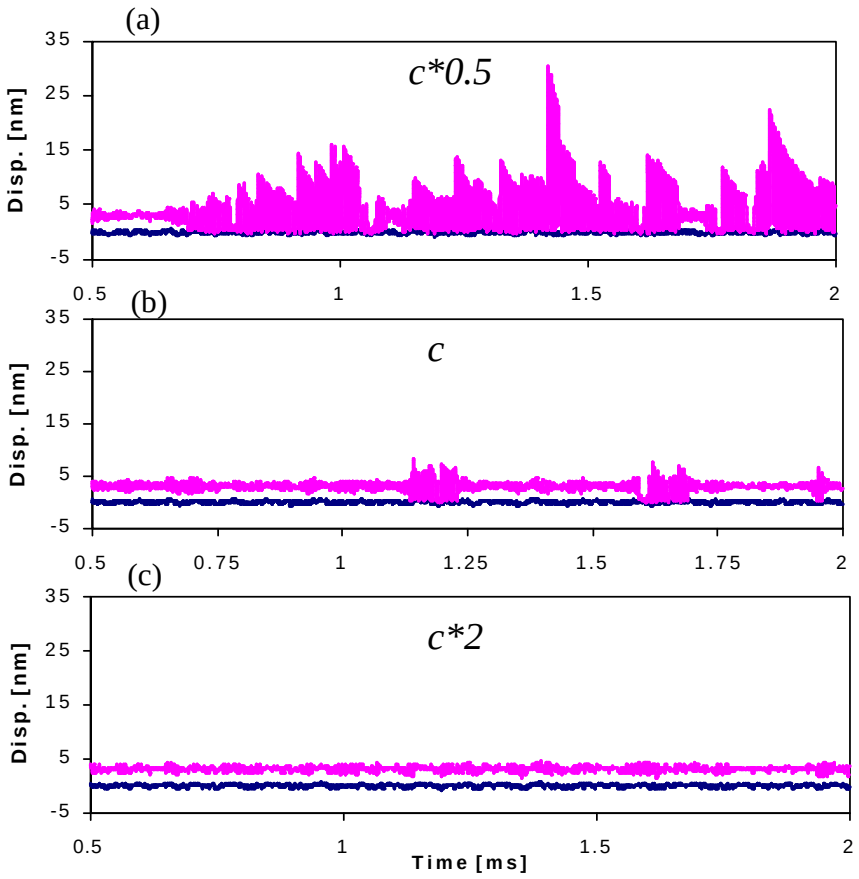

Fig. 6.33. Constant FH_{ss} simulations for air bearing damping equal to (a) *c*0.5*, (b) *c*, and (c) *c*2*.

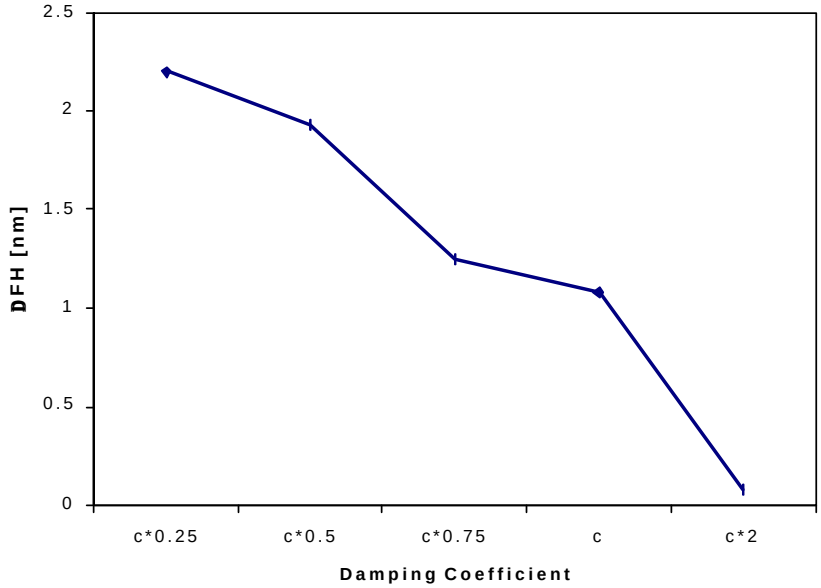

Fig. 6.34. FH hysteresis as a function of air bearing damping.

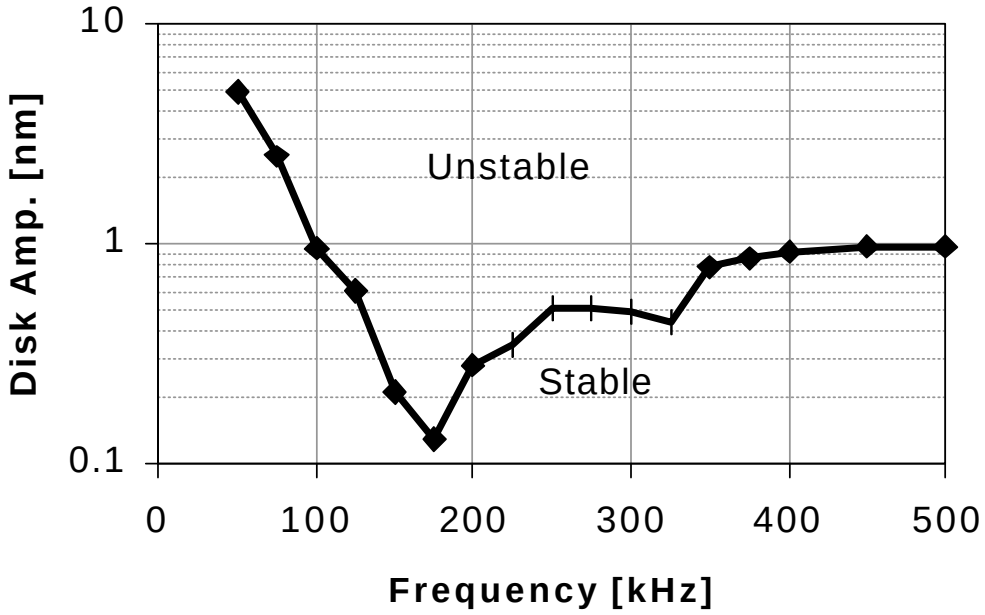

Fig. 6.35. Stable - unstable boundary for harmonic disk excitation.

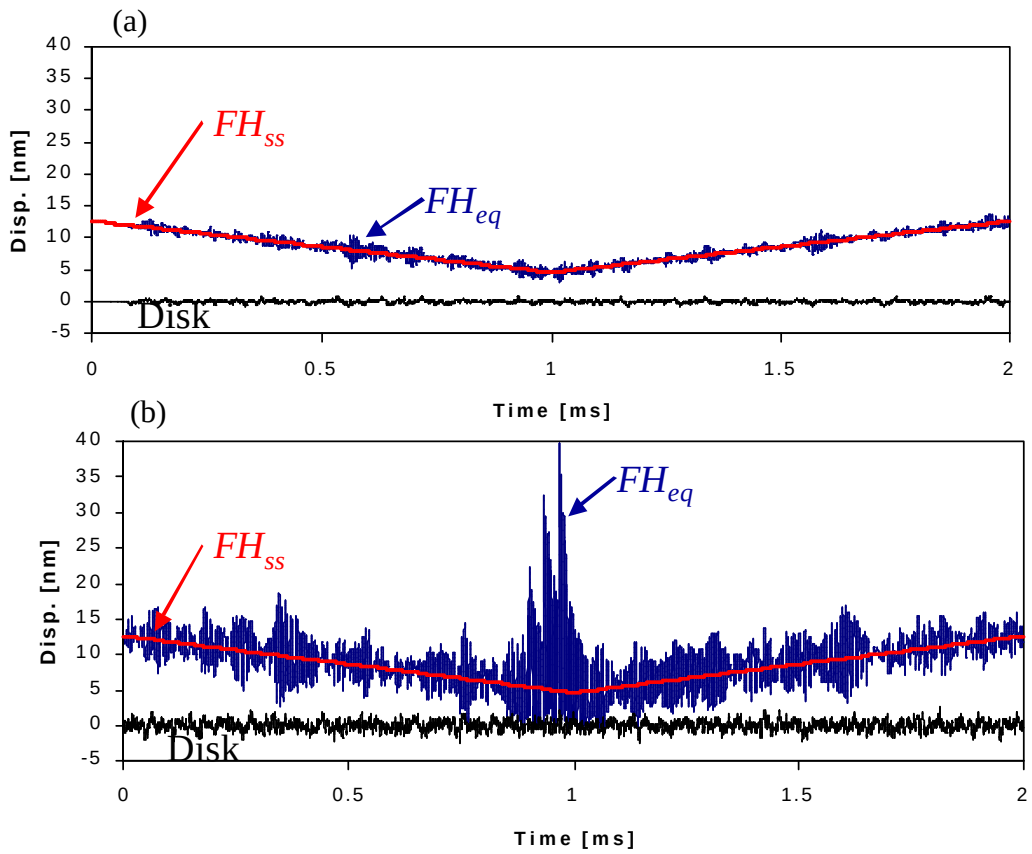

Fig. 6.36. TD-TO simulations forced by (a) disk A and (b) disk B.

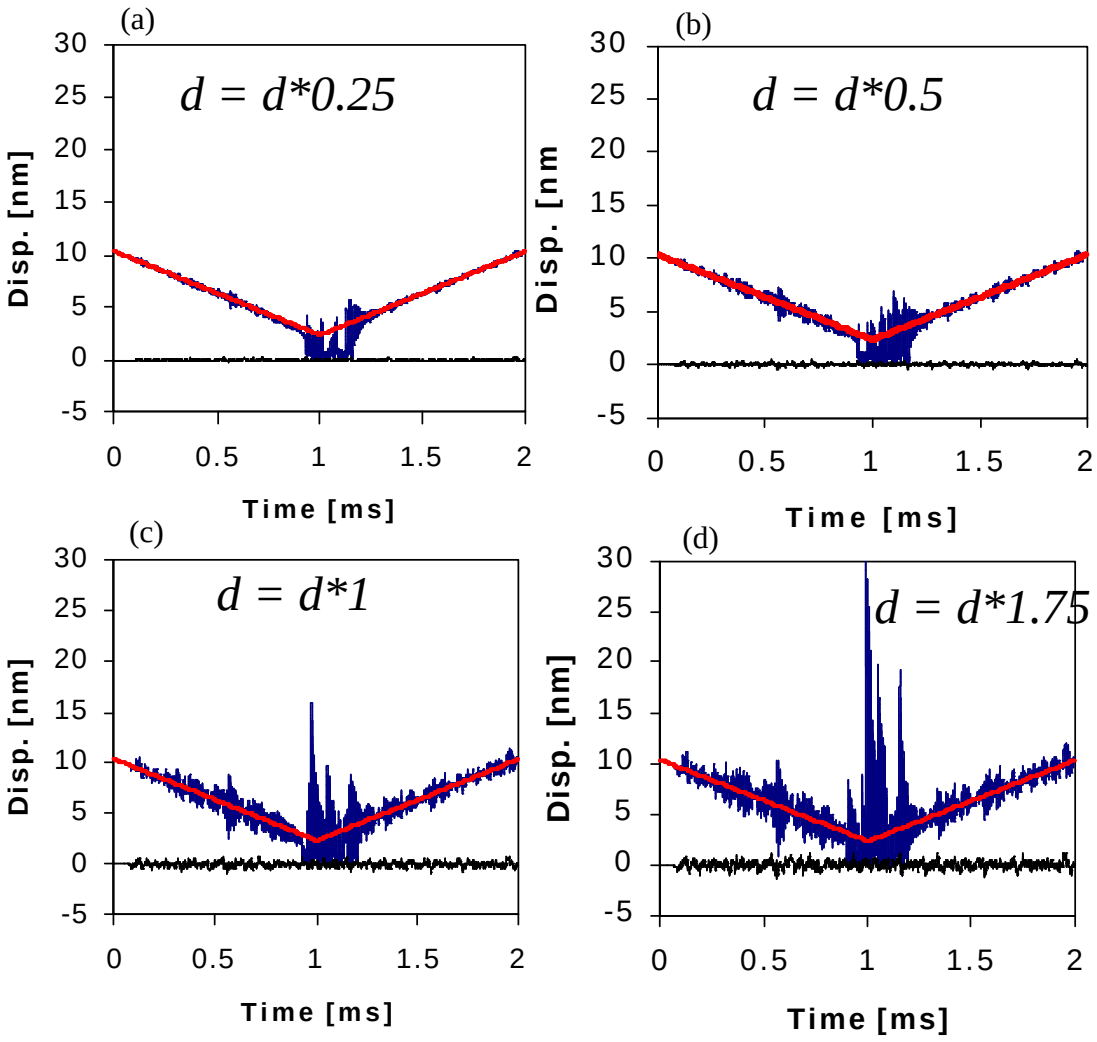

Fig. 6.37. TD – TO simulations by forcing the slider by disk A multiplied by: (a) 0.25, (b) 0.5, (c) 1, and (d) 1.75.

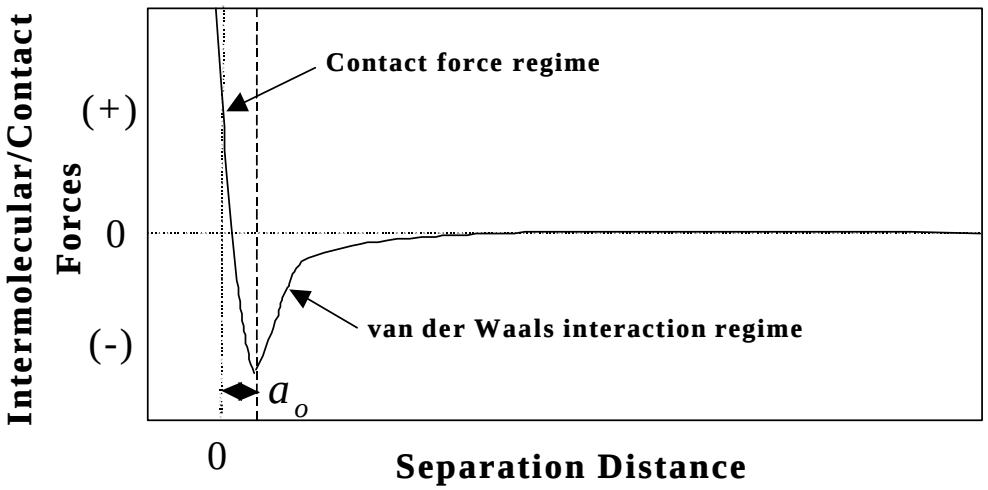

Fig. 6.38. Additional force generated by including the DMT model.

CHAPTER 7

SUMMARY AND CONCLUSIONS

Several technological challenges still remain in the pursuit of a magnetic recording areal density of 1 Tbit/in^2. One of the important challenges is obtaining a reliable HDI that is tribologically and magnetically robust with a FH of only 3.5 nm. At such an ultra-low spacing, several new phenomena at the HDI are either not currently considered or simply unknown. In achieving 1 Tbit/in^2 it is important to understand these phenomena as spacing is decreased from sub- 10 nm to sub- 5 nm. One of the concerns is how the new phenomena at the HDI affect the dynamics of the slider. Achieving and maintaining slider dynamic stability and tolerable spacing modulation (FHM) is a crucial aspect in achieving a working interface. The understanding of the new phenomena of ultra-low flying sliders can be applied to study their effects on the air bearing slider dynamics and stability. This understanding will be an integral part of realizing a HDI for 1 Tbit/in^2.

In this dissertation, the research focus is on the understanding of slider dynamics and FHM for ultra-low spacing. This dissertation is broken into two distinct sections. The first section considers a flying interface and studies the effects of new phenomena on slider dynamics and FHM. The second section is focused on stability transitions as the FH is lowered in order to achieve greater areal densities.

In Chapter 2 a new measurement system was briefly introduced to measure the slider's displacement and the disk's morphology directly under the slider with sub- nm accuracy.

This system was then used to measure the response of a sub- 10 nm FH slider flying over various disks. It was found that over the bandwidth of interest from 10 kHz to 2 MHz the slider's response while flying in steady-proximity was mostly caused by repeatable motions associated with the disk morphology. Using the measured disk topographies we obtained a direct comparison between experiment and simulation that showed excellent correlation. The FHM was analyzed using the experiments and simulations in the time and frequency domains. Three distinct frequency bandwidths were used to analyze the effect of disk morphology on FHM. Band I: 10 kHz < f < 100 kHz was the band of the geometric FHM. The geometric FHM amplitude for the particular system studied was on the same order as the disk morphology, which can be the largest contributor to FHM. The FHM in frequency Band II: 100 kHz < f < 500 kHz was influenced by the dynamics of the air bearing. If the disk morphology amplitude in Band II is low enough excitation of the air bearing does not contribute to the FHM due to the disk morphology. The FHM in frequency Band III: 500 kHz < f < 2 MHz was so low that it could be neglected compared to Bands I and II. It is obvious that a single number characterization of roughness or waviness is not sufficient to determine the quality of a disk with respect to FHM. We have shown that, for the particular slider used with disk C, the FHM amplitude is on the order of the disk morphology. However, optimization can be achieved with both the ABS design and the disk morphology to obtain an even lower FHM. A case study measuring FHM of 10 different disks manufactured for sub- 20 nm interfaces was carried out revealing that a majority of the disks exhibited excessive FHM. Also, with the correlation realized here between experiment and simulation, simulations can now be used as a

design tool. New ABS designs can be modeled and simulated for FHM due to disk morphology prior to manufacturing.

From Chapter 2, it was found that even for a well behaved HDI, the FHM is on the same order as the disk morphology. Since the amplitude of the disk morphology exponentially decays as frequency increases, the geometric FHM becomes the largest contributor to FHM. In Chapter 3 we extensively studied the cause of the geometric FHM with pico and femto form-factor designs.

The expectation was that the femto slider should have less FHM than the pico slider, because it has long been known that for wavelengths somewhat larger than the slider length, the FHM is proportional to the square of the length of the slider. It was found that this was indeed the case for wavelengths longer than the slider, but when the wavelength was reduced to about the slider's length the FHM of the femto slider was much greater than that of the pico slider. After examining the characteristics of the sliders it was found that the primary reason for the large FHM of the femto slider was its low pitch, which caused its pressure support points to be at the trailing edges of the side rails, about 0.15 mm forward of the transducer. It was also observed that the large FHM results from a phase shift between the slider's response and the disk waviness, which is itself a result of the low pitch and forward pressure points. The phenomenon occurred for both the femto slider and the pico slider.

In comparing redesigned pico and femto sliders with the same target FH and comparable pitch, we showed that the pico slider has roughly twice the FHM in the 6 mm to 1.5 mm waviness range. However, for waviness between 1.5 mm to 0.156 mm both the pico and femto sliders have similar high levels of FHM due to their similarities in ABS designs (i.e. pressure distribution). We concluded that a femto design has lower FHM due to disk waviness for wavelengths greater than 1.5 mm. However, for waviness wavelengths below 1.5 mm and above the dynamic resonant modes of the air bearing, FHM is not primarily a function of the sliders overall length but is more a function of sliders' attitude and the ABS design. It is possible to predict FHM due to this geometric effect by considering only the disk morphology. A new femto slider design was introduced for minimizing the geometric FHM with the findings in this chapter taken into account. Results showed an 83% decrease in FHM when compared to the original femto slider design. Therefore, these results can be used in designing better ABS's and disks for ultra-low FH sliders. In order to decrease FHM due to disk waviness for wavelengths below 1.5 mm, attention needs to be focused on slider attitude, ABS design, and disk morphology.

In Chapter 3, results were presented for both pico and femto sliders, however, the focus was on understanding the cause and minimizing geometric FHM. In Chapter 4 we performed a direct comparison of the performance of air bearing slider form-factors, namely femto and pico size sliders. We found that the smaller form-factor exhibited an overall enhancement in performance when the ABS was properly designed. A beneficial increase in damping ratios and a detrimental decrease in modal stiffnesses was observed

when simply scaling the form-factor from pico to femto. However, it was seen that if the ABS is designed to retain a larger percentage of its bearing load capacity and maintain high peak pressure(s), the stiffness is not compromised dramatically by scaling down the form-factor. Also, a large number of transverse pressure gradients are extremely effective in increasing damping, and they further increase damping when the form-factor is scaled from pico to femto.

It was previously believed that geometric FHM was solely caused by the form-factor and was proportional to the square of the slider body length. However, we found that the FHM due to geometry is composed of the superposition of two effects dependent on the overall length of the slider for long disk waviness wavelengths and dependent on the ABS design for shorter disk waviness wavelengths. For long waviness wavelengths, FHM was shown to be dependent on the sliders body length: proportional to $L^{2.6}$ and L^{4} for ABS I and ABS II, respectively. For shorter waviness wavelengths, FHM was shown to be dependent on the ABS design and a phase shift between the slider's response at the transducer and the disk as well as an amplitude change in the slider's displacement. These two effects are demarked by a transition disk waviness wavelength of approximately 3 mm. By comparing femto to pico form-factors, it is seen that the femto exhibited lower FHM for waviness wavelengths greater than the slider's body length, however, it demonstrated similar levels of FHM for waviness wavelengths less than the slider's body length. By cross comparing ABS designs, it was found that significant improvements in FHM performance can also be attained by changing the ABS design and not decreasing the form factor. Simulations were performed using an actual measured

disk topography which showed a decrease of 22 % to 32 % in FHM by scaling down the form-factor from pico to femto. However, by cross-comparing ABS designs, we found that ABS II exhibited much less FHM even in comparing ABS II in the pico form-factor to ABS I in the femto form-factor. It is concluded that by simply scaling down the form-factor, enhanced performance is not always attained. However if special care is taken in the design of the ABS in order to maintain stiffness, increase damping and decrease geometric FHM, major improvements can be realized. Ultimately, to achieve the greatest performance, a smaller form-factor should be used with special care taken in the ABS design.

As the FH is lowered, a slider's behavior as described above changes drastically. What has been described in Chapters 2 – 4 are the dynamics associated with steady-proximity or a flying slider. However, once the spacing becomes extremely small, unsteady-proximity behavior occurs that cannot be describe by the analysis thus far. In Chapter 5, the nature of the unsteady-proximity behavior was studied. The findings presented suggest that the non-linearities of the air bearing slider system cannot be ignored for sub-5 nm FH sliders and must be considered when modeling slider-disk interface dynamics. When a slider is within proximity of a disk the complexities of the slider's response can be explained by the non-stationary response, and FFT analysis becomes an inadequate means for frequency domain analysis. A method such as JTFA must be used to accurately analyze the non-linear, non-stationary response of a slider when it is in the state of unsteady-proximity. Contact between the slider and disk can cause complexities of the slider's response due to the additional boundary conditions when viewed in the frequency

domain, however, it is seen that contact is not a necessary condition for producing this phenomenon.

Experimentally it is observed that as a slider flies within proximity of the disk, HDI dynamic stability is lost and the interface becomes unsteady. The nature of this response under unsteady-proximity was studied in Chapter 5, however the cause was not addressed there. In Chapter 6 we considered additional interfacial forces due to the close proximity of the slider and disk.

Additional forces due to capillary and intermolecular adhesion were considered. Due to the kinetic formation of a meniscus and the experimental results presented, we concluded that meniscus forces need not be considered in the dynamic modeling of the HDI. A nonlinear dynamic analysis of a modeled HDI incorporating intermolecular forces revealed a new kind of dynamics that cannot be captured by static analysis. By analyzing the systems equilibria and stability it was found that multiple equilibria exist in the sub – 6 nm FH regime associated with a double-well potential. Within this regime the slider's motion can be stable or chaotically unstable when it is externally forced by a disk topography. From the analytical and numerical analysis presented, the experimentally measured FH hysteresis, the intermittent slider instability and the abrupt transition between stable and unstable proximity can be explained. A parametric study was used to show how the variables affect HDI stability. Also, the effect of the power-hardening air bearing stiffness was shown to be beneficial in increasing HDI stability. By optimizing the parameters such as the air bearing design and the disk morphology we can improve

the stability of the HDI. However, for practical values of the parameters, it is found that instability is likely to occur when flying below 6 nm. From these results, we are forced to conclude that there may be a fundamental lower FH limit for a give slider – disk combination, below which the slider would not be able to fly with a controlled FH due to HDI dynamic instability caused by intermolecular adhesion forces.

This dissertation describes the dynamics associated with ultra-low flying sliders over a broad range from steady to unsteady proximity. Based on the research presented, we conclude that achieving the spacing requirement for 1 Tbit/in^2 will not be a simple matter. The topics covered here are by no means the only phenomena associated with the HDI, however, these findings can be directly applied to increase the feasibility, stability, and reliability of the HDI in future hard disk drives.

REFERENCES

[1] Seagate website, http://www.seagate.com/newsinfo/images/downloads/Barracuda36ES.jpg.

[2] Hutchinson Technologies website, http://www.htch.com/primer.asp.

[3] IBM Corporation website, http://www.almaden.ibm.com/sst.

[4] Read-Rite Corporation website, http://www.readrite.com/html/whatnew/topgun.html.

[5] Information Storage Industry Consortium (INSIC) website, http://insic.org.

[6] C. D. Mee and E. D. Daniel, *Magnetic Recording Handbook: Technology & Applications*, United States of America, McGraw-Hill, 1990.

[7] R. Wood, "The Feasibility of Magnetic Recording at 1 Terabit per Square Inch," *IEEE Transactions on Magnetics*, Vol. 36, no. 1, pp. 36-42, Jan. 200.

[8] Hitachi Global Storage Technologies website, http://www.hgst.com/hdd/research/storage/hdi/interaction.html.

[9] Q .H. Zeng, B. H. Thornton, D. B. Bogy, and C. S. Bhatia, "Flyability and Flying Height Modulation Measurement of Sliders with Sub-10nm Flying Heights," IEEE Trans. on Mag., Vol. 37, No.2, pp. 894-899, March 2001.

[10] B. H. Thornton, A. Nayak, and D. B. Bogy, "Flying Height Modulation Due to Disk Waviness of Sub-5nm Flying Height Air Bearing Sliders," *ASME J. of Tribology*, Vol. 124, pp. 762-770, Oct. 2002.

[11] T. Pitchford, "Head/Disk Interace Tribology Measurements for 100Gb/in^2," *Proceedings of the Symposium on Interface Technology Towards 100 Gbit/in^2*, ASME, TRIB-Vol. 9, pp. 83-90, 1999.

[12] A. Menon, "Critical Requirements for 100Gb/in^2 Head/Media Interface," *Proceedings of the Symposium on Interface Technology Towards 100 Gbit/in^2*, ASME, TRIB-Vol. 9, pp. 1-9, 1999.

[13] A. Menon, "Interface Tribology for 100 Gb/in^2," *Tribology International*, Vol. 33, pp. 299-308, 2000.

[14] L. -Y. Zhu and D. B. Bogy, "Head-Disk Spacing Fluctuation due to Disk Topography in Magnetic Recording Hard Disk Files," *Tribology and Mechanics*

of Magnetic Storage Systems, STLE Special Publication, SP-26, pp. 160-167, 1989.

[15] W. Yao, D. Kuo, and J. Gui, "Effects of Disc Micro-Waviness in an Ultra-high Density Magnetic Recording System", *Proc. Of the Symposium on Interface Technology Toward 100 Gbit/in^2*, ASME, pp. 31-37, 1999.

[16] B. H. Thornton, D. B. Bogy, and C. S. Bhatia, "The Effects of Disk Morphology on Flying Height Modulation: Experiment and Simulation," *IEEE Transactions on Magnetics*, Vol. 38, no. 1, pp.107-111, Jan. 2002.

[17] Q. H. Zeng and D. B. Bogy, "Stiffness and Damping Evaluation of Air Bearing Sliders and New Designs with High Damping", *ASME J. Tribology*, Vol. 121, pp. 341-347, April 1999.

[18] Y. Hu and D. B. Bogy, "Flying Characteristics of a Slider over Textured Surface Disks," *IEEE Transactions on Magnetics*, Vol. 33, no. 5, pp. 3196-3198, Sept. 1997.

[19] J. W. White, "The Transverse Pressure Contour Slider: Flying Characteristics and Comparisons with Taper-Flat and Cross-Cut Type Sliders," *Advances in Information Storage Systems*, Vol. 3, pp. 1-14, 1991.

[20] J. W. White, "Dynamic Response of the Transverse Pressure Contour Slider," *Tribology and Mechanics of Magnetic Storage Systems, STLE Special Publication*, SP-22, pp. 72-82, 1987.

[21] H. Tanaka, S. Yonemura, and H. Tokisue, "Slider Dynamics During Continuous Contact with Textured and Smooth Disks in Ultra Low Flying Height," *IEEE Transactions on Magnetics*, Vol. 37, no. 2, pp. 906-911, March 2001.

[22] J. C. Harrison, K. J. Altshuler, and C. M. Huynh, "An explanation of the observed frequency domain behavior of head-disk interface resonances in the proximity recording regime," *IEEE Trans. Magn.*, vol. 35, pp. 933-938, Mar., 1999.

[23] B. Knigge, and F. E. Talke, "Dynamics of transient events at the head/disk interface," *Tribology International*, vol. 34, pp. 453-460, July, 2001.

[24] B. Knigge, and F. E. Talke, "Slider vibration analysis at contact using time-frequency analysis and wavelet transforms," *ASME J. of Tribology*, vol. 123, pp. 548-554, July, 2001.

[25] A. K. Menon, and Z.-E. Boutaghou, "Time-frequency analysis of tribological systems – part I: implementation and interpretation," *Tribology International*, vol. 31, pp. 501-510, Sept., 1998.

[26] G. Sheng, B. Liu, and W. Hua, "A nonlinear dynamics theory for modeling slider air bearing in hard disk drives," *J. of Applied Physics*, vol. 87, pp. 6173-6175, May, 2000.

[27] J. C. Goswami, and A. K. Chan, *Fundamentals of wavelets: Theory, algorithms, and applications*, New York, NY: John Wiley and Sons, Inc., 1999.

[28] F. Auger, and P. Flandrin, "Improving the readability of time-frequency and time-scale representations by the reassignment method," *IEEE Trans. Signal Processing*, vol. 43, pp. 1068-1089, May, 1995.

[29] B. H. Thornton, and D. B. Bogy, "Non-Linear Aspects of Air Bearing Modeling and Dynamic Spacing Modulation in Sub 5 nm Air Bearings for Hard Disk Drives," *IEEE Transaction on Magnetics*, Vol. 39, pp. 722-728, March 2003.

[30] X. Ma, D. Kuo, J. Chen, H. Tang, and J. Gui, "Effect of lubricant on flyability and read-write performance in the ultra-low flying regime," *Proceedings of the Symposium on Interface Tribology Toward 100 Gb/in^2*, C. S. Bhatia, A. A. Polycarpou, and A. Menon, eds., ASME Trib-Vol. 10, Seattle, WA, pp. 27-34, Oct. 2000.

[31] T. Kato, S. Watanabe, and H. Matsuoka, "Dynamic characteristics of an in-contact headslider considering meniscus force: part 1—formulation and application to the disk with sinusoidal undulation," *ASME J. of Tribology*, vol. 122, pp. 633-638, July 2000.

[32] T. Kato, S. Watanabe, and H. Matsuoka, "dynamic characteristics of an in-contact headslider considering meniscus force: Part 2 – application to the disk with random undulation and design conditions**,"** *ASME J. of Tribology*, vol. 123, pp. 168-174, Jan. 2001.

[33] T. Kato, S. Watanabe, and H. Matsuoka, "dynamic characteristics of an in-contact headslider considering meniscus force: Part 3 – formulation and application to the disk with sinusoidal undulation," *ASME J. of Tribology*, vol. 124, pp. 801-810, Oct. 2002.

[34] C. Gao, and B. Bhushan, "Tribological performance of magnetic thin-film glass disks: its relation to surface roughness and lubricant structure and its thickness," *Wear*, vol. 90, pp. 60-75, Nov. 1995.

[35] Autumn, K., M. Sitti, A.M. Peattie, W. Hansen. S. Sponberg, Y.A. Liang, T. Kenny, R. Fearing, J.N. Israelachvili, R.J. Full, "Evidence for van der Waals adhesion in gecko setae," PNAS, vol. 99(19): 12252-12256, 2002.

[36] L. Wu, and D. B. Bogy, "Effect of the intermolecular forces on the flying attitude of sub- 5 nm flying height air bearing sliders in hard disk drives," *ASME J. of Tribology*, vol. 124, pp. 562-567, July, 2002.

[37] J. H. Li, B. Liu, W. Hua, and Y. S. Ma, "Effects of intermolecular forces on deep sub- 10 nm spaced sliders," *IEEE Trans. Magn* , vol. 38, pp. 2141-2143, Sept. 2002.

[38] B. Zhang, and A. Nakajima, "Possibility of surface force effect in slider air bearings of 100 Gbit/in^2 hard disks," *Tribology International*, vol. 36, pp. 291-296, April – June 2003.

[39] R.H. Wang, V. Raman, U.V. Nayak, "Head-Disk Interface Issues for Near Contact Recording," *Proceedings of the Symposium on Nanotribology and Nanotechnology for 1 Tbit/in^2*, A. A. Polycarpou, and C. Singh Bhatia, eds., ASME Trib-Vol. 11, San Francisco, CA pp. 37-43, 2001.

[40] N.V. Gitis, L. Volpe, "Nature of static friction time dependence," *J. Phys. D: Appl. Phys.*, Vol. 25, pp. 605-612, 1992.

[41] J. N. Israelachvili, *Intermolecular and surface forces, 2nd ed.* San Deigo: Academic Press, 1992.

[42] S. H. Strogatz, *Nonlinear Dynamics and Chaos*. Cambridge: Perseus Books, 1994.

[43] L. N. Virgin, *Introduction to Experimental Nonlinear Dynamics: A case study in mechanical vibration*. New York: Cambridge University Press, 2000.

[44] F. C. Moon, and P. J. Holmes, "Magnetoelastic strange attractor," *J. of Sound and Vibration*, vol. 65, pp. 275-296, 1979.

[45] P. J. Holmes, and F. C. Moon, "Strange attractors and chaos in non-linear mechanics," *ASME J. of Applied Mechanics*, vol. 50, pp. 1021-1032, 1983.

[46] B. V. Derjaguin, V. M. Muller, and Y. P. Toporov, "Effect of contact deformations on adhesion of particles," *J. of Colloid and Interface Sci.*, vol. 53, pp. 314-326, 1975.

[47] S. I. Lee, W. Howell, A. Raman, and R. Reiferberger, "Nonlinear dynamics of mircocantilevers in tapping mode atomic force microscopy: A comparison between theory and experiment," *Phys. Rev. B*, vol. 66, 115409, 2002.

[48] W. R. Chang, I. Etsion, and D. B. Bogy, "Adhesion Model for Metallic Rough Surfaces," *ASME J. of Tribology*, vol. 110, pp. 50-56, Jan. 1988.